

UNIVERSITY OF LODZ
FACULTY OF PHYSICS AND APPLIED INFORMATICS

**GRAPHENE HETEROSTRUCTURES WITH TRANSITION METAL
OXIDES – INVESTIGATIONS OF MORPHOLOGY AND ELECTRONIC
STRUCTURE TOWARDS APPLICATIONS IN ORGANIC
ELECTRONICS**

A Dissertation Presented

by

Dorota A. Kowalczyk, M.Sc.Eng.

supervised by:

Prof. Zbigniew Klusek, DSc (passed away 18.12.2019)

Dr. Pawel J. Kowalczyk, DSc, prof. UL

co-supervised by:

Dr. Maciej Rogala

Submitted for the degree of

DOCTOR OF PHILOSOPHY

Lodz, 2022

UNIwersytet Łódzki
Wydział Fizyki i Informatyki Stosowanej

**HETEROSTRUKTURY GRAFENU Z TLENKAMI METALI
PRZEJŚCIOWYCH - BADANIA MORFOLOGII I STRUKTURY
ELEKTRONOWEJ W KIERUNKU ZASTOSOWAŃ DO ORGANICZNEJ
ELEKTRONIKI**

Mgr. inż. Dorota A. Kowalczyk

Łódź, 2022

“Just think, the future of humanity and technology will most likely actually be enhanced by scientists pulling pencil lead off of a sheet of paper with scotch tape and looking at what they pulled off.”

- Darth Koonstyle

Acknowledgments and Funding / Podziękowania

Throughout my PhD studies I have received a great deal of guidance and support. I would like to thank those who trained me and provided help during data-collection and analysis. Sincere acknowledgements go to those who contributed to my research.

Na wstępie chciałbym podziękować mojemu pierwszemu promotorowi, śp. Panu Profesorowi Zbigniewowi Kluskowi, którego wiedza i opieka były nieocenione. Jego wpływ podniósł moją pracę na wyższy poziom.

Serdeczne podziękowania składam na ręce moim promotorom, P. Dr. hab. Pawłowi Kowalczykowi, Prof. Uł, i P. Dr. Maciejowi Rogali, którzy nieprzerwalnie obdarzają mnie wsparciem. Drodzy Promotorzy, chcę Wam podziękować za Wasze cierpliwe wsparcie, rady i za wszystkie możliwości, jakie otrzymałam, aby rozwijać moje badania.

Pragnę również podziękować wszystkim członkom zespołu działającego w ramach Katedry Fizyki Ciała Stałego UŁ, a w szczególności koleżeństwu, które dzieliło ze mną większość moich chwil pracy nad badaniami do doktoratu: P. Dr. hab. Adamowi Busiakiewiczowi, P. Mgr. Justynie Czerwińskiej, P. Dr. Pawłowi Dąbrowskiemu, P. Dr. Ewelinie Frątczak, P. Dr. Jarosławowi Lutsykowi, P. Dr. hab. Witoldowi Kozłowskiemu, P. Dr. Pawłowi Krukowskiemu, P. przyszłej Dr. Katarzynie Pabianek, P. przyszłemu Dr. Michałowi Piskorskiemu oraz P. Dr. Hab. Karolowi Szałowskiemu, Prof. Uł.

Collaborators

In addition, I thank the external collaborators with whom I had the pleasure to work:

- Towarzystwo Elektrotechnologiczne QWERTY Sp.z o.o., especially M. Sc. Eng. Zbigniew Sieradzki
- University of Lodz, especially Faculty of Chemistry, including Dr. Michał Cichomski
- AGH University of Science and Technology, including Dr. Artur Rydosz, Dsc, and Prof. Katarzyna Zakrzewska
- Lodz University of Technology, including especially Dr. Beata Łuszczńska, Dsc, Dr. Ruslana Udovyt'ska, Dr. Jarosław Jung, Dsc, Dr. Marcin Kozanecki, DSc, Dr. Tomasz Kłąb, and Prof. Jacek Ulański
- Łukasiewicz Research Network - Institute of Electronic Materials Technology, including Dr. Paweł Ciepielewski, Dr. Piotr Caban, and Prof. Jacek Baranowski
- Warsaw University of Technology, including Dr. Iwona Pasternak and her coworkers
- Jagiellonian University, including especially Dr. Piotr Ciochoń

- University of Warsaw, including Dr. Jakub Kierdaszuk
- Maria Curie-Skłodowska University, including especially Dr. Marek Kopciuszynski and his coworkers
- Lund University including Dr. Domagoj Belić and Prof. Viveka Alfredsson
- University of Bristol, including Dr. Gary Wan, Prof. Neil Fox, and Dr. Jude Laverock
- Penn State University, including especially Prof. Joan Redwing and her group, as well as Dr. Yu-Chuan Lin, and Material Research Institute staff

Funding: Grants and Stipends

I hereby acknowledge the financial support:

- Fulbright Junior Research Award, 2020–2021 (8-month project at the Pennsylvania State University, USA)
- The National Science Centre, Poland
 - Sonata Bis, research grant no. 2018/30/E/ST5/00667
 - OPUS 11, research grant no. 2016/21/B/ST5/00984
- Stypendium Prezydenta Miasta Łodzi, VII edycja - 2017/2018
- The European Funds within Smart Growth Operational Programme under project of The National Centre for Research and Development, Poland, POIR.04.01.02-00-0046/16.

Abstract

The unique electrical, optical and mechanical properties of graphene make it attractive as a flexible transparent electrode for applications in organic electronics, e.g. organic light emitting diodes (OLEDs). However, the intrinsic electronic structure of graphene does not match energy levels in organic systems. Such matching can be achieved by depositing a transition metal oxide (TMO) on graphene, creating a heterostructure with new electronic properties.

The aim of this work concerns mainly the modification of graphene work function due to interaction with TMO of high work function (WF) with respect to matching the energy levels of the developed heterostructures to the requirements of OLED technology. The core of this thesis addresses synthesis of selected TMOs (molybdenum and rhenium oxides, MoO_3 and Re_2O_7) on graphene and highly oriented pyrolytic graphite (HOPG). The morphology of grown structures was studied in detail, with particular emphasis on molybdenum oxide monolayers. The electronic structure of obtained heterostructures was investigated, in particular, value of work function.

As a first step, the study focuses on the direct synthesis and *in-situ* characterisation of monolayer MoO_3 on HOPG by thermal evaporation in UHV. It results in two-dimensional, nearly stoichiometric, and electrically conductive MoO_3 , where local electronic structure possesses apparent energy gap of 0.4 eV which is uniform for the first three layers. Next, we address the deposition process of MoO_3 on graphene, with different properties depending on its substrate, to ultimately get as thin MoO_3 layer as possible. The third step is to explore the WF of MoO_3 monolayers in different conditions. The innovative character of this part is proposing crystalline MoO_3 monolayer for enhancement of substrate WF up to 6.4 eV for thicknesses as low as 0.7 nm. To close with the second TMO example, we study the potential of Re_2O_7 to increase graphene WF, leading to +0.8 eV for graphene/ Re_2O_7 heterostructure.

Streszczenie

Unikalne właściwości elektryczne, optyczne i mechaniczne grafenu czynią go atrakcyjnym jako elastyczna, przezroczysta elektroda do zastosowań w elektronice organicznej, np. organicznych diod elektroluminescencyjnych (OLEDs). Jednakże, struktura elektronowa grafenu nie jest dopasowana do poziomów energetycznych w układach organicznych. Takie dopasowanie można osiągnąć poprzez osadzenie tlenku metalu przejściowego (TMO) na grafenie, tworząc heterostrukturę o nowych właściwościach elektronicznych.

Celem niniejszej pracy jest opracowanie modyfikacji pracy wyjścia grafenu w następstwie oddziaływania z TMO o wysokiej pracy wyjścia (WF) z uwzględnieniem dopasowania poziomów energetycznych powstałych heterostruktur do wymagań technologii OLED. Główna część rozprawy dotyczy syntezy wybranych TMO (tlenków molibdenu i renu, MoO_3 i Re_2O_7) na podłożach grafenowych i grafitu pyrolitycznego (HOPG). Zbadano zarówno morfologię otrzymanych heterostruktur, ze szczególnym uwzględnieniem monowarstw tlenku molibdenu, jak również ich strukturę elektronową, w szczególności wartość pracy wyjścia.

W pierwszym etapie pracy skupiono się na bezpośredniej syntezie i charakteryzacji *in-situ* monowarstwowego MoO_3 na HOPG metodą parowania termicznego w warunkach ultra wysokiej próżni. W ten sposób otrzymano dwuwymiarowy, prawie stechiometryczny i elektrycznie przewodzący MoO_3 , którego lokalna struktura elektronowa posiada przerwę energetyczną o szerokości 0,4 eV – taką samą dla pierwszych trzech warstw. Następnie, zajęto się procesem osadzania MoO_3 na grafenie, którego właściwości różniły się w zależności od podłoża, na którym został wytworzony i ostatecznie skoncentrowano się na otrzymaniu możliwie cienkiej warstwy MoO_3 . W trzecim etapie zbadano pracę wyjścia monowarstw MoO_3 w różnych warunkach. Nowatorski charakter tej części pracy polega na zaproponowaniu krystalicznej monowarstwy MoO_3 dla zwiększenia pracy wyjścia podłoża do 6,4 eV przy grubości zaledwie 0,7 nm. Na zakończenie zbadano drugi przykład TMO – Re_2O_7 , w celu określenia jego potencjału do zwiększenia pracy wyjścia grafenu. Wykonane badania wskazują, że w przypadku heterostruktury grafen/ Re_2O_7 następuje wzrost pracy wyjścia o 0.8 eV.

List of Abbreviations & Symbols

1L	Monolayer (One Layer)
2D	Two-Dimensional
2L	Bilayer (Two Layers)
3D	Three-Dimensional
3L	Trilayer (Three Layers)
AFM	Atomic Force Microscope (Microscopy)
c-AFM	Contact Atomic Force Microscopy
BE	Binding Energy
CVD	Chemical Vapour Deposition
DFT	Density Functional Theory
E_F	Fermi Level
FFT	Fast Fourier Transform
HIL	Hole Injection Layer
HOPG	Highly Oriented Pyrolytic Graphite
HR-TEM	High-Resolution Transmission Electron Microscope (Microscopy)
KPFM	Kelvin Probe Force Microscope (Microscopy)
LEED	Low-Energy Electron Diffraction
nc-AFM	Non-Contact Atomic Force Microscopy
PES	Photoelectron Spectroscopy
PVD	Physical Vapour Deposition
RMS	Root Mean Square
RT	Room Temperature
SPM	Scanning Probe Microscopy
STM	Scanning Tunneling Microscope (Microscopy)
STS	Scanning Tunneling Spectroscopy
TMO	Transition Metal Oxide
UHV	Ultra High Vacuum
UPS	Ultraviolet Photoelectron Spectroscopy
vdW	van der Waals
WF, ϕ	Work Function
XPS	X-ray Photoelectron Spectroscopy

Contents

Acknowledgments and Funding / Podziękowania	VI
Funding: Grants and Stipends	VII
Abstract	VIII
Streszczenie	IX
List of Abbreviations & Symbols.....	X
Introduction.....	13
Outline.....	14
1. Background and Motivation.....	16
1.1. High work function of selected TMOs: key parameter	17
1.2. Transition Metal Oxides in Organic Electronics	19
1.3. Introduction to Transition Metal Oxides.....	19
1.3.1. Molybdenum Oxides.....	20
1.3.2. 2D α -MoO ₃	21
1.3.3. Rhenium Oxides	24
1.4. Graphene & HOPG	25
2. Experimental Methods	27
2.1. Ultra High Vacuum Systems.....	27
2.2. Sample Preparation: Thermal Evaporation	28
2.2.1. Substrates: Graphite and Graphene.....	29
2.2.2. Molybdenum Oxide on HOPG and Graphene.....	30
2.2.3. Rhenium Oxide on Graphene.....	30
2.3. Material Characterisation.....	31
2.4. UPS Work function Measurements in UHV: Uncoalesced 2D Films.....	32
2.5. KPFM Work function Measurements.....	35
2.6. Computations & software	35
3. α -MoO ₃ Monolayer Grown on Graphite Substrate.....	36
3.1. Introduction.....	37
3.2. Results and Discussions.....	39
3.2.1. Stable Monolayer of MoO ₃ : Morphological and Crystallographic Characterisation.....	39
3.2.2. Chemical and Electronic Structure: XPS and UPS Characterisation	45
3.2.3. Local electronic structure of MoO ₃ from monolayer to trilayer: STM/STS characterisation	48

3.2.4.	Air Exposure Effect on Monolayer MoO ₃ : STS and UPS Characterisation.....	51
3.2.5.	Theoretical characterisation	53
3.3.	Conclusions	56
4.	Towards Graphene/2D MoO ₃ Heterostructures: Translating the Growth of α -MoO ₃ from Graphite to Graphene	59
4.1.	Introduction to Graphene/MoO ₃ Heterostructures	60
4.2.	Results and Discussion: Effect of Graphene Substrate on the Growth of MoO ₃ Thin Films Grown by Thermal Evaporation	61
4.2.1.	Graphene on Cu: Morphological Characterisation.....	61
4.2.2.	Graphene on SiC: Morphological and Crystallographic Characterisation	64
4.3.	Conclusions	72
5.	Work Function of α -MoO ₃ Monolayers in Heterostructures with Graphite and Graphene	74
5.1.	Introduction	75
5.2.	Results and discussion.....	77
5.2.1.	Local Surface Potential of Monolayer MoO ₃ in Ambient Conditions	77
5.2.2.	Local Surface Potential on Monolayer MoO ₃ & HOPG in UHV	81
5.2.3.	Restoration of High Work Function of Air-Exposed MoO ₃ Monolayers: Post-Processing by UHV Annealing	84
5.3.	Conclusions	90
6.	Graphene Heterostructures with Rhenium Oxide	93
6.1.	Introduction	94
6.2.	Results and Discussion.....	95
6.2.1.	Chemical Structure: XPS Characterisation.....	95
6.2.2.	Thermally Evaporated Re ₂ O ₇ Nanoparticles on Graphene.....	96
6.2.3.	Re ₂ O ₇ Nanoparticles Misplacement by STM/AFM Tips on Graphene Surface ...	99
6.2.4.	Controlling work function of graphene/Re ₂ O ₇ heterostructure: UPS Characterisation.....	102
6.3.	Conclusions	104
	Conclusions.....	106
	References	109
	Appendix A: XPS Database for Mo3d.....	119
	Appendix B: Academic achievements	121
B1.	Publications.....	121
B2.	Dissemination of Results: Conference Contribution.....	122
B3.	Extracurricular Courses & Activities.....	125

Introduction

The unique electrical, optical, and mechanical properties of graphene make it attractive as a transparent electrode for potential applications in organic electronics. However, the intrinsic electronic structure of graphene does not match energy levels in organic systems. Such matching can be achieved by depositing transition metal oxide (TMO) on graphene, creating a heterostructure with novel electronic properties.

TMO films are commonly used in organic electronics devices to improve charge-injection between electrodes and organic layers. TMO monolayers hold their promise in ultrathin optoelectronics. However, as described in the literature TMOs films need high deposition temperatures and are usually amorphous/polycrystalline, thereby requiring thick films to provide continuity and desired properties, hindering their further ultrathin applications.

Despite some graphene/TMOs heterostructures satisfying initial expectations in organic electronic applications, the choice of TMOs with particular properties remains unlimited, and the choice of required thickness of TMOs seems undefined. In the case of graphene anodes, this mainly concerns modification of their work function (WF) due to interaction with a TMO having high WF. The study of described choices will be the subject of this work, which can contribute to designing a new type of conducting, transparent, and flexible heterostructures for anodes with electronic structure aligned to organic semiconductors.

The aim of this work is to synthesise selected TMOs (molybdenum and rhenium oxides) on substrates belonging to the graphene family. The morphology of grown structures will be studied in detail, with particular emphasis on molybdenum oxide monolayers. The electronic structure of obtained heterostructures will be investigated, in particular, value of their WF.

As a first step, the study will focus on direct synthesis and *in-situ* characterisation of MoO₃ monolayer on a graphene bulk counterpart – highly oriented pyrolytic graphite (HOPG). To establish a base for 2D form of MoO₃ concerning growth habits, stoichiometry, and local electronic structure for the first layers, which would be a novelty, we will study a model heterostructure of HOPG/MoO₃.

Next, we address the deposition process of MoO₃ on graphene with different properties depending on a substrate (Cu or SiC) and thickness (from monolayer to few-layer graphene) to ultimately get as thin MoO₃ layer as possible – this time on the target substrate, i.e. graphene.

The third step is to explore the WF of MoO₃ under different conditions in order to determine the highest value of WF that MoO₃ has to offer while reaching the limit of the minimal thickness of films, i.e. going down to monolayers. Therefore, the contribution of this study is

going beyond the usual approach, i.e. finding the final saturation of WF with increase in film thickness. Instead, we optimize the crystallographic and chemical structure of material to search for films that meet the WF requirements with continuity of surface with lowest possible thickness. Testing different conditions in this study will define the critical environment for utilising the highest qualities of MoO₃ monolayers and possible threads. Post-processing method of annealing after air exposure will be investigated.

To close with the second TMO example, we study the deposition and potential of Re₂O₇ in tuning the graphene WF. In contrast to MoO₃, rhenium oxides are not commonly used in organic electronic devices yet. Studying Re₂O₇ is not only much room for unexplored applications and development of new heterostructures, but also an advantage of lower temperatures of deposition.

The chosen transition metal oxides will be deposited by thermal evaporation in UHV. After determination of optimised deposition parameters, the samples will undergo comprehensive characterisation. For this purpose, the complementary experimental techniques will be used for analysis of surface morphology (atomic force microscopy (AFM) and scanning tunnelling microscopy (STM)), crystal structure (low-energy electron diffraction (LEED) and high-resolution transmission electron microscopy (HR-TEM)), chemical composition (X-ray photoelectron spectroscopy (XPS)), and local and global electronic structure (scanning tunnelling spectroscopy (STS), kelvin probe force microscopy (KPFM), ultraviolet photoelectron spectroscopy (UPS)). Additionally, the obtained results will be supported by numerical calculations in density functional theory (DFT) framework.

Note that in this Thesis, the terms MoO₃ and Re₂O₇ refer to molybdenum trioxide and rhenium heptoxide, which are not fully stoichiometric.

Outline

This thesis is structured as follows.

- **Chapter 1** presents the background and elaborates on the motivation driving this research. It starts with a need of organic electronic and continues with an overview of selected TMOs: MoO₃ and Re₂O₇, with emphasis on 2D MoO₃ as well as substrates: graphene and HOPG. The reader can expect to find more literature review necessary for discussion in each of subsequent Chapters describing experimental results.

- **Chapter 2** describes the experimental methods used in this work, covering the most details on work function measurements, including a practical UPS guide for interpretation of results from uncoalesced 2D films or two-component surfaces.
- In **Chapter 3**, the study of MoO₃ monolayers on HOPG is described in detail. In particular, the morphology, crystal structure, chemical composition, and electronic structure of the first three MoO₃ layers in the macro- and nanoscale are analysed. Additionally, the effect of air exposure is investigated. DFT calculations support the experimental analysis.
- **Chapter 4** presents a growth study of MoO₃ on graphene substrates revealing the difficulties in reproducing monolayers of MoO₃ grown on HOPG, where graphene synthesized on Cu and SiC were used. Moreover, it describes whether the chosen deposition method is harmful to graphene.
- **Chapter 5** is devoted to work function measurements in ambient and UHV conditions of MoO₃ monolayers on HOPG and graphene. Moreover, the restoration method after air exposure is proposed and tested.
- **Chapter 6** focuses on studying graphene heterostructure with Re₂O₇. In particular, it describes morphology, chemical composition, and the electronic properties of deposited structures.
- Finally, **Chapter 7** summarizes and concludes the major experimental findings of this Thesis.

Appendix A contains literature data of binding energies and energy separation of Mo oxidation states helpful for Mo3d analysis by XPS. A list of publications and details of the academic contributions that have resulted from this thesis are summarized in **Appendix B**.

1. Background and Motivation

Numerous scientific groups have made much effort to guarantee energy-level alignment between functional layers in organic electronic devices [1–5]. If we take only one element of a device, an anode and think of it as a separate part, we may design a transparent, flexible, and ultra-thin electrode, which needs to possess specific properties to meet, i.e., energy-level alignment requirements.

Transparent electrodes are used in many areas of modern electronics and are commonly found in optoelectronic devices [6,7], such as displays [8,9], touch screens [8,10], light-emitting diodes [9,11], and solar cells [2,12]. Thereby, doped metal oxides like indium tin oxide (ITO) are currently widely used as the standard material [2,13,14]. In addition, future displays are expected to be larger and reside on plastic. Therefore, prospective displays must be flexible, while ITO is brittle [14,15], and must be produced at low temperatures and over large areas. Such requirements must be in addition to standard technical requirements associated with, e.g., low sheet resistance.

Among the range of potential replacement materials for ITO, graphene shows great promise due to its two-dimensional (2D) bonding configuration offering flexibility, mechanical robustness as well as chemical inertness combined with excellent electrical and optical transparency in the range of visible light [1,16,17].

Graphene supports high electronic mobility, but at the same time, it intrinsically shows low electrical conductivity due to the low charge carrier concentration. Consequently, stable doping of graphene is crucial to achieving sheet resistance below 100 Ω/sq with optical transmittance above 90% [1,18,19]. This links to substantial modification in the work function (WF) of graphene.

Recent reports highlighted promising results of graphene-based electrodes, particularly for organic electronic applications, including organic light-emitting diodes (OLEDs) and organic photovoltaic (OPV) cells [11,14,19]. For those applications, band engineering is at least as important as sheet resistance of the transparent conductor materials.

From the perspective of an anode in those devices, the low WF of graphene [1,19,20] causes inefficient hole injection between the graphene anode and the neighbouring hole-transporting layer (HTL) due to high potential barrier between those components [4]. Hence, the efficiency of OLEDs with the graphene anodes becomes poorer than OLEDs fabricated on the ITO anode.

To reduce interfacial barriers, the graphene drawbacks have been overcome by deposition of layers of transition metal oxides (TMOs) onto graphene, forming graphene/TMO

heterostructure systems. The TMOs and graphene themselves cannot provide the desired parameters, but the idea of merging two dissimilar materials of different physical and chemical properties into one heterostructure system of new properties seems very promising.

While such interfacial TMO films are becoming more and more widely used with graphene electrodes, the focus of the scientific discussion has been either revolving around stable doping [4] or improved wetting [21,22], and there are few reports addressing a fundamental understanding of the new interfacial electronic structure [3,23,24]. From the side of organic semiconductors, the mechanism for level alignment between the organic layers and TMOs was demonstrated [3,5], where they derived a mathematical relation that describes the alignment governed by electron-chemical-potential equilibration. **Although the application of graphene/TMOs heterostructures as anodes satisfy initial expectations [14,19], their ultimate optimisation remains ambiguous in terms of the minimal thickness or highest work function. Such a heterostructure system is interesting for basic research in terms of thickness limitations and exploration of TMOs candidates to be connected with graphene, in addition to the proven advantages of electronic applications.**

1.1. High work function of selected TMOs: key parameter

TMOs have been the subject of studies on charge transport in organic electronic devices [23,24]. In particular, they have been reported to impact device performance significantly. Enhanced hole injection in OLED [25,26] and hole extraction in OPV [2,12] were established with the insertion of a thin layer of TMO, improving their performance. High WF TMOs – such as MoO_3 , WO_3 , and V_2O_5 – are already in use as anode buffer layers in organic electronics [23,24,27]. **However, rhenium oxides, also characterised by high WF (over 7 eV [28,29]), have not yet been extensively explored.**

Due to their high WF, selected TMOs provide a favourable alignment of the energy levels with the neighbouring active materials in mentioned devices [23,24]. The relative position of the energy levels at the interface and the resultant energy level alignment between the two contacting materials is essential for efficient charge transport [23,24]. A low-resistance contact requires the Fermi level of the anode (parameterised by WF) to be closely aligned with the highest occupied molecular orbital (HOMO) level of the organic semiconductor. In fact, the Fermi level of graphene is located at around 4.2–4.6 eV [19,20], while the typical hole transporting material - commonly used in OLEDs – like N,N'-di(1-naphthyl)-N,N'-diphenyl-(1,1'-biphenyl)-4,4'-diamine (α -NPD) has a HOMO level at around 5.5 eV [3,30].

With minor variations in the mechanism of the caused enhancement [2,23,24], the improved contact with the anode and organic layer material for the hole transportation is almost undisputed. The high WF of TMO is recognised as the key parameter for understanding such improvements [24,31,32].

WF is defined as the minimum energy required to withdraw an electron completely from a metal surface [33–35]. The experimentally measured WF value of a material represents the energy difference between the Fermi and the local vacuum level [23,31]. The surface science techniques to measure WF are ultraviolet photoelectron spectroscopy (UPS), on the microscale, and kelvin probe force microscopy (KPFM), on the nanoscale. Both these techniques will be used in this work.

As widely highlighted in the literature, securing the energy level alignment has been proven to increase efficiency of devices [4,19,36]. Consequently, determining the way to obtain the highest WF possible, therefore its dependence on TMO film thicknesses has been the focus of many research groups [6,19,20,37,38]. In other words, how thick needs to be a TMO film to modify the WF of its substrate to provide aligned energy levels.

The literature describes WF tuning of TMOs in the function of film thickness and the influence of the substrate [6,19,37–41]. The evolution of WF observed by UPS measurements is usually presented in the following way: a rapid shift of WF occurs during the deposition of the first few nm of the TMO film, while saturation occurs between specific thicknesses, reaching the highest possible surface WF at given conditions. In the case of MoO₃ films deposited on the graphene substrates for anode applications, a gradual increase along with MoO₃ film thickness has been reported. At the nominal thickness of 1.4 nm, WF reaches 5.9–6.4 eV [6,41], while the final saturation (≤ 6.80 eV) occurs for thicker MoO₃ films of about 4.0–5.0 nm [6,19,37]. The latter value agrees with the reported WF for bulk α -MoO₃ of 6.9 eV [19,38,42,43].

On the other hand, α -MoO₃ has been predicted to retain bulk electronic properties while taking 2D form [44–48], which includes the high work function. Other calculations explain the WF enhancement in electrodes by modifying surface dipoles induced by the ultrathin dielectric layer [49,50]. In particular, these works suggest that the work function of metals can be significantly increased or decreased by a dielectric coating as thin as just one monolayer thick. **In this Thesis, we propose monolayer α -MoO₃ films sufficient to increase the WF of the graphene substrate to a desirable level for organic electronic applications.** This could downscale the thickness of films currently used for tuning WF down to < 1 nm.

1.2. Transition Metal Oxides in Organic Electronics

For investigations described in following Chapters among all TMOs the molybdenum and rhenium oxides were chosen for building heterostructures with graphene. This selection was supported by several reasons:

- I. Mo and Re oxides have higher work function than graphene.
- II. Mo and Re oxides can be deposited via thermal evaporation; therefore, the film thickness can be easily monitored and controlled.
- III. Mo and Re oxides can be deposited in low temperatures (with particularly low for Re_2O_7).
- IV. Mo and Re oxides deposited via thermal evaporation are unlikely to induce defects in graphene in contrast to, e.g., TiO_2 [51].
- V. Mo and Re oxides can be deposited in UHV; therefore, the environment can be controlled avoiding any contact with air (air is likely to reduce work function of these TMOs [42,43]).
- VI. $\alpha\text{-MoO}_3$ is naturally layer material holding a promise of functional monolayers.
- VII. Films of MoO_3 are commonly used in organic electronics as a hole injection layer and bulk MoO_3 has been extensively studied. Thus, the electronic structure of bulk MoO_3 is well understood, supporting reliable analyses on the MoO_3 monolayers.

Additionally, what is beyond this study, some aspects of optical properties of chosen materials are worth mentioning. The visible light transmittance of one- to five-layer pristine graphene was reported to be at the level of 98%, 95%, 93%, 90%, and 88%, respectively [52], which means that transmittance of graphene decreases by around over 2% with each added layer [52,53]. TMOs, themselves, have high transmittance of 85%–90% in the visible range [25,54]. In particular, the transmittance through graphene synthesised on SiC and covered with Re_2O_7 (nominal thickness of 25 nm) decreased by about 7% in comparison with uncovered graphene [20]. The average optical transmittance of ReO_3 film with different thickness (up to nominal 1.5 nm) on quartz substrate was higher than 98% [13].

1.3. Introduction to Transition Metal Oxides

Transition metal oxides (TMOs) is a family of materials with many diverse properties such as superconductivity, magnetism, and ferroelectricity [55,56]. Thus, TMOs find applications ranging from catalysis, solar cells to electronic devices [24,55].

TMOs family contains wide variety of oxides. Many TMOs exhibit more than one stable oxidation state and form more than one oxide [27,57]. For example, molybdenum occurs at the following formal oxidation states: 6+ and 4+, with the corresponding stable oxides: MoO₃ and MoO₂. In addition, there is possibility of oxides affected by oxygen vacancies both undefined and those with defined stoichiometry [27,57]. Some of them are stable, e.g., Mo₄O₁₁, Mo₅O₁₄, Mo₆O₁₇, Mo₇O₂₀, Mo₈O₂₃, Mo₉O₂₆, Mo₁₇O₄₇, and Mo₁₈O₅₂. Then, each oxide possesses unique properties. For example, electronic band structure of TMOs can range from insulating to conducting [31,38]. Some TMOs are inert, while others are catalytically active [58]. Also, they can exhibit a wide range of work functions [31,59]. TMOs thin films are commonly used in organic electronics to improve charge-injection between organic semiconductors and electrodes [23,24,27]. Some TMOs are good hole-injectors, while some others are good electron-injectors. The metal oxidation state, stoichiometry and density of vacancy defects are the factors affecting TMOs electronic structures [55,60]. Therefore, any of these factors may affect energy-level alignment in organic electronic devices.

Among other members of TMOs family such as vanadium, nickel or copper oxides, we will provide more detail review only for those presented in this Thesis: molybdenum [19,31] and rhenium oxides [28,29]. The vast part of following investigations focuses on monolayer of α -MoO₃. Therefore, a broader review in this topic will be described in the following Section 1.3.2.

1.3.1. Molybdenum Oxides

As mentioned, molybdenum can be found in various oxide stoichiometries, which play an important role in many versatile applications, ranging from catalysis, batteries, gas sensors to optoelectronics, and future twistrionics [27,61,62]. Variations in the oxidation states allow for manipulating the crystal structure, morphology, and oxygen vacancies, to control and engineer electronic states [27]. In terms of organic electronics, efforts have been taken toward graphene-based electrodes addressing devices with films of MoO₃ as a hole injection layer (HIL) [6,19]. However, the practical attractiveness of MoO₃ may lay in the electronic structure of its 2D form (monolayer of α -MoO₃(010) phase (see below for explanation)), as theoretical calculations predict that it is not significantly altered from the bulk [44–48].

The most stable phase of molybdenum trioxide is orthorhombic α -MoO₃. It has a layered crystal structure, Figure 1, consisting of corner-sharing octahedral nets linked by van der Waals (vdW) forces [39,63], which offers creation of 2D morphologies. The unit cell of

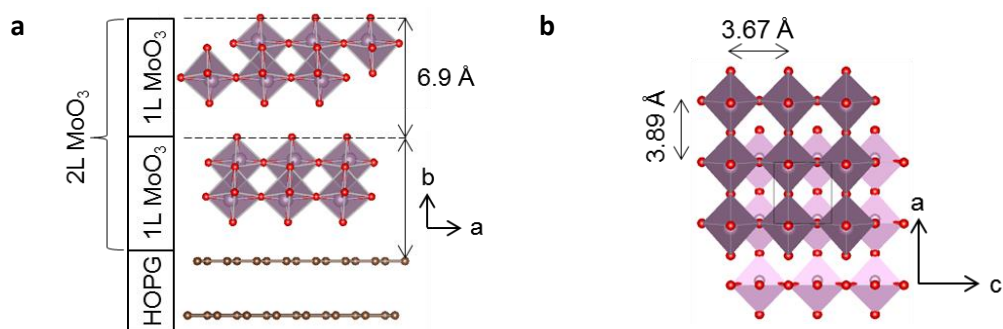


Figure 1: Crystal structure of α - MoO_3 . (a) Side view of two layers (2L) of MoO_3 on HOPG. The height of a monolayer (1L) MoO_3 including vdW gap is marked. (b) top view of the atomic structure of 1L α - MoO_3 .

α - MoO_3 is built of two layers (see marked 2L in Figure 1a) of chemically bonded octahedra, where the layers are separated by a vdW gap [39,63]. The layered α - MoO_3 was the subject of many studies; however, its 2D form was not uniformly addressed. Here we want to define a monolayer (1L) of α - MoO_3 as a single layer of the octahedral net corresponding to half of the unit cell (in vertical b direction or [010]) with the thickness of 6.9 Å, which is a half of the b -axis lattice parameter of a single unit cell α - MoO_3 .

α - MoO_3 is an n-type semiconductor with a bandgap of over 3 eV [46], while it can be easily doped by oxygen vacancies forming MoO_{3-x} [42,46,64–66] and inducing additional bands below the conduction band minimum (CBM), which leads to a local decrease of the bandgap [67]. Therefore, the electronic properties of molybdenum oxides are in the broad range of insulating (for stoichiometric MoO_3) through semimetallic (for MoO_{3-x} with relatively small x) to metallic (for MoO_{3-x} , $x \leq 1$). The stoichiometry of molybdenum oxides can be easily controlled via, e.g., annealing in vacuum or nitrogen [65,68,69]. On the other hand, annealing treatments of ultrathin films have barely been reported.

1.3.2. 2D α - MoO_3

There are relevant papers regarding the models of MoO_3 growth in 2D form. This section covers the information available up to date in the literature about layers of α - MoO_3 , focusing on monolayer (1L), and bilayer (2L) up to few layers (called also nanosheets). The data relates to 2D MoO_3 films grown on various substrates, including metals (Au), 2D templates (e.g. graphene, hBN, mica), and oxide substrate (SrTiO_3). The growth of mono- or few-layered MoO_3 films has been achieved by several methods, such as the most common thermal evaporation either in air (hot plate method) [44,70,71] or in UHV [72], e-beam evaporation [73], flame

Ref.	Substrate & Method	Monolayer (1L)	Bi- (2L) or Few-layer	Highlights
Kim <i>et al.</i> 2019 [71]	multilayer graphene or graphite; hot plate method	<ul style="list-style-type: none"> unstable in air (observed by AFM but mobile) 	<ul style="list-style-type: none"> α-MoO₃ phase square-like single crystal 	thickness-insensitive properties: <ul style="list-style-type: none"> friction work function dielectric constant PES: (450eV) Mo ⁶⁺ ~70%, Mo ⁵⁺ ~30%; (750eV) also Mo ⁴⁺ and lower oxidation states
Kim <i>et al.</i> 2018 [70]	graphene hBN mica MoSe ₂ MoTe ₂ WSe ₂ sapphire; hot plate method	<ul style="list-style-type: none"> height of 0.7 nm quasi-stable irregular shapes 	<ul style="list-style-type: none"> α-MoO₃ phase quasi-square single-crystal relative angles integer multiples of 60° 	<ul style="list-style-type: none"> thickness-dependent band gap 2.9 eV to 3.2 eV (bulk) valence band maximum 2.8 eV below the Fermi level work function of 4.6 eV (as-grown) to 5.2 eV (after sputtering) XPS: Mo ⁶⁺ 96%, Mo ⁵⁺ 6%
Wang <i>et al.</i> 2016 [74]	fluorophlogopite mica APPVD	-	<ul style="list-style-type: none"> α-MoO₃ phase rectangular flakes aligned in three major orientations 120° wrt. each other 1.4 nm height 	<ul style="list-style-type: none"> growth temperature between 350 °C and 480 °C controllable thickness lateral sizes reaching several tens of micrometres AFM: visible perturbations
Molina-Mendoza <i>et al.</i> 2015 [44]	muscovite mica(001); hot plate method	-	<ul style="list-style-type: none"> α-MoO₃ phase 1.4–4.0 nm height ~60° between crystals 	<ul style="list-style-type: none"> transferable lateral sizes reaching centimetres thickness variations XPS: transfer onto Au resulted in pure MoO ₃
Cai <i>et al.</i> 2017 [75]	muscovite mica; flame synthesis	<ul style="list-style-type: none"> lateral size of several micrometres ~0.8 nm height 	-	<ul style="list-style-type: none"> at 450 °C controllable thickness rapid deposition (2 min)
	few-layer graphene; flame synthesis	-	<ul style="list-style-type: none"> α-MoO₃ phase rectangular shape thickness of 2 to 12 nm 	<ul style="list-style-type: none"> rapid deposition structural change under electron beam
Biener <i>et al.</i> 2004; Biener and Friend 2004; Deng <i>et al.</i> 2008; Guimond <i>et al.</i> 2013; Quek <i>et al.</i> 2005 [22,76–79]	Au(111); oxidation of Mo layer	<ul style="list-style-type: none"> (5.77 × 5) Å first published 0.5 nm [76,77] height of 0.7 nm [22] semimetallic well-defined edges with kinks and domain walls 6% Mo⁵⁺ 	<ul style="list-style-type: none"> (11.5 × 5.0) Å corrugation lines >2L crystallites of α-MoO₃ 1.3 nm height domains with random azimuthal orientations 	<ul style="list-style-type: none"> despite herringbone reconstruction of clean Au(111), STM images indicated no reconstruction under the MoO₃ islands hydrogen adsorbed more strongly than on bulk MoO₃
Du <i>et al.</i> 2016 [72]	Nb-doped SrTiO ₃ (001); UHV thermal evaporation	<ul style="list-style-type: none"> height of 0.7 nm iso-oriented square-like (concluded from an STM scan by the author) Mo⁵⁺ 9% 	<ul style="list-style-type: none"> α-MoO₃ phase single-phase epitaxy highly crystalline fully stoichiometric 	<ul style="list-style-type: none"> self-limiting growth deposition at 450 °C results in the nucleation of monolayers charge transfer between MoO₃ and SrTiO₃ stabilised the interfacial layer

Table 1: The summary of growth characteristics of MoO₃ mono- to few layers on various substrates according to cited references.

synthesis [75], as well as oxidation of a Mo layer [22,76,77,79,80] and transformation from MoS₂ to MoO₃ [66,81]. The formation of MoO₃ ultrathin films was also usually followed by post-deposition annealing in oxygen atmosphere [22,72,73].

Table 1 summarises morphology and growth characteristics of molybdenum oxide ultrathin films with an emphasis on defining monolayer structure depending on the surrogate substrate. The prior works provide a guide for synthesising MoO₃ nanosheets with specific shapes and distributions, while Au substrate was studied in the most comprehensive approach so far [22,76–79]. The first layer (also called buffer layer) of MoO₃ on Au is distinguished from the next layers and bulk α -MoO₃ [22,76,77,79]. Most of the first layers were reported to consist of mostly Mo on 6+ oxidation state with some percentage of atomic concentration of 5+, which is given in Table 1.

In terms of achieving monolayer films on large scale, the study of Wang *et al.* [74] showed that vdW epitaxy by ambient pressure physical vapour deposition (APPVD) is a simple and effective method to fabricate ultrathin α -MoO₃ nanosheets of lateral sizes of several tens of micrometres. Bigger lateral dimensions of centimetres – unbeatable record so far – were offered by the hot plate method established by Molina-Mendoza *et al.* [44], which requires less complex setups than other large-scale synthesis methods like the chemical vapour deposition (CVD) or molecular beam epitaxy (MBE). The key to achieving large-scale monolayer films of α -MoO₃ may be a self-limiting process reported by Du *et al.* [72] and its translation to other surrogate substrates.

Based on above examples, the use of vdW layered materials, such as mica or graphene, as growth templates allows growing laterally aligned 2D MoO₃ layers. The vdW interaction between the substrate and MoO₃ relaxes the lattice mismatch, thus promoting vdW epitaxial growth of MoO₃ layers. Allowance of lateral growth is in contrast to other substrates including Si and glass [82]. Due to surface dangling bonds, those growth templates promote, e.g., horizontally aligned MoO₃ nanobelts among other structures [82].

In two recent papers, Kim *et al.* [70,71] reported on 2D single-crystal (square-like) MoO₃ nanosheets on multilayer graphene (graphite). However, the thinnest measurable MoO₃ nanosheet was bilayer due to instability of irregularly shaped monolayer with the thickness of approx. 0.7 nm, as suggested in their first paper. The growth of the 2L MoO₃ films was in ambient conditions. The multilayer MoO₃ of rectangular shape on graphene was also reported therein [70] and by Cai *et al.* [75]. Interestingly, many of 2L to few-layer MoO₃ properties were reported to be independent of the number of layers such as friction, dielectric constant, and work function (4.73 eV in ambient) [71]. In contrast, the band gap increased from 2.9 (for bulk) to 3.2 eV (for the thinnest portion measured) as the thickness decreased [71]. This is in conflict with

theoretical expectations, where no thickness dependence of the band gap in α -MoO₃ should be observed because of weak interlayer interaction [44].

We find the ability to synthesise two-dimensional high-quality α -MoO₃ films under UHV conditions superior, as it allows direct *in-situ* characterisation. Thus, it can lead to fundamental research and a great advance in our understanding of their properties. Thermal evaporation in UHV is the method of our choice and was used to obtain results presented in this work.

Moreover, the ability to grow α -MoO₃ films in a controllable fashion on more substrates from graphene family opens possibilities for practical applications in organic electronics. This is especially prospective due to, as mentioned, the reported synthesis of large-scale 2D α -MoO₃ up to centimetres on other substrates [44,74,75,83] or wafer-scale in case of amorphous films [84].

1.3.3. Rhenium Oxides

Rhenium oxides are of high importance for their wide applications as they are the most common precursor for catalyst preparation and the synthesis of metalorganic compounds [55,85]. Their high work function (reaching 7 eV) is vital for both classes of their applications: electronics and catalysis [55]. Rhenium heptoxide is known for its high catalytic activity in olefin metathesis as well as the only catalyst working efficiently at room temperature [86].

Rhenium exists in at least five oxidation states: 7+, 6+, 4+, and 3+ [87]. The oxides with Re²⁺ is uncommon, and high valent species are more stable. The stable binary oxides are ReO₂, ReO₃ and Re₂O₇. When exposed to air the oxides may form a surface layer of Re₂O₇ [88], as Re₂O₇ is thermodynamically most stable. While ReO₃ has a melting point at about 340 °C [26,89], Re₂O₇ sublimates at lower temperature of about 225 °C [89]. Rhenium in the highest oxidation state form Re₂O₇ in yellow angular crystals. UV–visible absorption spectroscopy indicated that Re₂O₇ has an absorption at 405 nm (3.06 eV), which is responsible for its yellowish colour [90]. Re₂O₇ is highly hygroscopic [90] which presumably affects its properties after contact with moisture in ambient conditions.

Crystalline Re₂O₇ is an electrically insulating material [91], with a predicted direct bandgap of 2.9 eV [92]. Both phases of ReO₂, low-temperature monoclinic phase α -ReO₂ and high-temperature orthorhombic phase β -ReO₂, have metallic conductivity [91]. Similarly, ReO₃ is a red solid with a metallic character.

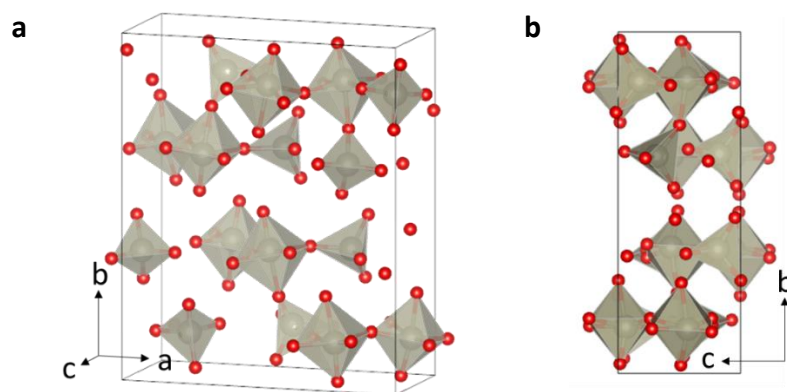


Figure 2: Crystal structure of Re_2O_7 . Unit cell structure model taken from [93]. **(a)** standard orientation of crystal shape **(b)** side view of Re_2O_7 .

The structure of Re_2O_7 is layered with top oxygen to oxygen vdW contacts in between layers – note that the unit cell is cut half by this vdW gap in b direction (see Figure 2a and b). The two layers building a unit cell and consist of subunits interconnected through the corners of the octahedrons [94]. The lattice parameters are $a = 12.5 \text{ \AA}$, $b = 15.2 \text{ \AA}$, and $c = 5.4 \text{ \AA}$ [94].

Lawler *et al.* described the molecular and electronic structure of Re_2O_7 [92]. Considering theoretical studies of ReO_3 , the electronic structure and the relation between its structural and electronic properties are well described in [55,95]. In particular, (001) surface of ReO_3 was reported to offer the possibility of tuning its work function from initial 7 to 3 eV by controlling the concentration of oxygen vacancies; the more vacancies, the lower work function [55]. It was also observed experimentally by Baikie *et al.* [28], who presented that oxidation substantially increases the work function of rhenium metal from clean 5.1 eV at room temperature to as high as 7.1 eV at around 525 °C. Zhou *et al.* [29] focused on tri-rhenium oxide clusters and computationally analysed the chemical bonding, and elucidated electronic and structural evolution in these clusters. More recently, Wang *et al.* predicted hourglass Dirac chain metal realising in ReO_2 [96]. Comprehensive information about rhenium and its oxides can be found in [97].

Due to the rich chemistry of rhenium oxides, it is worth mentioning that based on the literature, the database for chemical analysis of these oxides suffers from inconsistency in the reported binding energies of Re4f. For example, the $\text{Re}4f_{7/2}$ binding energy has been reported between 45.4–46.9 eV [98–100]. Thus, in this work, we support our XPS Re4f interpretation on a comprehensive, *in-situ* studies by Greiner *et al.* [88].

1.4. Graphene & HOPG

Graphene, a monolayer-thick allotrope of carbon, was initially investigated in 2004 [101], and is a 2D material having exceptional physical properties. Notably, in the K/K' corners of the

hexagonal Brillouin zone, the valence and conductance bands of graphene show a linear dispersion relation precisely crossing at the so-called Dirac points [16,17]. This behaviour is similar to massless relativistic particles described by the mass-less Dirac equation and leads to treating graphene as a zero-gap semiconductor. The new papers suggest that graphene description by the quantum electrodynamics theory [16,17,101,102] is more accurate than the nonrelativistic Schrödinger equation. This application notably predicts high mobility of charge carriers due to the pseudospin conservation rule as well as high optical transparency in the visible light, making this material promising for flexible optoelectronic applications [16,17].

The properties and variety of graphene fabrication methods have been summarized in review papers such as [10,14,16,103]. More on graphene as a flexible electronic material can be found in reviews on mechanical limitations related to structural defects induced during synthesis [104,105] and transfer [106].

In the ongoing research, it has been shown that graphene may have its electronic properties easily adjusted in a broad spectrum [19]. Therefore, it can be used as a base for complex systems such as heterostructures. These modifications include properties like doping level, band gap width and modification of the dispersion relation. The background of graphene heterojunctions is broadly covered in [107,108]. For example, the introduction of dopant atoms into the graphene lattice or deposition of inorganic and organic layers can cause the mentioned modifications [19,52,109].

In the focus of this work, graphene is the most promising thin film electrode as a replacement for ITO. The relatively low work function of graphene of 4.2–4.6 eV [19,20] is one of the major limits for the energy level alignment in organic electronic structures. The most commonly used method to solve this issue is the mentioned modification of graphene by combining it with additional layers of high work function films such as TMOs. This opens a platform to tune the work function value to desired level.

As the first step in this direction, we aim to use a HOPG surface as a model graphene system. Graphite is, in principle, a bulk material consisting of many graphene layers forming vdW structure. An exposed HOPG(0001) surface is a perfect model graphene layer on a graphite substrate, providing repeatable quality. HOPG was previously used as a prototypical inert and atomically flat template for the vdW epitaxial growth of numerous crystalline nanomaterials [41,110,111]. Thus, HOPG is ideal for studying the growth of 2D MoO_3 layers and should hold promise considering its compatibility with characterization techniques such as scanning tunnelling microscopy/spectroscopy (STM/STS) and high-resolution transmission electron microscopy (HR-TEM).

2. Experimental Methods

This Chapter presents the experimental equipment, TMOs sample preparation details, and describe the substrates used in this study. A series of techniques was used in this work in order to characterise and understand the morphology, crystal and electronic structure, as well as chemical composition of prepared materials. Background information about characterization techniques is not included; the principles of used techniques are well known and available in the literature, such as about STM/AFM microscopy in refs. [112,113]. Thus, only the technical aspects are covered in this Chapter.

The presentation of relevant operating parameters, their ranges, and details of the analysis of experimental results is intended to not only allow other researchers to reproduce the results but also work as optimal initial values for either TMOs evaporation, substrate preparation or data analysis.

Work function determination for 2D materials require more attention from the perspective of this study. Therefore, we provide a commentary on UPS measurement for monolayers, to provide a practical guide for the determination of high WF attributed to 2D islands on a substrate with relatively lower WF. We address complications associated with double secondary electron cut off due to insufficient coverage based on UPS analysis of various lateral area ratios between 2D-MoO₃ islands and HOPG.

2.1. Ultra High Vacuum Systems

Majority of experimental results presented in this dissertation were obtained at three UHV systems at Department of Solid State Physics, University of Lodz.

TMOs were thermally evaporated in two dedicated UHV systems, while the following characterization was performed in the third UHV system. The latter, Multiprobe P Scienta-Omicron with a base pressure of 5×10^{-10} mbar, is equipped with the Omicron VT STM/AFM microscope, LEED optics, and hemispherical analyser for XPS, UPS and ARPES. Figure 3a shows the UHV Multiprobe P system. The system is interconnected with other UHV systems (see below) using vacuum suitcase (base pressure of 5×10^{-8} mbar) shown in Figure 3b (highlighted blue).

The other UHV systems are dedicated to deposition of TMOs. The UHV system by Prevac of base pressure of 3×10^{-8} mbar is used for molybdenum oxides – see Figure 4a. The OXFORD Instruments system (base pressure of 7×10^{-10} mbar) is used for rhenium oxides deposition – Figure 4b. In both cases growth rate was monitored using a quartz crystal microbalance (Quartz Monitor QM20, EDF-electronics).

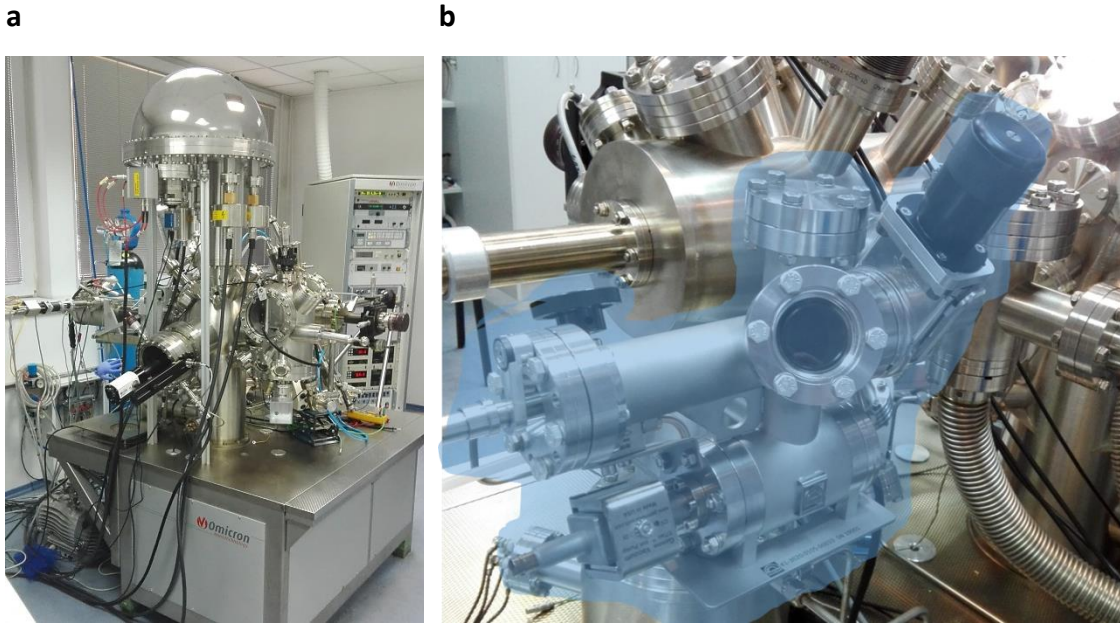


Figure 3: UHV facilities at University of Lodz (a) Multiprobe P Scienta-Omicron UHV system dedicated to characterisation and post-processing including annealing. **(b)** vacuum suitcase highlighted blue while attached to the Load Lock of the Omicron system (a).

2.2. Sample Preparation: Thermal Evaporation

Deposition of films was performed by thermal evaporation in UHV conditions – a simple bottom-up method, which belongs to Physical Vapour Deposition (PVD) techniques. Basically, material placed in a crucible is heated until its atoms have sufficient energy to leave, producing gas phase material. At this point they will traverse the chamber in UHV, and coat a substrate positioned above the evaporating material.

A representative effusion cell (Knudsen cell) is shown in Figure 4c (highlighted blue) when assembled at the Prevac system (Figure 4a). To present the whole instrument, a design drawing of effusion cell is shown in Figure 4d. Generally effusion cell utilizes a containment crucible (made of, e.g., Al_2O_3 , Mo or W) which is surrounded by a heat source coiled around the crucible such as a tungsten or tantalum resistance wire. Crucibles are heated in a controlled fashion utilizing a thermocouple sensor, integral water cooling if applicable, and a heater controller. Thereby, the source powder material is heated and evaporates from the open end of the crucible if a shutter is open. The evaporation rate is controlled with power input (equivalent to heating element temperature).

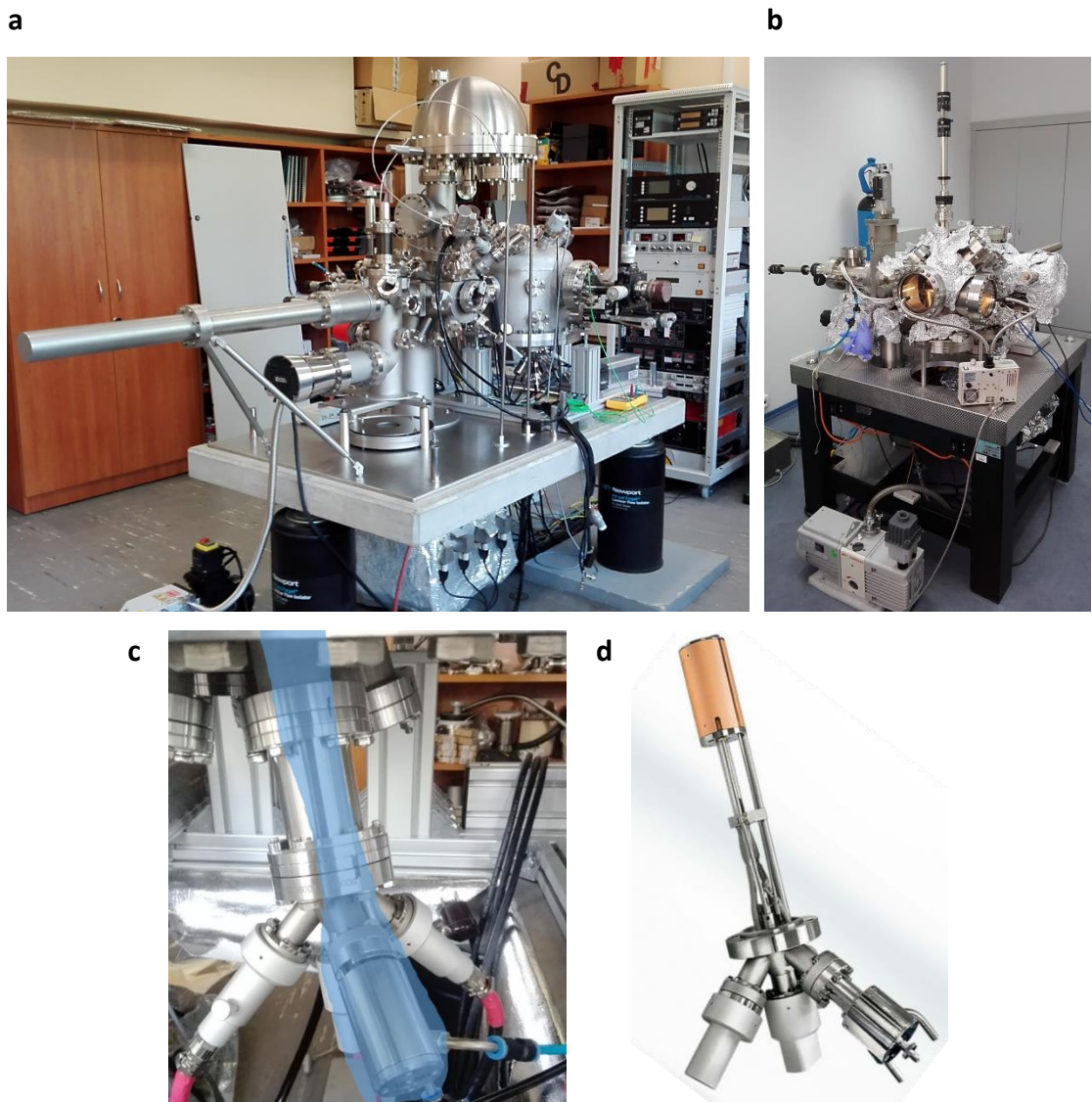


Figure 4: UHV facilities at University of Lodz dedicated to sample preparation including TMOs deposition. (a) UHV system used for molybdenum oxides, Prevac, equipped with home-made cleaving tool for HOPG in the Load Lock, and heating of substrates during deposition **(b)** UHV system used for rhenium oxides, OXFORD Instruments. **(c)** Effusion Cell (Knudsen Cell) for thermal evaporation of TMOs, highlighted blue while assembled at the Prevac system (a). **(d)** design drawing of effusion cell adapted from www.precvac.eu.

2.2.1.Substrates: Graphite and Graphene

In this Thesis the following substrates have been used:

- I. HOPG(0001), ZYA grade – treated as graphene-like substrate contributing to fundamental understanding of the nature of graphene/MoO₃ heterostructure, and most importantly providing repeatable quality substrate surface.
- II. For MoO₃ heterostructures, graphene monolayers were synthesized by chemical vapor deposition (CVD) method on copper foil (Cu) substrates and silicon carbide

6H-SiC(0001) using AIXTRON reactor at *Łukasiewicz Research Network – Institute of Electronic Materials Technology, Warsaw* [114]. While few-layer graphene on SiC was fabricated by graphitising SiC surfaces in Si flux [115] (BeeGraphene) at Jagiellonian University, Cracow.

- III. For Re_2O_7 heterostructures, the graphene layers were synthesized by CVD method on 6H-SiC(0001) substrate using AIXTRON reactor at *Institute of Electronic Materials Technology, Warsaw* [114]. The graphene was hydrogen intercalated, i.e. consists of bilayers (hereafter referred to as graphene) and exhibited p-type doping.

2.2.2. Molybdenum Oxide on HOPG and Graphene

Molybdenum oxide was deposited on HOPG substrate or graphene (on Cu and SiC) by thermal evaporation using Knudsen effusion cell from MoO_3 powder source (Sigma-Aldrich). The temperature of the effusion cell was maintained at 330 °C for evaporation – the power input was controlled manually and after reach the desired temperature by utilizing PID controller.

In the case of a HOPG substrate, it was first introduced into UHV system to be cleaved in base pressure of 5×10^{-8} mbar. After cleavage, the substrate was immediately introduced into the next chamber (base pressure of 3×10^{-8} mbar), where it was annealed at 330 °C for at least 1 h (counted from reaching the temperature) prior to MoO_3 film growth. The HOPG substrate was held at 220 °C for MoO_3 growth.

In the case of graphene, the graphene samples were treated differently depending on their substrates. Graphene on Cu foil was UHV annealed at 350 °C for at least 1 h in order to remove atmospheric contaminations. Then, the MoO_3 growth was on the heated substrate kept at 265 °C. Graphene on SiC was UHV annealed at 440 °C for at least 1 h, and the MoO_3 growth was on the heated substrate kept at 220–250 °C.

2.2.3. Rhenium Oxide on Graphene

Re_2O_7 was deposited on graphene substrate by thermal evaporation using Knudsen effusion cell from powder source of ReO_3 (Sigma-Aldrich). The graphene substrate on SiC was first annealed at 300–350 °C for at least 1 h prior to the oxide deposition. Re_2O_7 was evaporated on the substrate held at room temperature. The temperature of the effusion cell was maintained at 260 °C for evaporation – the power input was controlled manually.

Fabrication of graphene heterostructures with Re_2O_7 is possible because ReO_3 in solid phase is unstable at temperature above 300 °C in vacuum, in consequence it decomposes by disproportionation thermal reaction into Re_2O_7 (gaseous phase) and ReO_2 (solid phase) [13,116].

2.3. Material Characterisation

The majority of the characterisation measurements were performed in the UHV Multiprobe P Omicron system at room temperature (RT), see Figure 3a.

STM and AFM measurements were performed with VT-STM/AFM microscope, Omicron. For STM a mechanically cut tip (90% Pt–10% Ir, Goodfellow) was used. Typically, STM scans were acquired at a positive bias in the range of 0.2–0.6 V and current 0.1–0.3 nA. In STS technique, current imaging tunnelling spectroscopy mode (CITS) or STS mapping, the I/V curves are recorded with topography by the interrupted-feedback-loop technique. The STM data was processed with WSxM 5.0 DEVELOP 7.0 [117], Gwyddion software [118], and Modular Analyse System (MAS) ver. 2.6.07.374, which is being developed at University of Lodz by Dr. Pawel J. Kowalczyk, DSc, prof. UL. The statistical data of step heights was extracted from images in a form of height histogram from area that was as big as possible when consisting of one step, i.e. MoO₃ nanosheet on HOPG.

LEED data were acquired by OCI Vacuum Microengineering Inc. spectrometer with energy set to 55 eV at RT for MoO₃ layers. The surface lattice constants of MoO₃ could be calculated from the diffraction rings, using the graphite first-order diffraction ring as a reference of known diameters.

A hemispherical energy analyser Phoibos 150 (SPECS) with 2D-CCD detector was used for photoelectron spectroscopy measurements. The pass energy was set to 30 eV and 5 eV for XPS and UPS measurements, respectively. The DAR 400 X-ray source with Mg K α (1253.64 eV) non-monochromatic radiation was utilised in XPS measurement. UPS measurements were performed with the Helium I line (21.22 eV) of VUV Source HIS 13 (Focus GmbH) with a sample bias of -3.1 V. The energy calibration was conducted at the Fermi level (E_F) of Au(111). At the pass energy of 5 eV, we determined the energy resolution of \sim 100 meV for the settings used in this study for finding secondary electron cut-off positions (step size of 0.01 eV).

Analysis of the photoemission spectra was performed in CasaXPS software. In UPS, the work function values were derived from the intersection of linear extrapolation of a steep edge of secondary electron cut-off (SEC) with the background, i.e., Edge Up background type provided in CasaXPS. More information about analysing two-component surfaces can be found in the next Section 2.4.

All the XPS spectra were calibrated using C1s peak (284.5 eV). The XPS data analysis involved Shirley background subtraction, curve-fitting, and peak area determination based on given elements. In the case of Mo3d, a mix of Gaussian–Lorentzian function was used, with 85%

of Gaussian. The Mo3d region was fitted by two doublets (Mo^{6+} and Mo^{5+}) with fixed parameters: spin-orbit separation (3.1 eV), ($3d_{3/2}$):($3d_{5/2}$) intensity ratio (0.67) and full width at half maximum constraint (FWHM = 1.8 eV). Binding energies of particular Mo oxidation states are given in Appendix A (see page 109). In the case of Re4f, a mix of Gaussian–Lorentzian function was used, with 75% of Gaussian. The Re4f region was fitted by three doublets with fixed parameters: spin-orbit separation (2.4 eV), ($4f_{5/2}$):($4f_{7/2}$) intensity ratio (0.75) and FWHM from 1.77 to 1.95 eV.

NT-MDT Ntegra Aura system was used for AFM and STM measurement in ambient conditions.

External measurements without much of specific parameters are following. HR-TEM measurements were performed at the National Center for High Resolution Electron Microscopy (nCHREM) at Lund University. Details of HOPG/ MoO_3 samples, their transport and preparation can be found in [67]. Raman studies were performed at Łukasiewicz Research Network – Institute of Electronic Materials Technology by the use of Renishaw inVia Raman Microscope in ambient, at RT, and with a 532 nm laser with an average power about 5 mW [20].

2.4. UPS Work function Measurements in UHV: Uncoalesced 2D Films

For the sake of providing practical guide for interpretation of work function measurements on uncoalesced 2D films or nanosheets, we comment on UPS measurement on monolayer (1L) MoO_3 nanosheets on HOPG. Despite the usefulness of UPS [6,19,20,37,41,43], there is little discussion on conducting measurements on patchy or multicomponent samples with laterally heterogeneous work function (WF). The available discussions have focused on patchy samples, where patches derive from dirt or designed patterning [33,41,119–121]. In contrast, our setup is a perfect system to discuss the limitation of this technique for heterogeneous systems.

In the case of UPS, WF is extracted based on the width of an observed spectrum versus photoelectron energy [119,120]. The spectrum, on the one hand, starts with high-energy electrons coming from the Fermi level; on the other hand, it ends with low-energy electrons whose limit to leave the sample is the work function (at SEC). When calibrated to vivid Fermi energy of clean metal surfaces, as in our case Au, the SEC position on the kinetic energy scale indicates the work function of the material. The low-energy end of the photoelectron spectra is observed as step edges, where the SEC position is read from the point where the edge merges into the background.

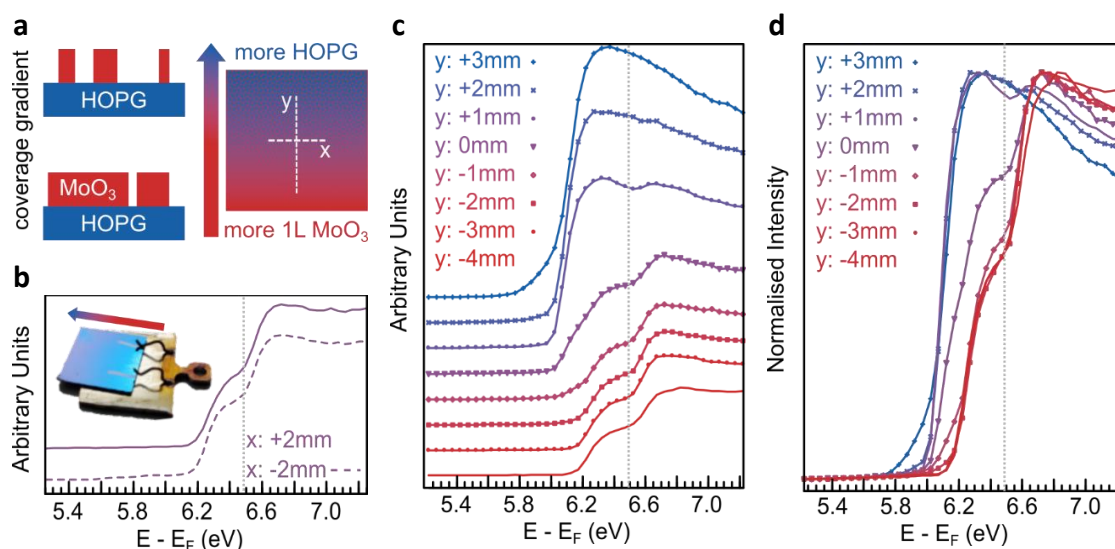


Figure 5: Series of He I UPS spectra of HOPG/MoO₃ multicomponent surface of different area ratio of HOPG and monolayer (1L) MoO₃ patches. (a) illustration of a patchy HOPG/1L-MoO₃ sample structure; UPS measurements were taken along marked lines in *x* and *y*: secondary electron cut-off (SEC) region with a range of spectra taken at various points across the sample in intensity arbitrary units (**b and c**) and normalised intensity (**d**). The *x*-axis of photoelectron energy is calibrated to Au Fermi level ($E - E_F$), corresponding to work function. The vertical lines indicate the positions of high-energy SECs. Inset in (b) represents gradient of MoO₃ surface coverage – additional photography was taken on SiO₂ substrate for visualization.

We present a real-life experiment, where area of patches with different WF depends on the sample morphology (see also Figure 29). Our test sample has a topography of randomly distributed 1L MoO₃ nanosheets of different shapes, where patches of HOPG remain uncovered. In our deposition setup, we can obtain a gradient of deposition coverage – see Figure 5a illustrating the HOPG/1L-MoO₃ area coverage from dense (red, MoO₃) to scarce (blue, HOPG). For visualization, an additional photography was taken on similar sample but on a SiO₂ substrate, where a thicker film interference pattern is observed due to the gradient – see inset in Figure 5b. Due to coverage gradient on HOPG samples, we can provide the UPS results from the various area ratio between 1L MoO₃ patches and exposed HOPG.

At UPS spectra, with fractional coverage by 1L MoO₃ the SEC does not take a typical step edge shape but may consist of two components (two edges) observed at lower and higher energy. The first SEC at low energy can be assigned to an apparent WF value of both materials HOPG and MoO₃, while the second SEC at high energy corresponds to MoO₃ only. The explanation of the observed effect is well described by Schultz *et al.* [119]. The double SEC is explained by electrostatic potential distribution due to the presence of two components on the surface.

We took a range of spectra at various points (see lines *x* and *y* in Figure 5a) to show how acquired UPS spectra can vary in such conditions. Within the horizontal line *x*, where coverage is expected to be similar, the UPS spectra are consistent – see Figure 5b. On the contrary, when HOPG/1L-MoO₃ area ratio varies – vertical line *y* in Figure 5a – the UPS spectra significantly change. Figure 5c presents SEC region with that series of spectra, while Figure 5d replots them with normalised intensity to highlight the positions of high-energy SECs, which are marked by the vertical lines on all plots. The high-energy SEC, related to WF of MoO₃ is observed in the same position for all the spectra regardless the HOPG/1L-MoO₃ area ratio. However, the shift in the low energy SECs is clear (about up to 200 meV) as well as change in SEC shape, width, and relative intensities of distinct SECs depending on a HOPG/1L-MoO₃ pattern within the probed area. Regarding the latter, note that if the area covered by MoO₃ is insufficient to contribute and build up a distinct high energy SEC, a spectrum reveals only one broad SEC giving no significant information about any distinct material [119] – see the top blue spectrum in Figure 5c and the only spectrum lacking the second component in Figure 5d. Then the MoO₃ contribution is hidden and the single broad SEC reveals work function higher than bare HOPG and lower than MoO₃. It is higher than it would be for HOPG due to higher additional electrostatic barrier as a result of the presence of MoO₃ nanosheets. In order to elaborate on usability of UPS for WF determination of 2D islands, some useful information can be deduced from these measurements as listed below:

- I. for different spots on the sample, i.e. different ratios of two materials, the high-energy SEC is uniformly located [119] at ~ 6.50 eV, thus is determined as absolute value of work function of high-WF material, here MoO₃;
- II. the energy of the low-energy SEC shifts, thus it is dependent on area ratio between MoO₃ and exposed HOPG, as the position of low energy SEC is governed by electrostatic potential distribution above a two-component surface [119];
- III. with the low-energy SEC shifting towards lower energy, the relative intensities of the peaks change, i.e. the contribution from HOPG increases, thus, the intensity of the low-energy SEC increases; alike, the overall intensity of a spectrum in SEC region increases as well [119] – the same variation in SEC was found by Sharma *et al.* [120] for patches composed of ITO and Au;
- IV. there is a minimal area of high-work-function material required for observation of a distinct high-energy SEC. Sharma *et al.* [120] determined that only with coverage higher than 60% there is identifiable contribution of higher work function material. In our case, we do not quantitatively determine such

requirement, however, we also recognised broad spectra without distinct components, which we attribute to an insufficient area of MoO₃.

2.5. KPFM Work function Measurements

Frequency-modulated KPFM experiments were performed with Omicron Matrix system and Nanonis controller (SPECS). Contact potential difference (CPD) maps were obtained simultaneously with topography non-contact-AFM (nc-AFM) operating in UHV. In ambient conditions, NT-MDT Ntegra Aura system was used for KPFM conducted using a two-pass technique. A freshly cleaved HOPG was used as a calibration sample before and after the measurement of MoO₃ to ensure uniform tip condition and correct calibration. The calibration value varied by 3 mV, thus the measurement error is mostly affected by tip-sample distance, especially at steps. Autoreference was used if applicable – for HOPG/1L-MoO₃ samples with uncovered substrate.

CPD is directly related to work function differences. The work function of MoO₃ was calculated with respect to the work function of HOPG measured using UPS ($\Phi_{HOPG} = 4.5$ eV) according to the following equation (1):

$$\Phi_{MoO_3} = \Phi_{HOPG} + e(CPD_{HOPG} - CPD_{MoO_3}) \quad (1)$$

where e is the elementary charge. The KPFM images were processed using Gwyddion software [118].

2.6. Computations & software

The experimental work was supported by calculations as a result of collaboration within the Department of Solid State Physics at University of Lodz with dr. Karol Szalowski, DSc, prof. UL. The first-principle calculations based on Density Functional Theory (DFT) were carried out with QUANTUM ESPRESSO software [122,123]. Details of data presented in Chapter 3 can be found in [67]. Drawings of crystal lattice were produced by VESTA [124]. LEED patterns were simulated in LEEDpat, Version 4.2 [125].

3. α -MoO₃ Monolayer Grown on Graphite Substrate

This Chapter presents the possibility of development van der Waals (vdW) heterostructures based on graphene-like substrates and stable metal oxide monolayer.

The results shown here will serve as a reference for the further analysis presented in the thesis. The Chapter is devoted to monolayers of molybdenum trioxide in the α phase (α -MoO₃), where we disseminate the possibility to synthesise slightly nonstoichiometric MoO₃ on highly oriented pyrolytic graphite (HOPG). HOPG was chosen as it mimics the physical and chemical properties of graphene as a substrate for MoO₃ growth. At the same time, HOPG is a highly repeatable and nearly defect-free substrate in contrast to any available graphene. Such MoO₃ is electrically conductive while maintaining its two-dimensional (2D) character.

Most of the results discussed in this Chapter have been already reported in the article entitled '*Local electronic structure of stable monolayers of α -MoO_{3-x} grown on graphite substrate*', published in 2D Materials on November 13, 2020 [67]. The transmission electron microscopy (TEM) measurements and density functional theory (DFT) calculations were performed by Domagoj Bielić and Karol Szałowski, respectively. The author acknowledges their contribution.

The work is the first to report stable 2D MoO₃ with monolayer (1L) thickness directly grown on HOPG. That stability is in stark contrast to previously available results on graphene describing mobile 1L MoO₃ [70,71]. Our results are obtained under ultra high vacuum (UHV) and provide scanning tunnelling spectroscopy (STS) information on the electronic properties of MoO₃ on the first three layers. To our knowledge, STS measurements have been previously reported only on bulk molybdates. Due to the future application of graphene/MoO₃ heterostructures in flexible electronics, the studies of the electronic structure of monolayer MoO₃ at the nanoscale play a crucial role, where a HOPG surface works as a model of a graphene system. The presented approach is in line with previous studies, where HOPG has been used extensively as a prototypical substrate for the vdW epitaxial growth of 2D materials [41,110,111].

The aim of the presented research is to synthesise monolayers of MoO₃ on the graphene-like substrate and investigate its electronic structure. This Chapter presents an introduction to the electronic structure of MoO₃ and answers the following questions:

- I. Is it possible to synthesise crystalline α -MoO₃ with monolayer thickness on a graphene-like substrate? Is thermal evaporation under UHV a suitable method to obtain such layers?

- II. What is the stoichiometry of MoO₃ layers obtained by UHV evaporation? Are any defect states induced in the bandgap according to possible oxygen deficiency?
- III. Is there any particular difference between the first few layers of MoO₃? What is the energy gap for the first few layers of MoO₃ on HOPG?
- IV. How does the bandgap states and work function (WF, Φ) of UHV obtained MoO₃ monolayers change upon air exposure?

3.1. Introduction

Monolayers of MoO₃ have been previously grown on atomically flat substrates, e.g., graphene [70,71], mica [70,75], hBN [70], or SrTiO₃ [72], as described in Section 1.3.2. In particular, Kim *et al.* [70,71] reported few-layer MoO₃ nanosheets growth on graphene (multilayer graphene or graphite) using so-called hot plate method. Due to instability of 1L MoO₃, the thinnest measurable MoO₃ structure possessed two layers. Irregularly shaped 1L MoO₃ was mobile; however, its thickness appeared to be approx. 0.7 nm by AFM [70]. Note that in those experiments: both the growth and AFM characterisation, were carried out in ambient conditions.

Extensive photoemission spectroscopy (PES) studies were widely conducted on reduced molybdates to understand the influence of substrate as well as charge transfer [38–40,68]. In particular, Greiner *et al.* [38] focused on how metal contacts affected the properties of MoO₃ and elucidated how they induce Mo4d gap states at the interface leading to making MoO₃ semimetallic or metallic. They attributed this interface's reactivity to the oxygen and electron chemical potential difference between MoO₃ and the substrate. The former induces oxidation or reduction reactions, while the latter reduces Mo⁶⁺ through charge transfer with the substrate. In addition, the formation of Mo4d gap states decreases the work function while increasing the conductivity [19,38,69,126]. Similar to other transition metal oxides (TMOs) [20], these effects are confined to a few nm of the MoO₃ film from the substrate [6,19,37,38], which may be an advantage of MoO₃ in 2D form. PES has also indicated that the graphene/MoO₃ interface exhibits non-negligible reactivity. It has been reported that contact with graphene results in a 0.3 eV shift in the valence band edge of thin MoO₃ films [6,19]. Wu *et al.* [6] and Meyer *et al.* [19] made important advances in analysing graphene/MoO₃ heterostructures, reporting that the heterostructure's work function can be tuned to high values by increasing the thickness of MoO₃ films.

A clear trend can be derived from previous PES results [16–19,41,42] from distinct yet broad peaks built by emission from gap states in oxygen-deficient MoO₃ in the range of 2 eV.

The trend is clear considering a transition from MoO_2 to final MoO_3 . Upon oxidation, the peaks evolved in three following steps:

- I. doublet at 0.4–0.5 and 1.6–1.7 eV, which in some cases fell to 0.0 eV (accompanying Mo^{4+});
- II. rather broad peak at 1.1 eV (accompanying Mo^{5+});
- III. peak at 0.8–0.9 eV (accompanying nearly stoichiometric MoO_3).

At the graphene/ MoO_3 interface, an additional emission was indicated at 0.9–1.0 eV (local maximum) [6,19]. A comprehensive but not conclusive discussion on the nature of defects in molybdates is given in [68,127], while the gap states are discussed in [43,128].

Even though the molybdates band structure has been investigated via PES and widely discussed, there are surprisingly scarce experimental reports on their local electronic structure. Among molybdenum oxides, STS measurements were acquired for the cleaved $\text{Mo}_{18}\text{O}_{52}$ [63] as well as Mo_8O_{23} [129] crystals. Interestingly, Smith and Roher [63] have observed distinctive differences in probing unfilled states of $\text{Mo}_{18}\text{O}_{52}$ in relation to its topography. Nasretdinova *et al.* [129] have presented a complex Mo_8O_{23} electronic structure with various phenomena such as metal-to-insulator transformation and the formation of charge density waves. Moreover, Kim *et al.* [71] have suggested that MoO_3 is an excellent candidate for tunnel barriers by demonstrating tunnel current gaps by conductive AFM for few-layer MoO_3 films, i.e. 1.6 V for bilayer, 2.8 V for trilayer. In contrast, a comprehensive analysis of the nanoscale electronic properties of 2D α - MoO_3 on HOPG has not yet been conducted. Yet, investigations of these heterostructures under UHV conditions are missing.

All the above make the graphene/ MoO_3 system attractive for fundamental research on the electronic properties of the first few MoO_3 layers on the nanoscale using scanning tunnelling microscopy (STM) and spectroscopy. Herein, in controlled UHV conditions, we used HOPG as a model platform to study graphene/1L- MoO_3 heterostructures.

In contrast to previous results [70,71], we present stable 1L α - MoO_3 that covers the HOPG substrate nearly uniformly. This layer stability enables precise scanning probe microscopy (SPM) characterisation with STM and contact atomic force microscopy (c-AFM) under the UHV conditions, minimising possible contamination and oxidation of the MoO_3 films. First, we present the crystalline lattice structure of α - MoO_3 nanosheets determined by TEM and low-energy electron diffraction (LEED) measurements. Combining ultraviolet and X-ray photoelectron spectroscopies (UPS and XPS), we examine the chemical composition of HOPG/ MoO_3 and the interface-induced defects states. The nanoscale characterisation by STM/STS permits us to investigate the local electronic structure of the first layers (1 to 3L) of α - MoO_3 on HOPG.

In addition, we investigate the effect of air exposure on 1L MoO₃. After air exposure, we perform STM/STS characterisation without any cleaning procedure. We demonstrate the differences in the electronic structure due to exposure to air, while in contrast, the atomic structure is fully preserved. Our findings shed light on the heterogeneity of the electronic structure of the first MoO₃ layer at the interface with the substrate, which contributes to the fundamental understanding graphene/1L-MoO₃ system. Finally, using UPS, we study the work function of HOPG/1L-MoO₃ before and after exposure to air.

We support the analysis of experimental results by theoretical predictions of crystallography and electronic structure dependence on a number of layers of MoO₃.

3.2. Results and Discussions

3.2.1. Stable Monolayer of MoO₃: Morphological and Crystallographic Characterisation

It has been demonstrated previously that the first monolayer of MoO₃ grown on multilayer graphene was highly mobile due to weak interaction with the substrate [70,71]. The reference to layers corresponds to known α phase of MoO₃, where 1L is attributed to half of out-of-plane lattice parameter of a single unit cell [39,46,63] (see Figure 1). As mentioned instability hindered characterisation of 1L material and limited potential ultrathin applications, we decided to study growth processes in fully controllable conditions, i.e. UHV, and directly on contamination free and repeatable substrate. We thermally evaporated MoO₃ monolayers on HOPG, kept at 220 °C – for details see Experimental Section 2.2.2. The success of our process lies in the ultraclean substrate due to cleaving top layer of HOPG in UHV prior to growth. This technique leads to crystalline and stacked MoO₃ nanosheets. Such 1L MoO₃ films are stable and allow characterisation by STM and c-AFM in UHV.

Typically shaped monolayer MoO₃ nanosheets are shown in a large-scale STM image in Figure 6a. The 1L nanosheets are characterised by curved edges. For 2L nanosheets, we observe another type of morphology – rectangular for relatively small nanosheets, which seem to be common (see a framed region of stack layers in Figure 6a and Figure 6b). However, for larger area nanosheets, also irregular shapes alike the 1L were rarely seen – marked on c-AFM images provided in Figure 6c. The rectangular morphology of 2L nanosheets of MoO₃ is in line with previous reports [70,71,74,75].

MoO₃ forms 1L nanosheets at submonolayer coverages, which preferentially (yet not exclusively) nucleate at the steps or domain edges of the substrate. Typically, MoO₃ grow over HOPG steps, i.e. on neighbouring terraces. This can be observed in topographies in Figure 6a-c,

which show numerous MoO₃ nanosheets attached to step edges and a few free-standing nanosheets that presumably nucleated at morphological defects. While the first layer tends to cover the majority of the substrate surface, nucleation of the second layer, similarly, starts at HOPG step edges. The multilayer ($\geq 3L$) nanosheets are detected at presumably large morphological defects. Figure 6d shows higher MoO₃ coverage, where the surface is covered by numerous stacked nanosheets of rectangular-like shapes.

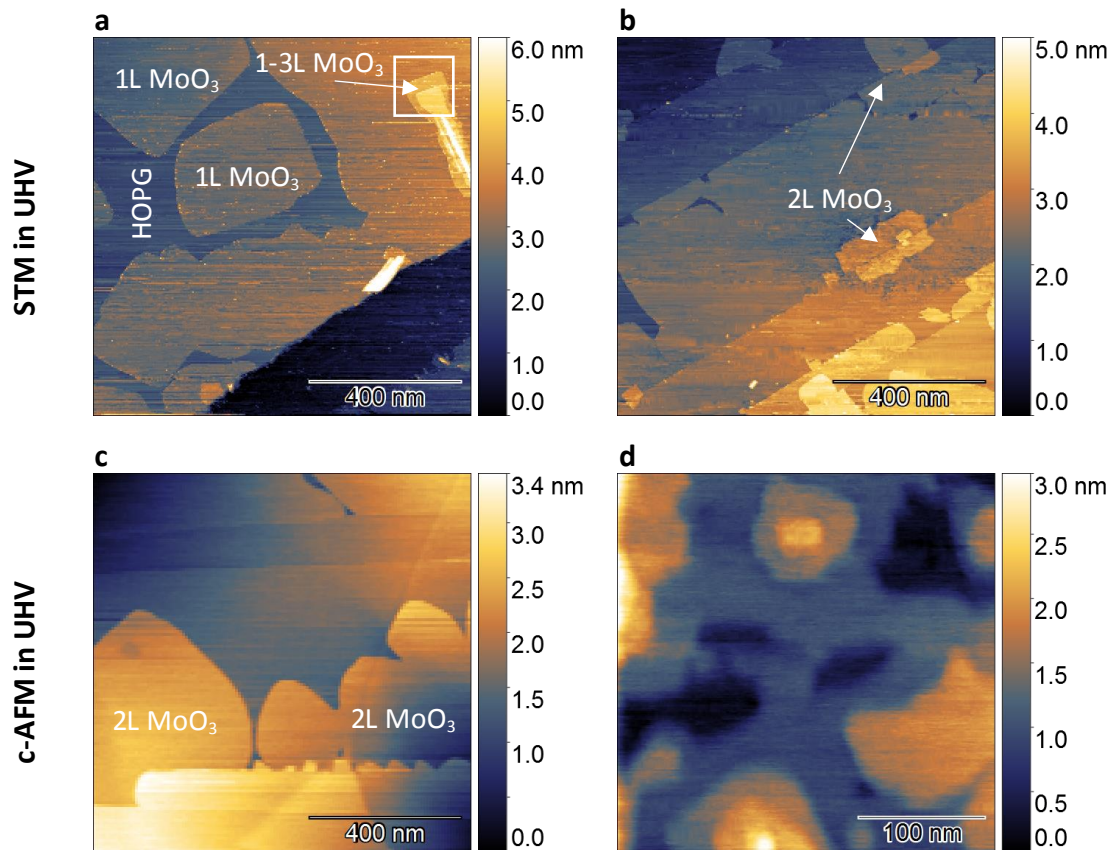


Figure 6: Typical morphology of monolayers of MoO₃ on HOPG. (a-b) large-scale STM images of typically shaped monolayer (1L) and bilayer (2L) MoO₃ nanosheets on terraces of the HOPG substrate ($V_{\text{tip}} = 0.6$ V, $I = 0.1$ nA, acquired in UHV). MoO₃ nanosheets are mostly monolayers and present the typical morphology of this material. **(c-d)** contact AFM (c-AFM) images of MoO₃ on HOPG acquired in UHV conditions, showing irregular 2L nanosheets and higher coverage, respectively. Note in (a), there is an indicated region of multiple stacked layers that is characterised in Figure 13.

We believe that the distinction between these morphologies results from a subtle balance between various factors such as speed of edge diffusion, interface energy promoting symmetry-enforced rectangular nanosheets, and local flux decrease in the vicinity of step edges or other adislands. To fully comprehend the growth mode, detailed calculations involving the energies of surfaces, interface, and edges of the HOPG/MoO₃ system are required [22,23]. All the aforementioned factors suggest:

- I. the mean free path of MoO_3 clusters, which directly impinge and diffuse on top of 1L MoO_3 is large, i.e. clusters that land on top can reach the film edge;
- II. Ehrlich-Schwöbel barrier for downward MoO_3 cluster diffusion is sufficiently small due to MoO_3 clusters overcoming it when arriving at the step edge of 1L films.

In consequence, the first MoO_3 layer initially grows in favour of the second layer.

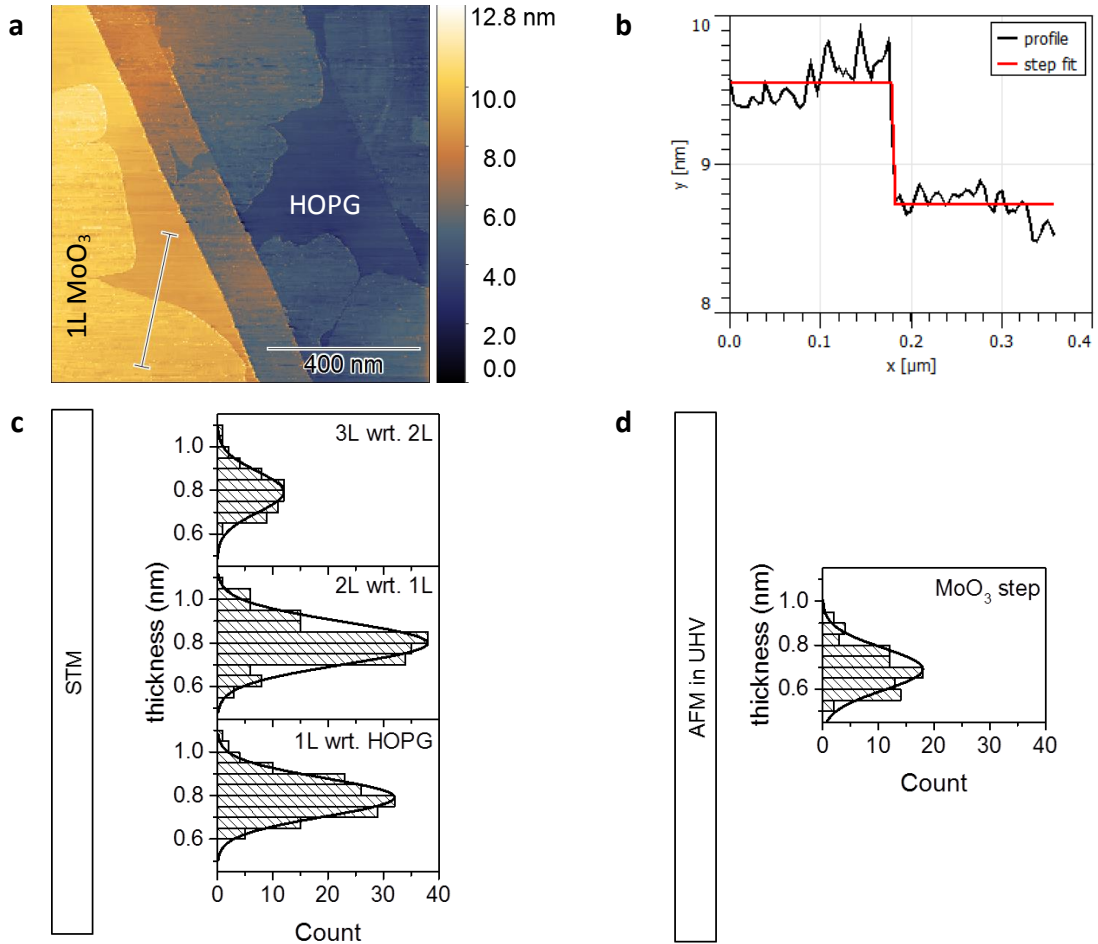


Figure 7: Statistical analysis of MoO_3 film thickness for the first three layers. (a) a representative large-scale STM image of typically shaped monolayer (1L) MoO_3 nanosheets (framed by dash lines) on HOPG terraces (framed by dotted lines) ($V_{\text{tip}} = 0.6 \text{ V}$, $I = 0.1 \text{ nA}$, acquired in UHV). (b) the lateral profile (averaged over 10 px) taken across the line marked in (a) reveals the 1L height of around $0.82 \pm 0.10 \text{ nm}$. (c) height distribution of individual layers measured on multiple MoO_3 nanosheets based on 54 STM images acquired in UHV with respect to (wrt.) a layer underneath. (d) height distribution of detected steps belonging to MoO_3 nanosheets based on 16 AFM images acquired in UHV conditions without differentiation between 1–3L.

To elaborate on thicknesses of MoO_3 layers, we performed multiple measurements of their heights using STM and c-AFM. Figure 7a presents a large-scale STM image of typically shaped 1L MoO_3 nanosheets on terraces of the HOPG substrate. Across the line marked in Figure

7a, we took a cross-section profile to show a representative measurement of the 1L MoO₃ height – it reveals a value of around 0.82 ± 0.10 nm (see Figure 7b with the profile and a step fit).

Figure 7c show statistical height distribution of individual layers of MoO₃ films measured by STM in UHV. The height measurements were acquired on multiple MoO₃ nanosheets based on 54 STM images with respect to a surface of a layer underneath, i.e. 1L to HOPG, 2L to 1L, and 3L to 2L. For details of acquiring statistical data, see Experimental Section 2.3. We statistically found the apparent thickness uniform for all first three layers. Mean values of heights based on STM measurements are presented below. The error intervals are the standard deviation.

- I. 1L MoO₃: 0.79 ± 0.09 nm
- II. 2L MoO₃: 0.80 ± 0.10 nm
- III. 3L MoO₃: 0.79 ± 0.10 nm

Because the given apparent height via STM is affected by the geometric and electronic structure and can substantially deviate from the actual height [112,113], especially at various applied biases (the majority of the measurement were acquired at similar parameters, i.e. $V_{\text{tip}} = 0.6$ V, $I = 0.1$ nA), we also evaluated the MoO₃ layer heights by AFM in contact mode. Figure 7d show statistical distributions of the step heights of MoO₃ films measured by c-AFM in UHV. Because of insufficient AFM data for discrimination of individual layers, we derive a mean value of step height for all three layers together: 0.69 ± 0.10 nm. While it is in agreement with STM measurements, AFM provides more accurate height measurements than STM. Our step height measurements are in line with previous reports, i.e. a minor step in α -MoO₃ crystal observed by AFM was 6.9 \AA [63].

In order to estimate epitaxial relation between MoO₃ monolayer and HOPG as well as surface lattice constants of grown MoO₃, we performed LEED measurement at room temperature at 55 eV. In Figure 8a, the LEED pattern from HOPG, covered mainly by MoO₃ monolayer, consists of rings. The presence of rings instead of sharp spots is observed because both structures comprise many crystallites having random in-plane orientations. Additionally, Figure 8b shows the same pattern with overlaid rings: the black outer ring correspond to first-order diffraction spots of graphite, while the white inner rings correspond to the rectangular MoO₃ structure and their first and higher order diffraction spots. Black and white dots were drawn to schematically illustrate where LEED spots would occur from single-domain graphite and α -MoO₃, respectively. For a clear explanation, the LEED pattern was simulated in LEEDpat software – see Figure 8c. The simulated pattern consists of spots of single-crystal graphite (marked by empty dots and connected by a blue ring, only first-order diffraction spots) and three distinguished domains of α -MoO₃ (marked by green, red, and purple dots and connected by white rings) with arbitrary alignment with respect to graphite. The two inner rings

correspond to first-order diffraction spots, while the outer one to second-order diffraction spots of MoO_3 .

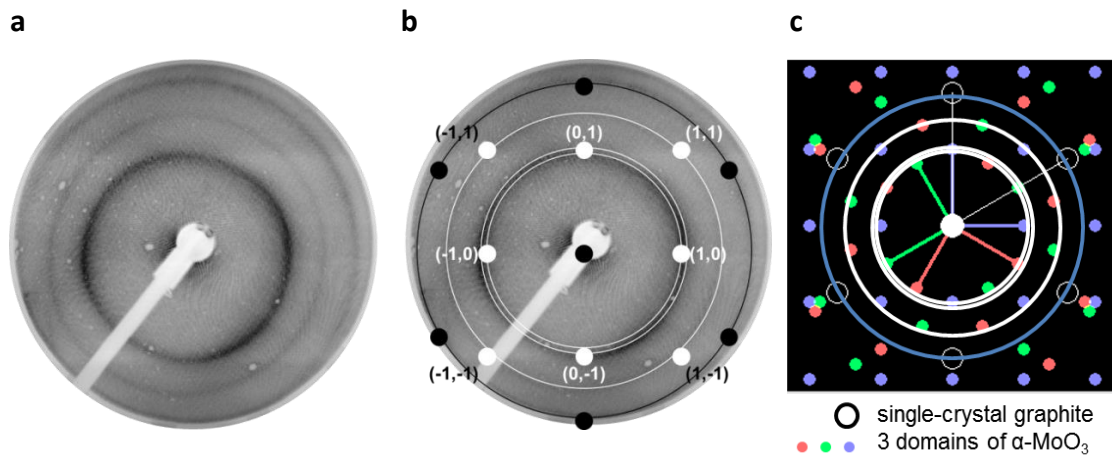


Figure 8: Crystal structure of monolayer $\alpha\text{-MoO}_3$ on HOPG. (a) LEED pattern from a monolayer film of $\alpha\text{-MoO}_3$ on HOPG at RT and $E = 55$ eV. **(b)** schematic of the diffraction rings drawn on top of (a). The inner (white) rings correspond to the rectangular lattice structure, and the outer (black) ring indicates the location of the HOPG first-order diffraction ring. Black dots indicate where LEED spots would occur from single-crystal graphite, while white dots illustrate possible locations of diffraction spots of a single-domain of $\alpha\text{-MoO}_3$ structure. **(c)** simulated LEED pattern of single-crystal graphite and multidomain (three distinguished domains) $\alpha\text{-MoO}_3$ with arbitrary alignment with respect to graphite.

The presence of many crystallites with random in-plane orientations is clearly seen for graphite, where the corresponding most outer ring (marked black in Figure 8b) has uniform intensity (see Figure 8a). In contrast, some intensity modulation can be seen in three inner rings corresponding to $\alpha\text{-MoO}_3$ (marked white in Figure 8b). It indicates that crystallites of grown MoO_3 monolayer have lateral dimensions larger than domains of underlying HOPG. In turn, this observation further supports the proposed above growth mechanism, in which directly impinged clusters diffuse toward $\alpha\text{-MoO}_3$ edges promoting the growth of monolayer. Nevertheless, due to too small lateral dimensions of domains of MoO_3 and HOPG, we cannot determine any particular epitaxial relation between them using LEED.

The surface lattice constants of $\alpha\text{-MoO}_3$ obtained from the diffraction rings are $(4.00 \pm 0.50) \times (4.23 \pm 0.50) \text{ \AA}^2$, using the graphite diffraction ring as a reference. Unfortunately, the experimental error is high due to the proximity of the inner rings leading to the unclear measurement of their diameters. The given surface lattice constants are slightly bigger but within the error range agree with known $\text{MoO}_3(010)$ [39,46,63].

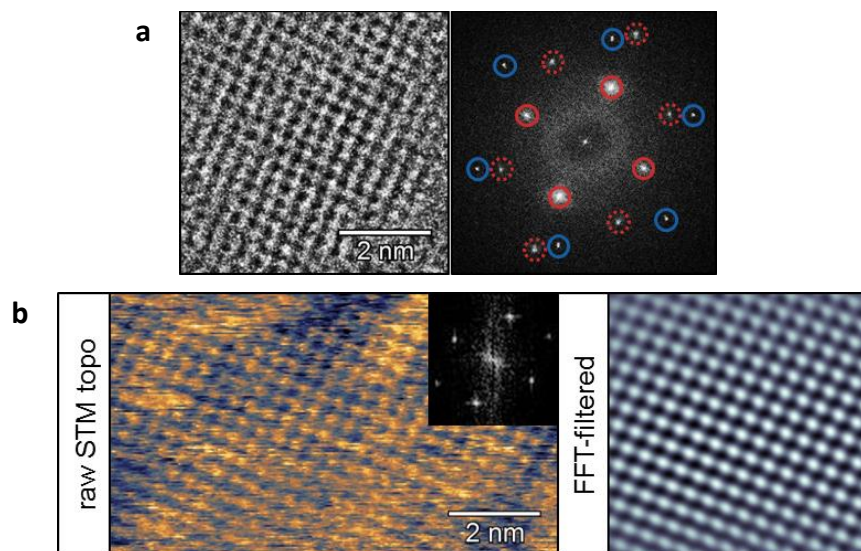


Figure 9: Atomic structure of MoO₃ monolayer on HOPG. (a) HR-TEM image (right) and typical FFT pattern (left) of single-domain MoO₃ nanosheet. Red solid and dashed circles indicate first and higher-order diffraction spots of α -MoO₃, respectively (see Figure 8 for a full description of particular spots), while blue circles indicate first-order diffraction spots of HOPG lattice. **(b)** highly resolved raw STM image (left) recorded at 1L MoO₃ ($V_{\text{tip}} = 0.2$ V, $I = 0.9$ nA, acquired in UHV) together with FFT pattern (inset) and the corresponding filtered image (right panel).

To further confirm and expand information on crystal structure, we continued with high-resolution TEM (HR-TEM) and STM analysis. Samples suitable for TEM measurements were peeled off from the top surface of the bulk HOPG in the form of multilayer graphene flakes with MoO₃ on top. Figure 9a shows an atomically resolved HR-TEM image (left panel) revealing a uniform MoO₃ layer formed at HOPG. Together with a typical fast Fourier transform (FFT) pattern (Figure 9a, right panel), HR-TEM data suggests orthorhombic unit cell of α -MoO₃. The calculations based on inner diffraction spots, marked with solid red rings, provide the dimensions of the surface unit cell equal to $-(3.66 \pm 0.20) \times (3.88 \pm 0.10) \text{ \AA}^2$, which is in agreement with literature data for α -MoO₃ [39,46,63]. The spots marked with red dashed rings come from higher-order diffraction spots of α -MoO₃. The outer spots in the FFT, marked blue, are identified as the hexagonal reciprocal lattice of graphene/graphite.

It would be interesting to analyse the lattice overlays configuration of HOPG/MoO₃. In multiple HR-TEM images, we observed that MoO₃ forms domains, which tend to be rotated by 15° (or 105°) and 30°(or 120°) with respect to each other. However, the inspection of the alignment angle between MoO₃ and HOPG lattices revealed various angles in quantitative analysis of FFT of HR-TEM images. Unfortunately, we find our analysis inconclusive and wish to expand this study. In contrast to previous reports (on substrates such as graphite, hBN, MoSe₂ and mica [44,70]) where 2L MoO₃ sheets grow with restricted facet orientation of 60° with

respect to each other, HOPG seem to allow growth of 1L MoO₃ domains in several azimuthal alignments. In particular, Kim *et al.* [70] presented graphene(multilayer)/MoO₃ crystalline orientation relation, where the MoO₃ aligns along the main symmetry axes of graphene. We have not observed such a configuration. It may indicate that, for the case of UHV epitaxy, the HOPG (and presumably also graphene) substrate does not influence the orientation of grown monolayer MoO₃ films.

The orthorhombic structure of 1L MoO₃ is further confirmed by an STM image with atomic resolution acquired on the 1L terrace (Figure 9b, left panel), which shows a nearly square unit cell (see the corresponding FFT pattern in the inset). It should be noted, that at room-temperature the thermal drift affects the precise determination of a unit cell dimensions. However, our statistical analysis from STM images yields the dimensions of surface unit cell of $(3.85 \pm 0.66) \times (4.41 \pm 0.77) \text{ \AA}^2$, which agrees with the LEED and HR-TEM results.

3.2.2. Chemical and Electronic Structure: XPS and UPS Characterisation

3.2.2.1. XPS Characterisation

First, we describe XPS results to estimate stoichiometry of 1L MoO₃ film. The XPS measurements were recorded at 60° grazing electron exit angle with respect to the surface normal in order to increase the surface sensitivity. Figure 10a shows an XPS spectrum for the Mo3d core-level region. For details of the fitting curve parameters, see Experimental Section 2.3. The spectrum

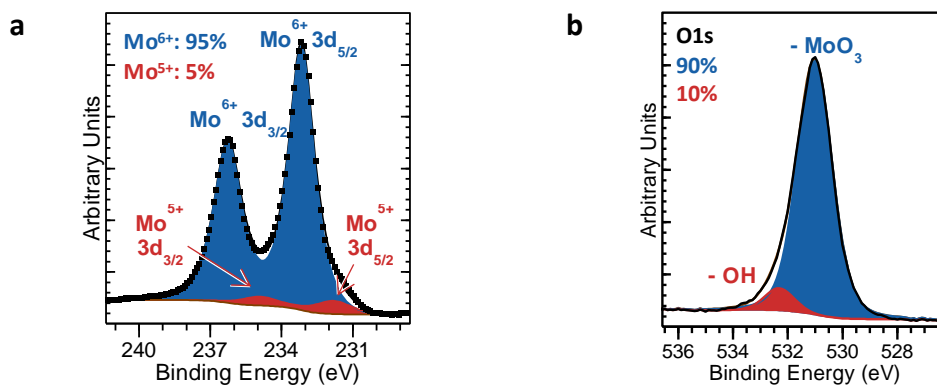


Figure 10: Chemical composition of MoO₃ monolayer on HOPG: XPS measured at exit angle of 60° to the surface normal. (a) Mo3d XPS spectrum; experimental data (points) and fitting with a two-component profiles corresponding to Mo⁶⁺ (blue) and Mo⁵⁺ (red) in approx. 95:5 ratio. (b) O1s XPS spectrum; experimental data (black line) with fitting. Two components correspond to lattice oxygen of MoO₃ (blue) and hydroxyl groups (red).

was fitted with two double components that correspond to approx. 95% of Mo⁶⁺ (3d_{5/2} at binding energy (BE) of 233.2 eV) and 5% of Mo⁵⁺ (3d_{5/2} at BE of 231.8 eV) [19,43,65,69,71,79]. Although

the Mo3d region shows no indication of further splitting or broadening beyond Mo⁵⁺ within our experimental resolution, we cannot fully exclude the presence of Mo⁴⁺ (3d_{5/2} typically observed at 229.4 eV [41,43,65,71,79]). We tentatively refer to the 1L molybdate structure as nearly stoichiometric MoO_{3-x}, where x = 0.03 ± 0.01, based on the areas of the Mo⁶⁺ and Mo⁵⁺ peaks.

In addition, the O1s region is shown in the XPS spectrum in Figure 10b. Typically in TMOs, the O1s peak is asymmetrical towards higher BE. The O1s peak at BE of 531.0 eV is attributed to the metal oxide component, i.e. the lattice oxygen of MoO₃, along with a shoulder peak at BE of about 532.3 eV, which can be associated with hydroxyl groups (-OH) on the surface [40,130]. On the contrary, this shoulder peak has been previously assigned to the oxygen in distorted environment due to defect (vacancy) sites [65,127]. However, we discount this assignment. Nonetheless, we treat apparent Mo reduction as a quality rather than a quantitative indicator because the likely substoichiometric level of (3 - x) is around 2.97. As already stated, in this thesis, we refer to nearly stoichiometric MoO₃ without indicating a slight reduction in the index. Previously, it has been shown that thermally evaporated MoO₃, like other TMOs, was oxygen-deficient resulting in a typical substoichiometric level (3 - x) ≥ 2.5 [43,131].

The oxygen deficiency level depends on the substrate's choice and growth conditions, such as the source's temperature and the substrate during deposition [6,38]. We kept the HOPG substrate at the temperature of 220 °C during evaporation. Following previous reports, it should result in non-negligible oxygen loss as annealing above 200 °C leads to the presence of Mo⁶⁺, Mo⁵⁺, and some Mo⁴⁺ [65,69].

On the other hand, the lower oxidation states of Mo may appear due to charge transfer with the substrate induced by chemical potential difference at the interface [6,19,37,38,43]. MoO₃ is known to induce p-type doping in carbon substrates leading to downshifting in the BE of the C1s peak by 0.3–0.7 eV [6,19,37,41,132]. Such conclusions are beyond the experimental resolution capabilities in our system.

Interestingly, Greiner *et al.* [38] reported that a MoO₃ film was indeed reduced at the contact with metal, so within the first few nanometres. Moreover, it is known that the MoO₃ electronic structure exhibits thickness dependence on graphene substrates; graphene induces a significant amount of Mo⁵⁺ formation at the graphene/MoO₃ interface [6,19]. However, those reports did not focus on the crystalline α phase of MoO₃. In the next Section 3.2.3, we discuss that reported conclusion by comparing 1L–3L MoO₃ and their electronic structures. Also, Du *et al.* [72] suggested that charge transfer between MoO₃ monolayer (approx. 9% of Mo⁵⁺) and the SrTiO₃ substrate was responsible for the stabilisation of the MoO₃ film. Similarly, Quek *et al.* [22] associated the charge redistribution at the Au/MoO₃ interface with the stabilisation of the monolayer structures.

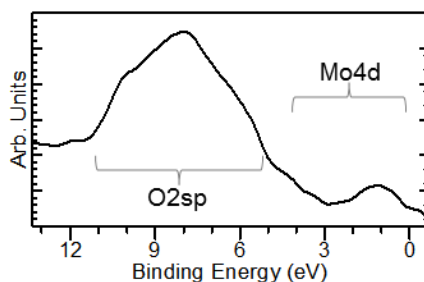


Figure 11: Valence band region of MoO₃ monolayer on HOPG: XPS measured at exit angle of 60° to the surface normal. The intensity is dominated by O2sp contributions and some of Mo4d at lower BE. The valence band edge is at BE of about 2 eV.

Both scenarios of the thermal reduction during growth and the charge transfer between the MoO₃ monolayer and the substrate are possible. Thus, we do not exclude each other but conclude that some amount of reduced MoO₃ species is present, which further can be associated with a considerable number of states within the bandgap – described in the following Sections. In general, α -MoO₃ has valence and conduction bands approx. 3.0 eV apart, and while slightly reduced has additional bands below conduction band minimum, leading to decrease of the bandgap [42,46,64,65] – see also Section 3.2.5. Here, we present the XPS valence region in Figure 11. The overall intensity of the spectrum is dominated by O2sp contributions, with some intensity between 0.0 and 3.0 eV corresponding to Mo4d [42,65]. The intensity in that range indicates the presence of oxygen vacancies [79].

3.2.2.2. UPS Characterisation of Valence Band Region

In this Section, we continue the investigation of the valence band region, but with a better resolution by utilising He I (21.22 eV) UPS.

Figure 12 presents UPS spectra recorded in the valence band region of HOPG/1L MoO₃ (blue spectrum). Note that in this case, the UPS data consists of spectral contributions from both MoO₃ and the HOPG substrate – we estimate the coverage by 1L MoO₃ film to be roughly 70%. Firstly, we measure an average bandgap width. The typical approach neglects the low emission at lower energies due to the gap states close to 0 eV. The average bandgap considers the dominant signal in a UPS spectrum. Therefore, the valence band edge is estimated (dash line) at 3.1 ± 0.1 eV, which agrees with [19]. However, the bandgap may be wider based on previously published IPES measurements that placed the edge of the conduction band at 0.2 eV (take the opposite sign when comparing with our binding energy scale) [42,128]. Thus, we can assume the width of the bandgap even up to 3.3 eV, agreeing with the width for bulk MoO₃ [46].

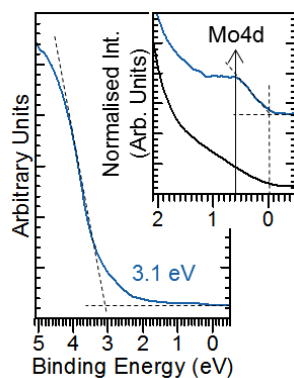


Figure 12: Valence band region of MoO₃ monolayer on HOPG: He I UPS spectra. Inset: magnification of gap states region; pristine HOPG (black) and HOPG/MoO₃ (blue). Dashed lines mark valence band edge and gap state edge (inset).

On the other hand, XPS measurements proved that the presence of states within the bandgap is non-negligible, detecting some occupied Mo4d states (Section 3.2.2.1). Also here, we are interested in that low-intensity contribution close to 0 eV. In the inset of Figure 12, next to the blue spectrum of HOPG/1L MoO₃, we added a black spectrum of bare HOPG to serve as a reference to track the differences in the electronic structures.

When comparing the two spectra, we can recognise an additional broad peak (see an arrow marking the build-up intensity) in the range of 0.0–1.2 eV for the sample with MoO₃ in contrast to bare HOPG, which agrees with a feature observed for graphene/MoO₃ [6,19]. The gap state edge is estimated to fall to 0.0 eV (see dash lines). The emission from Mo4d occupied states further confirms the XPS conclusions and indicates that some reduced MoO₃ is present at the interface with HOPG.

Because UPS does not resolve distinct peaks at the region of interest, our conclusion of a small but detectable number of reduced Mo species can be further investigated on the nanoscale.

3.2.3. Local electronic structure of MoO₃ from monolayer to trilayer: STM/STS characterisation

Theory calculations predict that the electronic structure of α -MoO₃ is nearly independent of the number of layers [44–48] – see also Section 3.2.5. Previous experimental studies by PES, have not provided insights into the MoO₃ electronic structure depending on the number of layers, primarily due to amorphous structures and lack of investigations on the nanoscale.

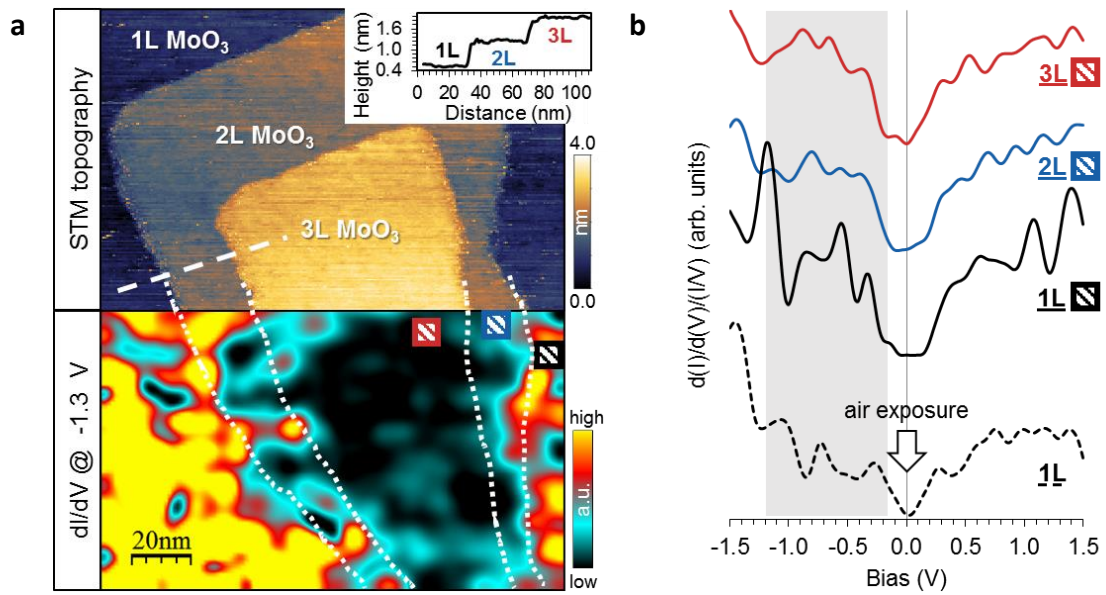


Figure 13: LDOS varying with a number of MoO₃ layers (1–3 L) on HOPG: STM and STS. (a) STM topography (top panel) with overlaid LDOS map (bottom panel) of MoO₃ nanosheet of monolayer (1L), bilayer (2L) and trilayer thickness (3L) ($V_{\text{tip}} = 1.5 \text{ V}$, $I = 100 \text{ pA}$; LDOS displayed at -1.3 V). The broader topography of (a) is shown in Figure 6a. The scale of LDOS map ranges from black (corresponding to the low value of LDOS) to yellow (corresponding to high LDOS). The inset's lateral profile taken from the dashed line across the topography. **(b)** dI/dV curves recorded and averaged from square regions marked on the LDOS map for 1L (black), 2L (blue) and 3L (red). Additionally, a dI/dV curve for 1L (dashed line) was taken after air exposure. For easy comparison, another spectrum was plotted (bottom spectrum, dashed curve) – air exposure effect is described in the following Section 3.2.4).

To determine the dependence of MoO₃ electronic properties on thickness, local STS measurements were performed on the first three layers. Figure 13a shows an STM topography in the top panel with overlaid LDOS map in the bottom panel. The STM topography shows three stacked MoO₃ nanosheets with one-, two-, and three-layer (1–3L) thickness, while the broader topography can be seen in Figure 6a, revealing the underlying HOPG surface. The edges of those layers are marked by dotted lines based on the topography information. Additionally, the lateral profile (inset in Figure 13a) taken across the STM topography (see dashed line) reveals a height of approx. 0.68 nm for each of the MoO₃ layers. In correlation with the topography, the bottom panel presents spatially resolved STS data that measures local density of states (LDOS) in function of bias voltage (energy). dI/dV quantity is plotted in the LDOS map plots at the bias voltage of -1.3 V . The map shows clear contrast in LDOS between 1L and subsequent layers. Note that black colour corresponds to low values of LDOS, while yellow colour corresponds to high values of LDOS. The electronic structure of 1L MoO₃ is distinguishable from the subsequent layers.

The STS spectra of the respective layers reveal a decrease in the density of states in the valence bands with an increase in thickness, resulting in the vivid contrast on the LDOS map. A closer inspection of the STS map shows maximum LDOS values for 1L MoO₃ at energies < -1 eV. This maximum is characteristic for the whole area of 1L – presented as high intensity (yellow colour) in LDOS map at -1.3eV – which does not occur for 2L and 3L. In comparison, the transition from 2L to 3L MoO₃ presents only a subtle difference. The dependence on the number of layers (the thinner MoO₃ film, the higher LDOS at energies < -1 eV) suggests more reduced MoO₃ species at the interface with the HOPG substrate. Such interpretation agrees with the aforementioned trend (see Section 3.2.2) of higher MoO₃ reduction at the interface and lower with increasing thickness. If the electronic structure of the α -phase MoO₃ is thickness-independent, as the theory suggests, we can associate the observed differences between the first three layers with the reduction of Mo. Assuming that the reduction is due to charge transfer at the interface with the substrate, this may also explain the stability of 1L MoO₃ on HOPG [72].

Figure 13b shows the STS spectra (as normalised differential conductance) recorded on the first three layers of MoO₃, which were obtained by averaging and differentiating approx. 50 I(V) curves from each area marked on the LDOS map (bottom of Figure 13a). The typical spectra from 1–3 L reveal a semiconducting character, where the bandgap is narrow and roughly equal to 0.4 eV for all thicknesses. The narrow bandgap can be explained by the defect states observed in XPS and UPS measurements.

We can distinguish a few characteristic features from the STM results for all three MoO₃ thicknesses – see the valence bands highlighted by a grey rectangle in Figure 13b. The features, when grouped, form an apparent increase (local maximum) of the LDOS, which is centred at roughly -0.7 eV and spans from -1.2 to -0.2 eV. It agrees with the UPS (Figure 12), which provides information over a wider sample area. In particular, when we average STS from a wider area, LDOS becomes featureless, with only one broad peak having a plateau from -0.6 eV towards higher energies, which resembles the UPS spectrum (Figure 12). We attribute the distinct features to defects representing possible nonstoichiometric Mo-O configurations, in line with the previous reports on PES studies. However, our observations of local changes in the MoO₃ electronic structure suggest that they are heterogeneous. The local variations imply that the electronic structure of MoO₃ cannot be simply learnt from averaged data measured over a large scale – note variance of differential conductance at 1L and energies < -1 eV in the LDOS map in Figure 13a). The defects must be randomly distributed and localised, presumably down to a few atoms, because they are undetected in HR-TEM observations, displaying long-range ordered structures. On the other hand, the lack of any periodicity excludes other phases exhibiting uniformly distributed crystallographic shear planes. Moreover, routinely acquired STM atomic

resolution and HR-TEM results indicate no considerable lattice deviation. It implies a substantial disorder of undefined type coexisting with the ordered structure. We propose that the possible aggregation of defects affects the local properties as it is typical of other TMOs [133,134]. Nevertheless, the heterogeneity of MoO species observed for 1L MoO₃ at the interface with HOPG remains unclear.

3.2.4. Air Exposure Effect on Monolayer MoO₃: STS and UPS Characterisation

In the previous sections, we presented *in-situ* investigations in UHV, which describe the properties of as-synthesised material. This Section investigates 1L MoO₃ films after exposure to ambient conditions and assesses the possibly introduced changes. It has been reported that the bulk MoO₃ electronic structure changes upon exposure to oxygen and air [42,43]. We extend the available data by examining the air exposure effect on crystalline 1L MoO₃.

After exposure to air for a few days, we reintroduced the HOPG/1L MoO₃ sample back to UHV. Note that the sample has not been cleaned, and the STM measurements are easily performed on 1L MoO₃. We did not aim to remove air-induced adsorbates from the surface as even gentle sputtering is known to induce defects [39], while annealing reduces MoO₃ [65,69].

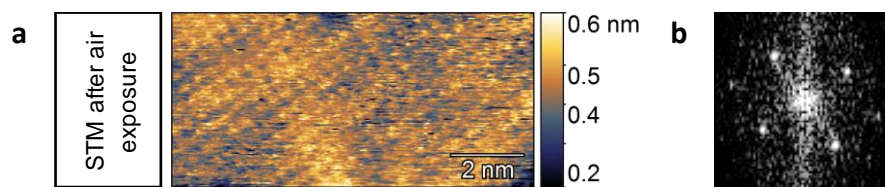


Figure 14: Atomic structure of MoO₃ monolayer on HOPG after air exposure: STM. (a) highly resolved STM image recorded at 1L MoO₃ ($V_{\text{tip}} = 0.2$ V, $I = 0.9$ nA). **(b)** the corresponding FFT pattern.

We present the atomic resolution STM image taken on a sample which was exposed to air – see Figure 14a. The crystal structure of 1L MoO₃ is unaffected upon exposure to air. This indicates high stability of 1L MoO₃ films on HOPG. The corresponding FFT pattern (Figure 14b) suggests a nearly rectangular unit cell of $(4.20 \pm 0.40) \times (4.40 \pm 0.70)$ Å² (room-temperature drift affects the precise determination).

Here, we refer once more to the STS results in Figure 13b (page 49), presenting the dI/dV curve recorded at 1L MoO₃ exposed to air (see the bottom spectrum, dashed line). The plot shows that the apparent bandgap narrows compared to the unexposed 1L MoO₃/HOPG (see solid black line). In contrast, regardless of air exposure, the differential conductance maintains the asymmetry of higher values for bias < -1 V. We suggest that the mechanism of narrowing

the bandgap after air exposure is related to hydrogenation or hydroxylation of MoO₃. Li *et al* [48] claimed that for MoO₃ monolayer, hydrogenation results in the formation of conduction bands. Also, adsorption of water and hydroxide groups might lead to the vanishing of the bandgap in MoO₃ [135]. Further research is necessary to fully understand the processes underlying the bandgap closure due to air exposure of MoO₃.

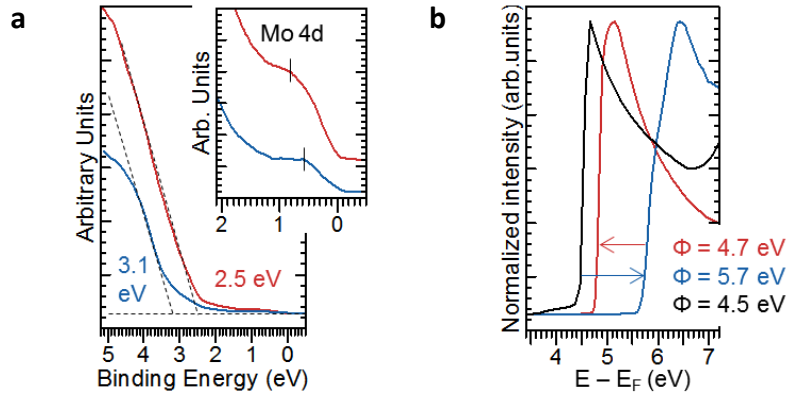


Figure 15: Electronic properties of MoO₃ monolayer on HOPG: He I UPS. Bare HOPG spectrum serves as a reference (black) and HOPG/MoO₃ spectra were taken before (blue) and after air exposure (red). **(a)** valence band region. Dashed lines extrapolate valence band edges. The inset magnifies region of low BE, where maxima of gap states are marked. **(b)** secondary electron cut-off (SEC) region. The photoelectron energy is calibrated to Au Fermi level ($E - E_f$), the energy indicated by SEC corresponds to work function. The arrows indicate that work function increases after MoO₃ deposition (blue) and decrease after air exposure (red).

To further confirm the narrowing of the bandgap at a larger scale, we also study the air exposure effect by UPS. Figure 15a presents UPS spectra of HOPG/1L-MoO₃ before (blue; see also Figure 12) and after air exposure (red). The intensity in the range of 5.0–2.5 eV is higher after air exposure, which agrees with [38,39]. The valence band edge related to O2sp states can be found at 2.5 ± 0.1 eV for the exposed sample, which is upshifted by 0.6 eV with respect to the original unexposed sample. Additionally, the inset in Figure 15a, magnifying the region of low BE, shows a higher intensity for the exposed sample than the unexposed sample (see that marked maxima of gap state contribution also shift). This observation agrees with Irfan *et al* [43] regarding the higher intensity of detectable gap states when MoO₃ was exposed to ambient. It can be explained, based on the previously referenced PES results, as a partial reduction of Mo species contributes to the higher gap states intensity at BE of around 0.9 eV. However, we cannot entirely exclude the possible role of a charge transfer from the adsorbates from air [43].

Finally, we start discussing the air exposure effect on the 1L MoO₃ work function. The secondary electron cut-off (SEC) region of UPS spectra is shown in Figure 15b. The black spectrum corresponds to bare HOPG, which SEC denotes the expected work function of

4.50 ± 0.10 eV (in agreement with literature values: 4.40–4.60 eV [136,137]). The blue spectrum corresponds to HOPG/1L-MoO₃, where the 1L MoO₃ nanosheets cover HOPG at around 70%.

The SEC of blue spectrum is found at 5.7 ± 0.1 eV, which is related to increase in the initial WF of the substrate (marked by a blue arrow). Next, the red spectrum corresponds to the HOPG/1L-MoO₃ that was exposed to air. Upon air exposure, SEC downshifts by around 1.0 eV (marked by a red arrow), to 4.7 ± 0.1 eV indicating reduction of the work function of this system.

Due to low coverage by 1L MoO₃ and uncovered regions of HOPG, the SEC value does not indicate the WF of MoO₃ nanosheets, but resultant SEC for two-component surface of HOPG and MoO₃. Detailed SEC interpretation for such systems is given in Section 2.4 and a separate Chapter 5. However, the UPS results present clear trend of increasing heterostructure WF with deposition of MoO₃ and further reduction upon air exposure, which agrees with previous results for thicker films [6,19]. The reduction is in line with the well-known effect of air, where the WF of bulk MoO₃ reduced from 6.9 eV to 5.2 eV [42,43].

3.2.5. Theoretical characterisation

To support the discussion of experimental results, we performed DFT calculations. The results allow for addressing the dependence between the number of layers in MoO₃ system and the unit cell parameters including the estimation of monolayers thicknesses. Additionally, the influence of the number of layers and the presence of oxygen defects on the electronic structure was calculated. Drawings of crystal lattices were produced using VESTA [124]; note that VESTA default parameters govern the presence or absence of chemical bonding.

3.2.5.1. Crystal structure: Lattice Parameters Estimation

Firstly, we describe DFT calculations predicting in- and out-of-plane dimensions of α -MoO₃ layers. Figure 16a shows separately: 1L α -MoO₃ with a marked height (measured between terminal O atoms); and two layers of α -MoO₃ (2L) with marked height of one layer and 1L together with interlayer spacing. The predicted distance between terminal O atoms for 1L α -MoO₃ equals 6.40 Å. The calculated interlayer spacing between layers (equal to 7.34 Å) are essentially in line with experiments where the interlayer spacing between MoO₃ and HOPG is taken into account.

The measured lattice parameters for 1L and 2L (marked in Figure 16a) are plotted in Figure 16b together with data for 3L, 4L and bulk – the height of single MoO₃ layer slightly varies with an increasing number of layers. Note that the y-axis presents lattice parameter b , which is

the distance between terminal O atoms, so it should not be confused with unit cell size in the standard sense used for bulk α -MoO₃.

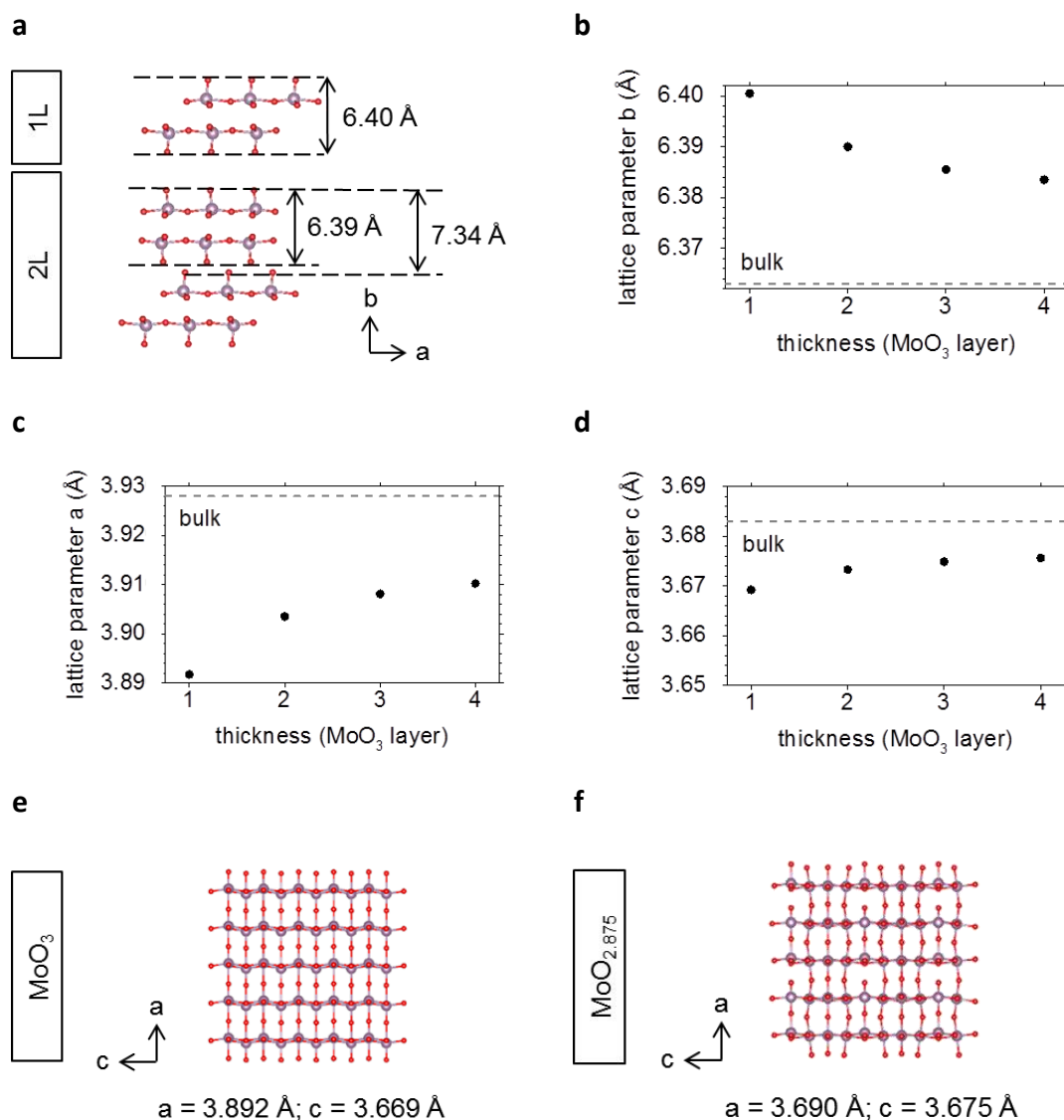


Figure 16: DFT calculations. (a) scheme: the dimensions of a 1L α -MoO₃ are marked as distance between terminal O atoms and with interlayer spacing at 2L. **(b-d)** graphs: lattice constants of α -MoO₃ in the function of a number of layers with bulk values for reference (lattice constant b is given as distance between O terminal atoms). **(e-f)** top views of the atomic structures of 1L α -MoO₃ and 1L MoO_{2.875}; lattice constants are given.

Additionally, DFT calculations provide unit cell parameters: a and c for 1–4L α -MoO₃, plotted in Figure 16c and d, respectively, with bulk values for reference. The a and c lattice constants in the function of the number of layers exhibit subtle differences among the layers, which are immeasurable experimentally. With an increase in the number of layers, one can predict elongation in both a and c unit cell constants accompanied by a decrease in b (see Figure 16b). Our DFT calculations of 1L α -MoO₃ predict a rectangular surface unit cell (3.96×3.70) Å²,

which is in agreement with the literature [45,47] and experimental values (see Section 3.2.1). In Figure 16e, we also illustrate the top view structure of stoichiometric MoO_3 with those lattice constants (2×2 supercell projection on 1×1 cell).

To complement the preceding Sections, we highlight how oxygen vacancies may affect different cell parameters. We chose as an example $1\text{L MoO}_{2.875}$ – the top view of the atomic structure is shown in Figure 16f with given lattice parameters. It indicates a change of unit cell constants after embedding the oxygen vacancy, which was apical on a MoO_3 surface to a 2×2 supercell. It results in an expanded unit cell compared to the stoichiometric MoO_3 . For an extensive discussion of oxygen vacancies affecting MoO_3 crystal structure, see [138,139].

3.2.5.2. *Density of States: Oxygen defects and Thickness dependence*

To simulate the influence of oxygen vacancies on the $1\text{L } \alpha\text{-MoO}_3$ electronic structure, we calculated the density of states (DOS) for stoichiometric $1\text{L } \alpha\text{-MoO}_3$ and reduced $1\text{L MoO}_{2.875}$. In Figure 17a, we compare the calculated DOS for $1\text{L } \alpha\text{-MoO}_3$ (black) with $1\text{L MoO}_{2.875}$ (blue). The calculations indicate that the bandgap for $1\text{L } \alpha\text{-MoO}_3$ is 1.8 eV. Such underestimation (related to the experimental results near 3.2 eV) is known in DFT and depends on pseudopotential selection [45,46]. Our selection of pseudopotential aimed primarily at analysing the lattice parameters (Figure 16) and not the reproduction of the bandgap. For $1\text{L of MoO}_{2.875}$, oxygen loss induces states within the bandgap of the stoichiometric $\alpha\text{-MoO}_3$ structure. Consequently, unlike stoichiometric $\alpha\text{-MoO}_3$, $1\text{L of MoO}_{2.875}$ becomes conducting.

To recognise the contribution of particular elements, Figure 17b plots the DOS for $1\text{L MoO}_{2.875}$ projected on oxygen and molybdenum atoms in red and blue, respectively, while the total DOS is in black. The majority of the contribution to DOS around 0 eV is related to Mo (mostly to d states).

Finally, to check DOS dependence on a number of layers $\alpha\text{-MoO}_3$, Figure 17c shows calculated DOS for 1L , 2L , and $3\text{L } \alpha\text{-MoO}_3$ (in black, blue, and red) as well as bulk $\alpha\text{-MoO}_3$ (dashed line). All characteristics are nearly uniform. The bandgap width for bulk is the widest and equal to 1.8 eV; for 1L – 3L the bandgap is slightly narrower. However, the difference is neglectable.

Qualitatively, our findings suggest that oxygen vacancies generate additional states between -1 and 0 eV. Such a conclusion is consistent with our experimental result of the narrow bandgap and the presence of states around 0 eV. Thus, the $\alpha\text{-MoO}_3$ electronic structure is not determined by the number of layers (within the first three layers) but rather by the concentration and arrangement of defects as well as the possible electronic interaction at the HOPG/ MoO_3 interface.

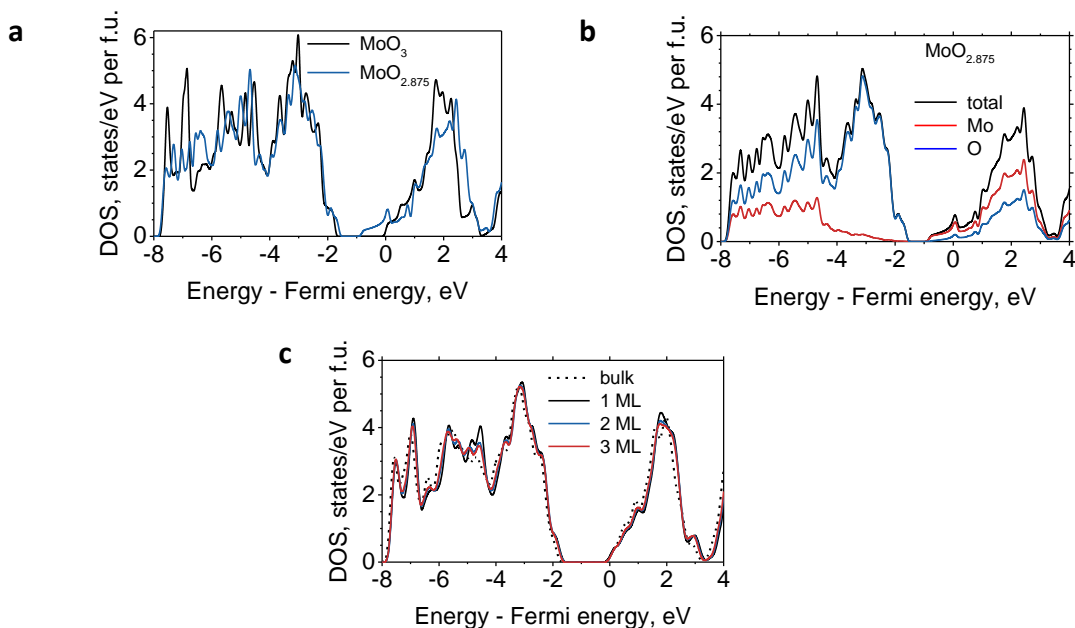


Figure 17: DFT calculations: density of states. (a) DOS of 1L α - MoO_3 (black) and 1L $\text{MoO}_{2.875}$ (blue); **(b)** DOS of 1L $\text{MoO}_{2.875}$ (total, black) projected on molybdenum (blue) and oxygen (red) atoms. **(c)** DOS of 1L (black), 2L (blue), 3L (red) and bulk (dashed) α - MoO_3 .

3.3. Conclusions

It was proved that it is possible to synthesise the monolayers of MoO_3 on HOPG and the electronic structure of such layers was investigated by various methods. To sum up, we answer to questions asked at the beginning of the Chapter.

1. Thermal evaporation under UHV directly on HOPG resulted in crystalline MoO_3 with monolayer thickness, proving our method was successful. The morphology and crystal structure investigations are summed up in the following list:
 - The grown 1L MoO_3 were stable and allowed detailed nanoscale characterisation by SPM.
 - We determined two shapes of MoO_3 nanosheets growing on HOPG by STM and c-AFM: irregular with curved edges (mostly for 1L) and rectangular (mostly for 2L).
 - We discussed MoO_3 nucleation, which starts at defects and the steps or domain edges of the HOPG substrate. MoO_3 tends to build up monolayers to cover the substrate before forming successive layers. The diffusion of MoO_3 clusters on the HOPG surface is sufficiently high to favour monolayer growth over successive layers.

- By STM and c-AFM, we determined 1L MoO₃ thickness as 0.7 ± 0.1 nm, which agrees with half of the height of single unit cell of α -phase MoO₃ corresponding to the basic vdW building block of the α -MoO₃ layer structure.
 - We measured surface lattice constants for MoO₃ by LEED, HR-TEM, and STM, proving the crystallinity of monolayers. The results agreed with the orthorhombic unit cell of α -phase MoO₃ [70] with dimensions: $(3.66 \pm 0.20) \times (3.88 \pm 0.10)$ Å².
2. Such a deposition method led to slightly reduced 1L MoO₃, consequently, to defect states in the bandgap.
 - We determined oxidation states of Mo ions in the films by XPS, showing the presence of 95% of Mo⁶⁺ and 5% of Mo⁵⁺, leading to the substoichiometric level of around 2.97, i.e. MoO_{2.97}.
 - Due to reduced MoO₃ species, we observed the gap states at low binding energies 0.0–1.2 eV by XPS and UPS. We discussed their origin from Mo4d filled states. We discussed a wide bandgap of 3.1 ± 0.1 eV in common approach from UPS.
 3. The nanoscale study of the electronic structure by STS, revealed that the first layer is distinguished from two subsequent layers.
 - The heterogeneity of the local electronic structure of the first layer is due to either oxygen vacancies or interface-induced defects.
 - The narrow apparent energy gap is similar for the first three layers of MoO₃ on HOPG and measures 0.4 eV.
 4. The air exposure affected 1L MoO₃: the apparent bandgap closed, and work function reduced.
 - A notable decrease in work function to 4.7 eV accompanied the higher emission intensity gap states, which was measured by UPS.
 - It was possible to characterize the air exposure material by STM without any cleaning procedure and the results proved the preservation of 1L MoO₃ crystallinity.
 - The local changes in the 1L-MoO₃ electronic structure further decreased the bandgap width, which was confirmed by STS.

In addition, DFT calculations predicted lattice parameters and found little differences between one to four layers of MoO₃: rectangular unit cell (3.96×3.70) Å² and thickness of 0.73 nm (when adding interlayer spacing). The calculations also shed light on the possible cause

of experimentally observed decrease of the bandgap, indicating that the concentration and distribution of oxygen defects in MoO₃ monolayers may significantly narrow the bandgap.

4. Towards Graphene/2D MoO₃ Heterostructures: Translating the Growth of α -MoO₃ from Graphite to Graphene

Many studies have focused on the growth parameters and post-deposition processing to find routes to improve MoO₃ film properties; however, the effect of the underlying substrate has not yet been carefully explored and could hold an essential key to the improvement of the quality of MoO₃ films, particularly those grown in UHV. Substrate selection influences the growth models, including TMOs and MoO₃. Epitaxial growth of MoO₃ monolayers on HOPG has been demonstrated in Chapter 3. Using a HOPG surface as a model of a graphene-like system, our studies highlight that careful substrate preparation is a crucial factor for promoting lateral growth of 2D MoO₃.

The aim here is to allow lateral growth of 2D MoO₃ films on graphene and this way to synthesise a new 2D heterostructure layer. The ability to grow 2D structures in a controllable fashion may open exciting possibilities for practical applications. One could expect no difference between graphene and HOPG, as the top layer structure and vdW interaction during growth should be similar. However, a reliable source of high-quality and large-area graphene film remains challenging. Based on the optimised growth parameters on HOPG, which provided a repeatable substrate surface, we demonstrate MoO₃ growth models in examples of various types and qualities of available graphene films.

Graphene can be synthesised on a number of substrates. Depending on the chosen substrate, grown graphene layers are characterised by different properties, which are often contradictory, e.g., either transferable but defective or of high quality but bonded to the substrate, to name crucial ones from the perspective of this study. Graphene synthesised on two selected substrates will be presented as a building block of graphene heterostructures with MoO₃:

- I. graphene on copper;
- II. graphene on silicon carbide.

To compare the MoO₃ growth modes on selected substrate surfaces, the presented results underwent a similar experimental procedure, which consisted of pre-growth graphene UHV annealing and deposition on a heated substrate. Note that slightly different parameters were often used in seeking optimum growth conditions. Parameters are given in figure captions. The findings in this Chapter provide valuable information for the growth behaviours of 2D MoO₃ heterostructures based on atomic force microscopy (AFM) in semi-contact and contact mode (c-AFM) as well as low energy electron diffraction (LEED) studies.

4.1. Introduction to Graphene/MoO₃ Heterostructures

As mentioned, the literature describes the fabrication of graphene/MoO₃ heterostructures without much discussion of the morphology of MoO₃ films. Only scarce effort towards morphology, available in the literature, is limited to results performed in an uncontrolled environment [6,19,70,71].

Studies on thin MoO₃ films by two research groups are worth mentioning. Essential steps in studying graphene/MoO₃ heterostructures were taken by Meyer *et al.* [19] and Wu *et al.* [6], reporting on tuning the work function of the heterostructure to high values by increasing the film thickness. In particular, Meyer *et al.* [19] show the morphology of deposited films: at submonolayer coverage, MoO₃ nanoclusters decorated the graphene surface, which indicates a Volmer-Weber type nucleation mode (i.e. island formation). Such heterostructures require relatively thick films to obtain desired high work function, which MoO₃ offers. Thus, the controllable method to grow 2D MoO₃ films may open up new possibilities for practical uses while downscaling MoO₃ thicknesses to their physical limit, i.e. monolayer.

In a couple of papers, Kim *et al.* [70,71] reported on 2D single-crystal MoO₃ on multilayer graphene or graphite, where square-like nanosheets were obtained. However, the thinnest measurable MoO₃ nanosheet was bilayer (1.4 nm) due to instability of irregularly shaped monolayer with the thickness of approx. 0.7 nm, as suggested in their first paper [70]. The growth of the 2L MoO₃ films was in ambient conditions. The multilayer MoO₃ of rectangular shape on graphene was reported therein and also by Cai *et al.* [70,75].

In this study, we continue with graphene, which in principle is known for its atomically smooth and chemically inert surface, as the growth template for MoO₃ via thermal evaporation in UHV. We find the ability to synthesise 2D high-quality α -MoO₃ films under UHV conditions superior to the previous reports, as it allows direct *in-situ* characterisation. Thus, it leads to fundamental research and a significant advance in our understanding of their properties.

Another important factor to consider for anode applications is surface roughness, where 2D films provide excellent smoothness. Moreover, no structural defects should be developed in graphene during the MoO₃ growth process to guarantee high quality. The previous transmission electron microscopy (TEM) images (Figure 9) indicate that the multilayer graphene is not damaged during the deposition of MoO₃. According to the previous reports, Raman spectroscopy indicates that such a deposition does not defect graphene structure [70]. Thus, graphene/MoO₃ heterostructures may take advantage of the high quality of both components and be a subject of nanoscale investigations.

4.2. Results and Discussion: Effect of Graphene Substrate on the Growth of MoO₃ Thin Films Grown by Thermal Evaporation

To investigate the effect of the graphene properties on the MoO₃ growth, the synthesis was carried out with different growth substrates, namely graphene synthesised on different materials and by different methods: chemical vapour deposition (CVD) and graphitising SiC, which result in either monolayer or few-layer graphene films.

4.2.1. Graphene on Cu: Morphological Characterisation

The first graphene substrate to be challenged in this study is copper. Although Cu may not be an obvious choice of a substrate for graphene and further applications, especially regarding the necessity of high transparency, Cu can be used as a surrogate substrate and allow subsequent transfer onto transparent glass or polymer film (PET) substrates [10,106]. Moreover, Cu has the potential to be an excellent economical choice. The pioneers of CVD graphene were using Cu because of its advantages: catalytic power, price, and availability [10].

Cu metal allows controllable synthesis of single-layer graphene with relatively low carbon solubility [10,140] and weak binding force with graphene [10,141], where graphene on Cu foils should be described as polycrystalline material [142]. The polycrystallinity may influence the local growth processes of MoO₃, which we describe below.

The Cu/graphene was used in the first and already mentioned reports of graphene/MoO₃ heterostructures by Wu *et al.* [6] and after transfer onto SiO₂ or glass substrates by Meyer *et al.* [19].

AFM was used to assess the quality of Cu/graphene. AFM micrographs in Figure 18a-b show that graphene on Cu is characterised by relatively high roughness on revealed numerous steps. The surface of the pristine graphene is only locally smooth, with an overall root-mean-square (RMS) value of 9 nm, in Figure 18a. The phase image in Figure 18b shows continuously the same contrast on all Cu terraces, where only step edges appear as narrow regions are suggested to have different surface properties. The AFM scans showing the surface before the MoO₃ growth help recognise the substrate topography and the subsequently grown structures. It should be noted, that the graphene film is supposed to be continuous over the observed step edges of Cu substrate, however such continuity is not preserved between domains, which are present in graphene layers [142].

The typical result of thermal evaporation of MoO₃ on Cu/graphene is presented in Figure 18c, where MoO₃ forms three-dimensional (3D) nanoclusters. The distinct surface

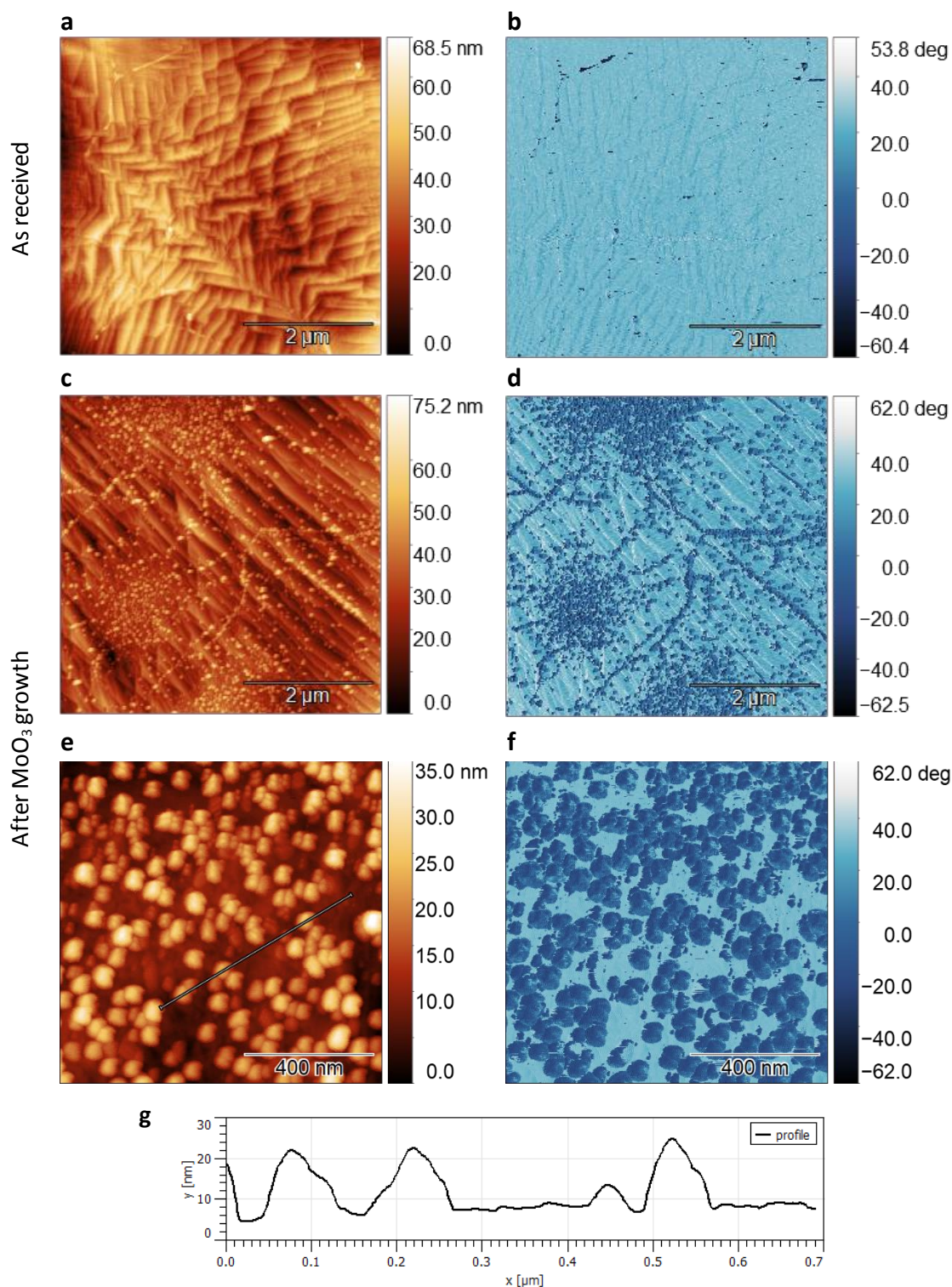


Figure 18: AFM micrographs of graphene synthesised on Cu before and after MoO_3 deposition. Semi-contact AFM topographies in (a), (c), and (e); the corresponding phase-contrast images in (b), (d), and (f), which highlight MoO_3 deposited structures. The dark blue areas indicate the MoO_3 nanoclusters, while the light blue represents graphene regions. (g) height profile taken across the marked line in (e) averaged over 10 px. Scan sizes: (5×5) and $(1 \times 1) \mu\text{m}^2$. Roughness: (a) RMS = 9 nm, (c) RMS = 8 nm, (e) RMS = 6 nm. Process parameters: pre-growth substrate UHV annealing (350°C , 1 h), growth on the heated substrate (265°C).

properties allow differentiation of MoO₃ from neighbouring graphene in the phase map (Figure 18d). The clusters are not evenly distributed over the graphene surface but are accumulated in particular areas and decorate preferential lines – see the phase-contrast image in Figure 18d with a vivid contrast between two materials highlighting those accumulations.

The observed accumulation of MoO₃ nanoclusters suggests strong binding energy between MoO₃ and some regions of the substrate surface, which leads to the selective nucleation of MoO₃ and 3D growth instead of wetting the graphene surface. The line-type decoration by nanoclusters seems to take place on graphene domain boundaries, which may indicate their strong influence on the growth process, presumably where the surface is not atomically flat (e.g., graphene domain edge exists or its continuity has been interrupted) and there are dangling bonds present. Interestingly, note that the step edges of the Cu substrate (visible in phase image in Figure 18d as a bright lines) have negligible, if any, influence of MoO₃ nucleation. This indicates that the nucleation is driven mainly by the defects in which the continuity of graphene is not preserved and graphene folds (as over step edges) do not limit the MoO₃ diffusion.

When we compare the roughness of the surfaces before and after MoO₃ deposition, we cannot draw any conclusion (RMS after deposition is 8 nm in Figure 18c, and 6 nm in zoom-in, Figure 18e), as the as-received Cu/graphene is rough intrinsically. To investigate the sizes of MoO₃ nanoclusters shown in Figure 18e-f, we derived a height profile taken across the surface in Figure 18e (average of 10 px) – see Figure 18g. The profile presents the heights of the MoO₃ structures of approx. 15 nm.

AFM experiments show that the growth of MoO₃ on Cu/graphene leads to the favourable formation of 3D nanoclusters. The average diffusion path must be limited on this type of graphene either because of its defected surface or because of the interaction of graphene with the Cu substrate, which causes surface potential perturbations and can act as a local trap for diffusing molecules. On the other hand, we believe that the Cu/graphene substrate is relatively clean although the annealing applied may not entirely ensure the removal of chemically adsorbed molecules. However, annealing at a higher temperature could induce structural defects in graphene.

The direct translation of growth parameters from HOPG to Cu/graphene leads to undesired 3D type structures, which would not be advantageous compared to literature reports [6,19]. After numerous trials of tuning pre-growth substrate preparation and growth parameters, the Cu/graphene substrate did not allow desired lateral 2D growth. For example, one of the parameters that have been tested was the temperature of the substrate during the MoO₃ deposition; while from RT to 315 °C, the growth leads to 3D clusters as presented above,

at higher temperatures up to 400 °C, nanoclusters decorate only the boundaries of graphene domains leaving the graphene fully uncovered due to longer range of mobility of MoO₃ species on the surface of growth template. The latter observation may indicate that the graphene within domains has low defect density preventing nucleation of MoO₃ or that the MoO₃ molecules had enough energy do not to stop on these defects. Besides, such a high temperature of the substrate probably caused re-evaporation of deposited material. Then, the only structures left are those which have adsorbed in large wells of potential. On the other hand, other parameters we tested – the duration and temperature of pre-growth annealing of Cu/graphene – lead to the same MoO₃ growth.

4.2.2. Graphene on SiC: Morphological and Crystallographic Characterisation

As a commercially available semiconducting or semi-insulating substrate, silicon carbide has the main advantage that the graphene films grown on such substrate are considered an attractive solution for directly integrating graphene in electronic devices. Therefore, no damaging transfer process is required [143]. Moreover, using SiC has potential in electronic applications operating at high frequencies, voltages, and temperatures [143].

Furthermore, SiC allows synthesis of high-quality graphene, which may be the closest to exfoliated 2D flakes from graphite [10], and can be the next step in expanding the potential of our studies of HOPG/MoO₃ structures. We expect the two substrates, HOPG and SiC/graphene, to behave the same in supporting MoO₃ during a deposition process, as the top surface layer is of the same graphene proving the high quality of the latter. However, not all graphene substrates provide repeatable and defect-free surfaces. In the following paragraphs, we show three examples of achieved results in MoO₃ deposition: two on monolayer graphene and one on few-layer graphene.

We start with monolayer graphene synthesised by CVD on SiC (hereafter referred to as ML-graphene). The surface of as-received ML-graphene is presented in Figure 19a-b. Typically, after the graphene synthesis process on a SiC substrate, it is characterised by many faults. These faults are edge groupings of SiC terraces as seen in c-AFM topography image, Figure 19a. The heights of such faults change depending on the process used in graphene growth. Figure 19a shows one such fault with a height of about 15 nm. However, the available data show that graphene covers both terraces and faults, which are present on the surface.

We used AFM lateral force measurement to characterise the graphene substrate further. In this configuration, a tip is sensitive to changes in surface properties and can

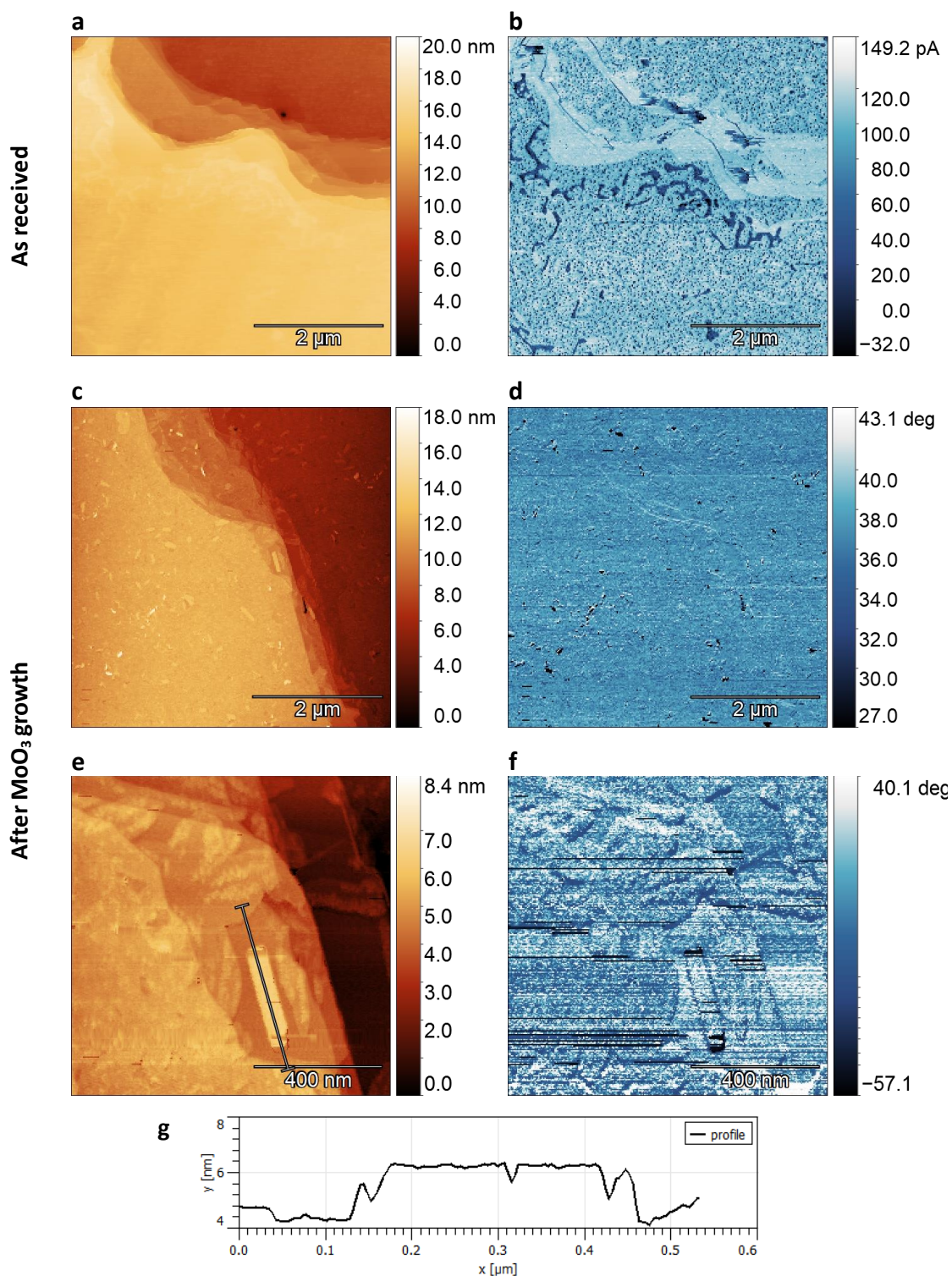


Figure 19: AFM micrographs of monolayer (ML) graphene synthesised on SiC before and after MoO₃ deposition on top. As-received ML-graphene on SiC: Contact AFM topography in (a) and the corresponding lateral force in (b) to highlight the heterogeneity of surface properties. MoO₃ on ML-graphene: semi-contact topography in (c and e) together with the corresponding phase-contrast image in (d and f), which highlights full coverage by deposited MoO₃ structures. (g) height profile taken across the marked line in (e) averaged over 10 px. Scan sizes: (5 × 5) μm². Roughness: (a) RMS = 2.5 nm, (c) RMS = 3 nm. Process parameters: pre-growth substrate UHV annealing (330 °C, 1 h), growth on the heated substrate (220 °C).

discriminate between areas of different friction coefficients while the tip is moved across the sample surface. The lateral force image recorded on ML-graphene is shown in Figure 19b. It shows a significant variety of contrasts, which indicates different coefficients of friction in given areas of the ML-graphene surface. It is worth mentioning that the change, in contrast, can also occur due to topographical changes on the surface, which occurs on faults. This is clearly seen in Figure 19b, where the contrast on the faults is visibly different than at some distance from them. However, this figure also shows structures with non-regular contours appearing particularly near the fault at the upper edge (these structures can also be seen in the topographic image, Figure 19a). However, they appear not only near the edges but on all terraces with different densities. In our opinion, these changes attribute to discontinuities of graphene surface, indicating some degree of defectiveness in available ML-graphene substrates.

In the first example of MoO₃ growth on SiC/graphene, the AFM micrographs of the deposited film are shown in Figure 19c-d. The ML-graphene surface seems to be fully covered by deposited material – see uniform contrast in phase map, Figure 19d. While the majority of the grown material appears amorphous, some patches are covered by crystalline-like grains. The shape of the grains is elongated as needle-shaped or thicker bars. As in many references mentioned in Table 1, it is common in the α -MoO₃ phase that crystallites grow in square or rectangular nanosheets. To measure the dimensions of the elongated grain, we extracted a height profile across the marked line in Figure 19c (averaged over 10 px), which is shown in Figure 19g. The profile reveals a flat surface of the grain and its height of about 2.1 nm, which suggests 3 layers of α -MoO₃. Note that the overall roughness increased after MoO₃ deposition (from RMS = 2.5 nm to 3 nm, Figure 19a and c, respectively). However, the surface of the grain is smooth without additional protrusions, which confirms more than 1 layer of α -MoO₃ – more discussion on topographical protrusions on MoO₃ monolayer is in Chapter 5.

Due to heterogeneity of the as-received substrate surface, we attribute mixed growth mode to a significant number of defects. Therefore, the mean free path of MoO₃ species is too short to promote only the desired lateral, crystalline and monolayer films.

The second example of MoO₃ growth on SiC/graphene is presented in Figure 20a-b. The substrate tested here is one of the same ML-graphene samples as in the previously discussed example (see Figure 19a-b). The AFM topography of another MoO₃ film on ML-graphene is shown in Figure 20a. Despite the same deposition procedure, the resultant MoO₃ film appears entirely amorphous (note relatively high RMS of 2.5 nm as for two terrace area), without any signs of grain crystallites. The corresponding phase-contrast image (Figure 20b) suggest full coverage of ML-graphene.

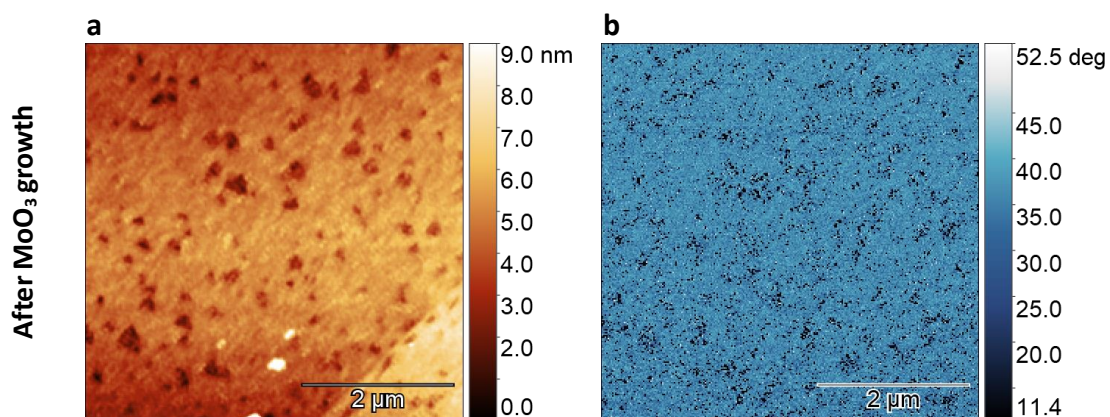


Figure 20: AFM micrographs of ML-graphene on SiC after MoO₃ deposition. Semi-contact AFM topography in **(a)** together with the corresponding phase-contrast image in **(b)**. Scan sizes: (5 × 5) μm². Roughness: (a) RMS = 2.5 nm. Process parameters: pre-growth substrate UHV annealing (330 °C, 1 h), growth on the heated substrate (220 °C).

These dissimilar results showed us that for defective ML-graphene substrates it is impossible to achieve reproducibility of the growth process. Even though the signs of desired crystallization process were observed for one sample, it did not occur for the second one. This made any approach to optimizing growth inefficient or impossible. The unfortunate lack of repeatability in obtained results shifted our focus towards few-layer graphene, which may provide higher reproducibility.

For the third example of MoO₃ growth on SiC/graphene, we used few-layer graphene fabricated by BeeGraphene, graphitising SiC surfaces in Si flux [115] (hereafter referred to as FL-graphene). The morphology of the as-received FL-graphene surface is presented in Figure 21a-b. This FL-graphene is characterised by uniform surface, as seen in topography in Figure 21a, despite many terraces in scanned area. The difference in the diversity of surface properties is significant compared to the previously described example. This is especially visible when we compare the phase images for ML-graphene (Figure 19b) and FL-graphene (Figure 21b). For FL-graphene we observe the uniform contrast with only slight disturbances from subsurface topography, while ML-graphene showed high concentrations of dark spots related to intense tip-surface interaction caused by the presence of defects.

In contrast to the previous example, including especially graphene on Cu, the translation of growth parameters from HOPG to SiC/FL-graphene leads to desired lateral 2D growth type structures, which would be advantageous compared to literature reports. The topography of such layers is presented in Figure 21c. The corresponding phase image in Figure 21d clearly distinguishes between MoO₃ nanosheets and uncovered graphene.

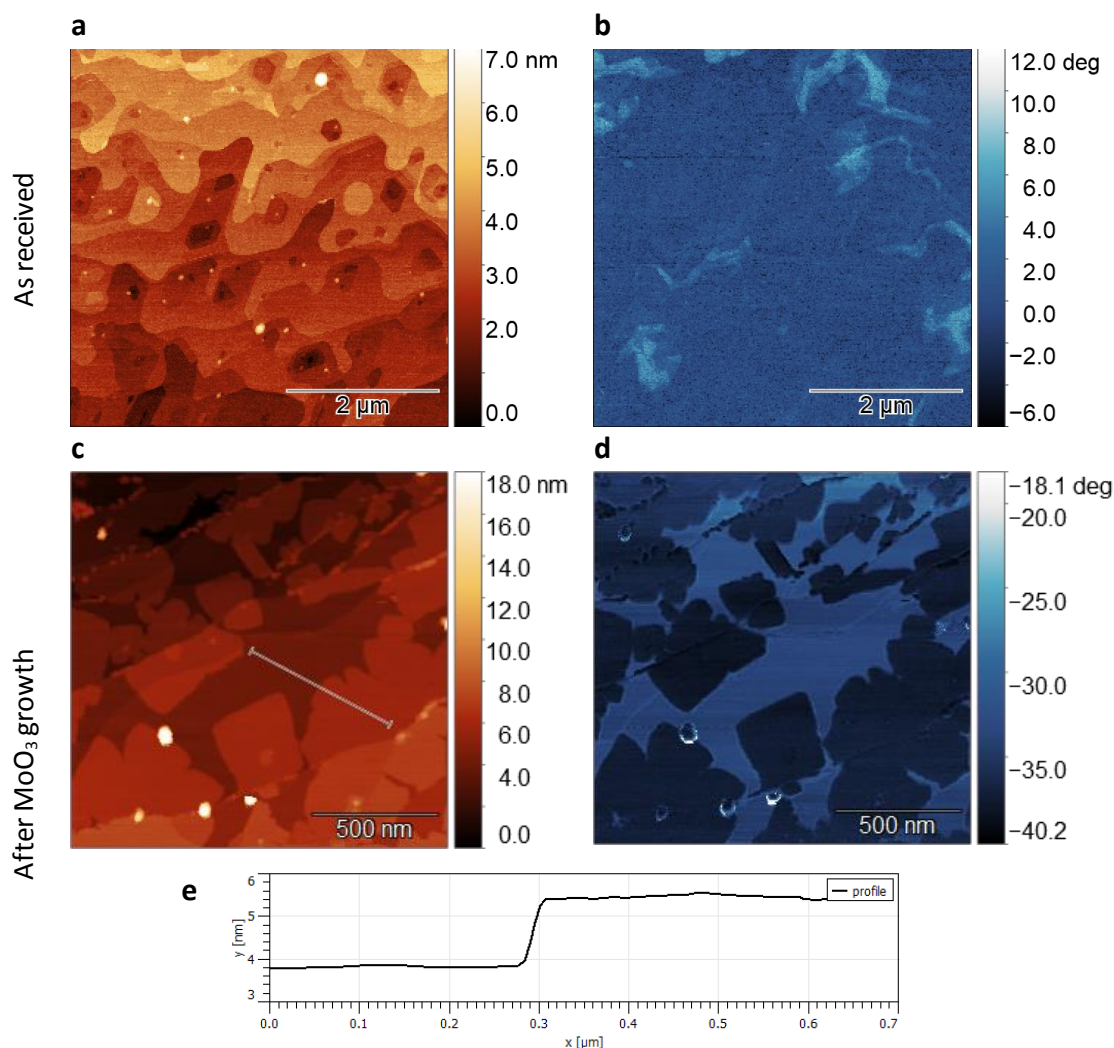


Figure 21: AFM micrographs of few-layer graphene on SiC before and after MoO₃ deposition on top. Semi-contact topography in (a) and (c), together with the corresponding phase in (b) and (d), which highlights MoO₃ deposited structures. (e) height profile taken across the marked line in (c) average of 10 px. Scan sizes: (5 × 5) and (2 × 2) μm². Roughness: (a) RMS = 1 nm, (c) RMS = 2 nm. Process parameters: pre-growth substrate UHV annealing (440 °C, 3 h), growth on the heated substrate (250 °C).

Similarly to HOPG, the growth mode on FL-graphene is layer-by-layer according to AFM observations, suggesting vdW epitaxy. The AFM micrographs reveal the flat morphology of the surfaces. Note that the MoO₃ nanosheets grow over the edges of the terraces (Figure 21c-d), indicating continuous graphene film and suggesting similar growth kinetics as on HOPG. The profile taken across the surface in Figure 21c (average of 10 px) is shown in Figure 21e, and it presents the thickness of the MoO₃ island of approx. 1.5 nm. This thickness is closer to 2L (1.4 nm) than 1L (0.7 nm); however, we observed that measurements in ambient are notably affected by adsorbents. A more detailed thickness investigation is described based on measurements in UHV (see Chapter 5). However, the number of layers more than 1 agrees with previous reports on 2D MoO₃ on graphene-like substrates found in the literature [70,75]. While

on HOPG we clearly achieved monolayer growth, the difference for FL-graphene may be due to different interaction energy between MoO_3 and the substrate. Confirmation of such a hypothesis would be possible by DFT calculations which, however, seem to be very difficult due to the required large size of supercells and, therefore, lack of possibility to perform calculations in a finite time.

Successful 2D growth of MoO_3 is achieved through the additional graphene layers on the SiC substrate due to the uniform surface properties of graphene promoting the diffusion (the high diffusion rate and length) of adsorbed MoO_3 species along the in-plane direction. The results indicate that FL-graphene is a viable substrate for the lateral growth of other 2D materials.

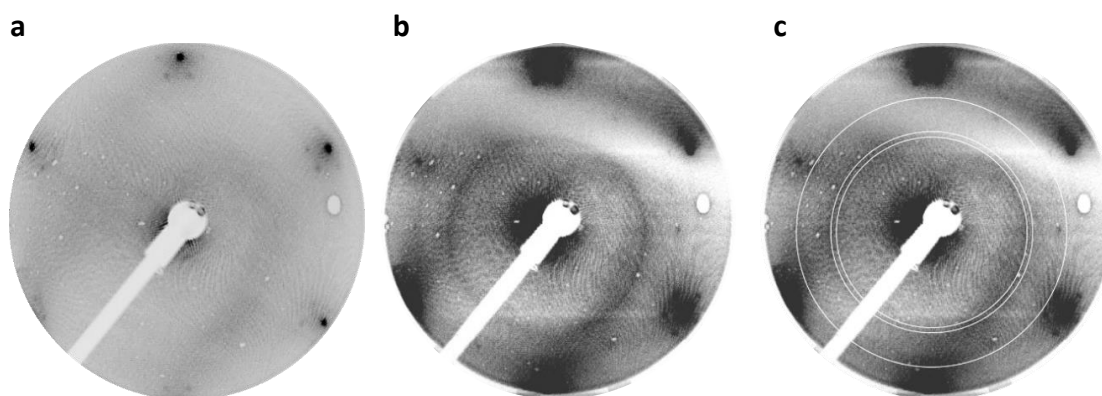


Figure 22: LEED patterns of MoO_3 nanosheets on SiC/FL-graphene at energy of 55 eV. (a) diffraction from a region where the intensity of first-order spots from FL-graphene is high while MoO_3 pattern has low intensity due to insufficient MoO_3 coverage. **(b-c)** diffraction from a region where intensity from MoO_3 surface results in two rings. For clarity, in (c), a schematic of the diffraction rings is drawn: the white rings correspond to the rectangular MoO_3 structure. Process parameters: pre-growth substrate UHV annealing (440 °C, 3 h), growth on the heated substrate (250 °C), post-annealing (UHV, 100 °C, 1 h).

For further characterisation of the MoO_3 nanosheets on FL-graphene, we employed LEED, which may indicate crystallography information on epitaxial relation between MoO_3 and the graphene substrate and verify whether the proposed process of MoO_3 deposition disturb the surface crystallography of FL-graphene.

In the previous Chapter 3 (Figure 8), we commented on the HOPG/ MoO_3 LEED pattern featuring rings that imply random in-plane rotation of domains for HOPG and 2D MoO_3 . The LEED measurements (performed at room temperature and energy of 55 eV) of FL-graphene/ MoO_3 are shown in Figure 22. The diffraction features of graphene are seen in Figure 22a. Notably, the central spots of the hexagon pattern are surrounded by additional spots forming flower-like hexagon patterns around the main spots. The flower-like patterns can be

attributed to $(\sqrt{3} \times \sqrt{3})R30^\circ$ reconstruction and are characteristic of buffer layer and graphene overlayers [144], indicating few-layer graphene film on SiC. The observation of nearly pure graphene pattern was possible due to the low and non-uniform coverage of the measured sample, which allowed focusing the beam on exposed graphene in between the MoO_3 nanosheets.

Figure 22b-c present a diffraction pattern from a more covered area where two rings are observed next to graphene spots, revealing a multidomain MoO_3 lattice. Note that the inner ring is thicker than the outer, which corresponds to first-order and higher-order diffraction spots of the rectangular α - MoO_3 structure in (010) plane, respectively. For simulation of the diffraction pattern of three-domain α - MoO_3 , see Figure 8. For clarity, in Figure 22c, three white rings were drawn inside the graphite features. Therefore, in the case of FL-graphene/ MoO_3 , we do not see any defined orientation between graphene and MoO_3 domains. The fact that a random epitaxial relationship exist suggests negligible deposition to substrate interaction at their hetero interface.

Furthermore, despite blur, the characteristic diffraction pattern of graphene after the MoO_3 deposition may indicate that FL-graphene has not been significantly damaged during the process.

Exhaustive STM imaging of MoO_3 layer on FL-graphene substrates was performed at various combinations of working parameters, such as bias voltage and current. However, those trials did not produce representative information on either morphology or electronic structure. We observed the high mobility of MoO_3 structures on graphene, which hinders nanoscale measurements by STM. This observation is in line with previously reported high mobility of MoO_{3-x} monolayers in ambient by Kim *et al.* [70].

A thicker MoO_3 layer was deposited on FL-graphene to check the possibility of STM measurements. Note that the substrate was kept at a low temperature (50 °C) during the deposition process to minimise the diffusion and promote higher nucleation site density to allow full coverage. The thicker layer was expected to be more stable than MoO_3 clusters or monolayer islands.

Optical image (Figure 23a) taken in AFM microscope after STM scanning presents a pattern made in the MoO_3 layer by STM tip in ambient conditions. The inset illustrates the pattern: four rectangular STM scans were taken. Around each scan window, there is a visible accumulation of the swiped material appearing as a dark frame.

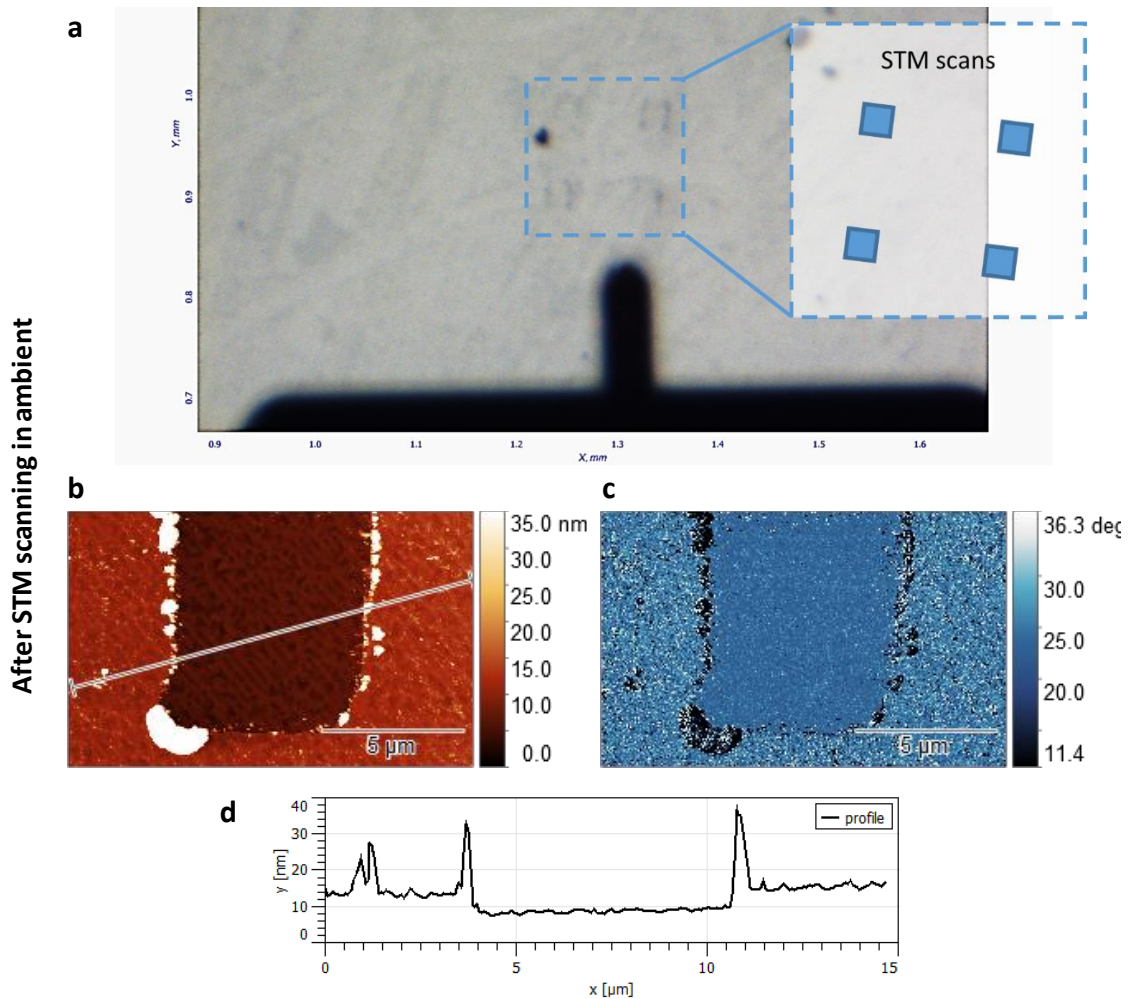


Figure 23: Result of STM scanning in ambient: (a) optical image of FL-graphene/MoO₃ after STM scans taken in a pattern shown in the inset. AFM micrograph of cleared window by STM uncovering the graphene substrate: (b) semi-contact topography together with (c) the corresponding phase. (d) height profile taken across marked line in (b) average of 10 px. Scan size: (14 × 10) μm². Process parameters: pre-growth substrate UHV annealing (300 °C, 3 h), growth on the heated substrate (50 °C).

Semi-contact mode AFM images of the locations of the prior STM scans are shown in Figure 23b-c. The topography reveals clean rectangular window in the centre (Figure 23b), while the corresponding phase image confirms removing MoO₃ down to the substrate surface (Figure 23c). STM is known to be able to clear surfaces while a tip acts as a 'broom' to sweep the material from the scan area [145,146]. As mentioned earlier, the cleared window is surrounded by accumulation of the MoO₃ material in uneven chunks around the edges. The profile taken across the topography image (see Figure 23d) finally confirms the uncovered area of graphene together with a surrounding layer height of approx. 5 nm and accumulation line up to 25-nm high with respect to the MoO₃ surface. Because the accumulated material seem to build relatively small banks, it may be explained by agglomeration of particles around the probe [146]. If so, in

consequence, the accumulated material at scan edges would be due to a pick-up-drop-off process rather than mechanical dragging of particles to the side.

The observed high mobility and easy MoO₃ removal by STM point towards low adhesion on graphene/MoO₃ interface. This, unfortunately, prevents us from studying electronic structure on the nanoscale. However, it is ideal for nanomanipulation studies and precise nanopatterning.

4.3. Conclusions

The obtained results collected information about the potential of graphene layers grown on selected substrates to surrogate MoO₃ layers. Based on the results presented in this and the previous Chapter 3, we can compare the growth mode of MoO₃ on HOPG and graphene, where HOPG is considered an initial model of a graphene system. The HOPG substrate had a better crystallinity providing reproducibility in a controlled manner, while the graphene substrates available in our study were not uniform and resulted in various deposited structures. The main findings are listed below.

- I. Cu/graphene as a surrogate substrate for MoO₃ promotes 3D growth, while the nucleation takes place in preferential areas, presumably where defects are accumulated as MoO₃ structures decorate domain boundaries. Although Cu offers transferability, Cu/graphene does not allow the growth of MoO₃ layers but leads to MoO₃ high agglomeration on the graphene surface.
- II. There is a variety of SiC/ML-graphene surfaces, which lead to the growth of different MoO₃ structures from amorphous to crystalline in an unrepeatable manner.
- III. While monolayer graphene appeared to be an unreliable substrate, few-layer graphene promotes the desired layer-by-layer growth mode of MoO₃ by providing a low energy barrier MoO₃ species migration and promoting the lateral growth.
- IV. MoO₃ islands take random orientation on the FL-graphene surface for the given surface nanosheet dimensions, suggesting random epitaxial alignment.
- V. There is low adhesion between MoO₃ and FL-graphene, hindering STM measurements on the nanoscale. Our experiments show that the nanoparticle system of MoO₃ on graphene is an ideal candidate for nanomanipulation.

To sum up, there is a high dependence on the quality and purity of graphene, which could serve as an advantageous substrate for MoO₃ lateral growth. Due to the insufficient quality of the tested graphene substrates, the processes of nucleation and the formation of flat MoO₃ layers are disturbed. With an increase in the number of layers and a decrease in the

number of graphene defects, nucleation begins to proceed similarly to that observed on the HOPG. Therefore, this Chapter set landmarks in the growth characteristics of MoO₃ on graphene, proving that FL-graphene is a suitable substrate for synthesising 2D MoO₃. Such informational gain is fundamental for designing further steps to completely understand the nature of graphene/2D MoO₃ heterostructure.

5. Work Function of α -MoO₃ Monolayers in Heterostructures with Graphite and Graphene

The MoO₃ electronic structure directly translates into applications, where the work function (WF, Φ) has tremendous significance in performance of devices [43]. According to the literature, the high WF of MoO₃ (for bulk 6.9 eV [19,38,42,43]) is tuned by film thickness and is dependent on the substrate for the first layers of MoO₃. The MoO₃ work function is known to be notably degraded by exposure to air [42,43]. However, it has also been reported that even air-degraded MoO₃ films maintain efficient performance in devices [42].

Chapter 3 showed that 2D MoO₃ on HOPG offers the WF of 5.7 eV measured globally over around 70% coverage and monolayer thicknesses. On the other hand, results in Chapter 4 proved that monolayers of MoO₃ can be grown on graphene. Therefore, 2D MoO₃ offers the possibility of fabricating transparent graphene-based anodes with desired properties, i.e. tuned work function. There is a gap in the literature concerning the WF of 2D MoO₃. The work presented in this Chapter is the first to report MoO₃ monolayers ensuring efficient enhancement of substrate WF.

In contrast to previous reports, we emphasise that crystalline 2D MoO₃ guarantees high WF, and in this regard, the material does not require thicker but coalesced monolayers. Furthermore, our study not only provides nanoscale results by non-contact atomic force microscopy (nc-AFM) and Kelvin probe force microscopy (KPFM) in controlled ultrahigh vacuum (UHV) conditions, but also positively verifies that commonly accessible ultraviolet photoemission spectroscopy (UPS) is, under defined here circumstances, suitable for the determination of WF attributed to 2D nanosheets on a substrate with lower WF. Both of our observations carry important implications in the design of van der Waals heterostructures for energy-level alignment and characterisation of 2D materials beyond MoO₃.

This Chapter aims to fill the literature gap; it focuses on the work function of heterostructures built by monolayers of MoO₃ and graphene-like substrates. It is divided into three sub-chapters to answer the following questions:

- I. What are the values and local distribution of work function of the heterostructures in ambient conditions? How air exposure affects the local work function of the MoO₃ monolayer? Are the properties of the first layers of MoO₃ considerably different, namely is the first layers different from the second layer?
- II. What is the work function of 2D MoO₃ if it was kept in a controlled (UHV) environment?

- III. Is it possible to restore the high work function of air-exposed MoO₃ monolayers? And if so, to what extent? Does duration of exposure make a difference in subsequent restoration?

5.1. Introduction

Many research groups have focused on determining the dependence of TMO electronic properties on film thickness [6,19,20,37,38]. Concerning MoO₃ and its WF, there are numerous relevant bodies of literature on the influence of film thickness and a substrate type on the WF value [6,19,37–41]. In particular, much effort was taken to increase WF of MoO₃ by increasing film thickness [6,19,37,41]. Those works showed that the highest WF value can be observed only at a particular film thickness from which the WF is as high as for bulk. In the case of MoO₃ films on graphene substrates, a gradual increase along with thickness has been reported. At MoO₃ thickness of 1.4 nm (bilayer), it reaches 5.9–6.4 eV [6,41], while saturation (≤ 6.8 eV) occurs for thicker films of around 4.0–5.0 nm [6,19,37]. Those investigations were performed by UPS.

However, the electronic structure of α -MoO₃ has been predicted not to alter with decrease in a number of layers down to a monolayer [44–48] (see also Section 3.2.5.2). α -MoO₃ in bulk form possesses WF as high as 6.9 eV [19,38,42,43], which is higher than work functions of HOPG and graphene (4.2–4.6 eV [19,20,136,137]). Therefore, we propose that monolayer α -MoO₃ films can be considered sufficient for enhancing WF of graphene heterostructures while downscaling the thickness to < 1 nm of films currently used for tuning WF.

Not only the accurate determination of work function is crucial, but also its homogeneity for future applications. This issue leads to choosing the most suitable technique for obtaining such information: local technique such as KPFM or global one such as UPS. In principle, both techniques provide information on WF value and its distribution over the studied area, however, on different scales. Uncoalesced films are typical for 2D materials, which leads to uncertainty in UPS measurements. UPS has proven its importance in surface science; however, measurements on multicomponent samples with laterally heterogeneous WF, e.g. with monolayer nanosheets, require careful investigation [33,41,119–121], and are only valid under certain sample conditions, as has been extensively described in the Experimental Section 2.4.

We believe that the highest possible work function of MoO₃ monolayer (1L) has not been experimentally revealed partially due to the uncontrolled environment as well as underestimation of UPS results. A great example of the latter is the first interpretation of UPS spectrum (Figure 15b) on heterogeneous in WF surface, i.e. HOPG/1L-MoO₃. The presented result was a WF of 5.7 eV, which is a significant improvement compared to bare HOPG. However,

we need to note that 1L-MoO₃ did not fully cover HOPG, and the coverage was estimated to be approx. 70%. A closer look at the shape of the secondary electron cut-off (SEC) determining the WF value reveals a broad and tilted edge. The broad spectral distribution is due to emission contributions from two surface components: 1L-MoO₃ and uncovered HOPG. Thus, the value of 5.7 eV is not a WF of pure 1L-MoO₃, meaning the monolayer of MoO₃ can have higher work function as predicted. More on SEC interpretation is discussed below in this Chapter and Experimental Section 2.4. On the other hand, local work function measurements are missing in the literature for 1L-MoO₃, in particular considering different environments.

In material science, comprehensive characterisation requires external facilities, specific equipment, and collaboration. Such requirements lead to dealing with transfer of samples. For susceptible to moisture surfaces, which is the case of molybdenum oxides, breaking the UHV environment significantly affects electronic properties that are of interest to this work. Therefore, the transfer issue has been encountered in the process of this study, where a vacuum suitcase could not be used. The aroused need included either a reliable transferring atmosphere of inert gas in a reliable container or a method to restore the previous properties. Regarding the former, there is another issue with the protective atmosphere. When a sample reaches its destination, it needs to be introduced into a UHV system, which requires exposure to air again. Only facilities equipped with glove boxes and vacuum suitcases, or similar solutions would be compatible and avoid exposure. Given the above arguments, a method of electronic properties restoration is demanded after air exposure.

Another topic that has been widely investigated was indeed restoring the high WF value of MoO₃ after air exposure [6,19,37,42,43]. Monolayer and few-layer MoO₃ properties strongly depend on the processing history and ambient environment. Air exposure degrades the WF of MoO_x from 6.9 eV to ~5.2 eV for bulk MoO₃ [42,43] and to ~4.7 eV for MoO₃ monolayer (Figure 15b). It is due to the effect of oxygen, moisture, and impurities on MoO_x films [43,147], which can be partially recovered via simple annealing. In the literature, many attempts have been made to recover the high WF of air-exposed MoO_x films, e.g., the recovery was measured to be over 60% at an annealing temperature of about 450 °C [148]. However, MoO_x is easily reduced while annealing [65]. Even with successful approaches, those studies were focused on neither proving that the electronic structure of α -MoO₃ is independent of a number of layers nor nanoscale measurements. The latter turns crucial when going down in thickness to a monolayer.

5.2. Results and discussion

5.2.1. Local Surface Potential of Monolayer MoO₃ in Ambient Conditions

We start with KPFM local surface potential measurements, i.e., mapping contact potential difference (CPD), which is directly related to work function. The study in ambient is focused on morphology and work function distribution, along with investigation of differences between the first MoO₃ layers, namely the differences between the first and the second deposited layer.

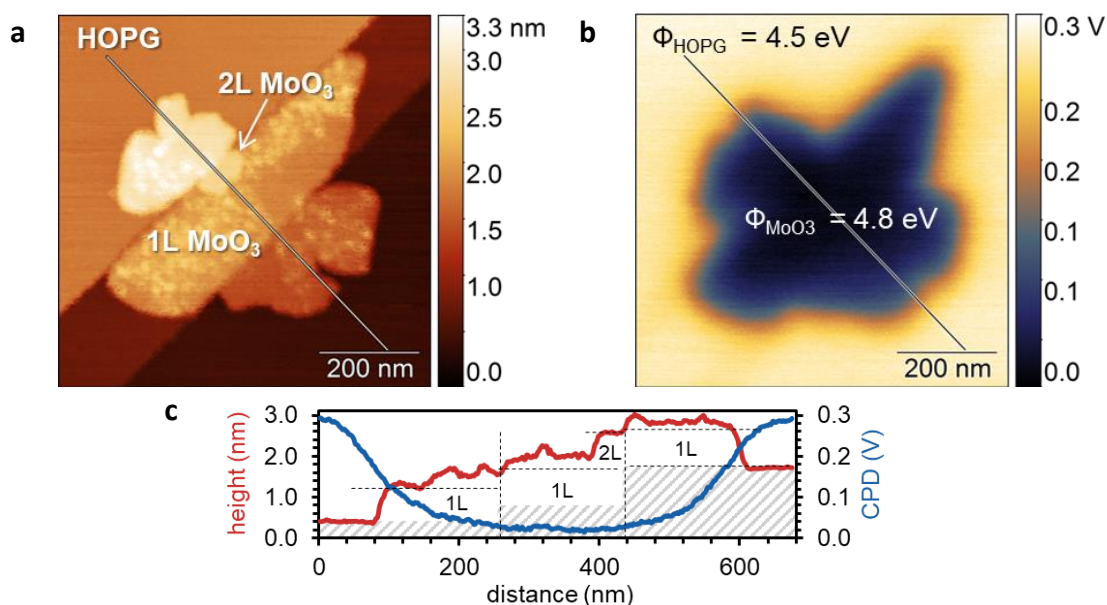


Figure 24. Local surface potential of MoO₃ monolayer (1L) on HOPG: KPFM measurement in ambient. (a) AFM topography. **(b)** corresponding contact potential difference (CPD) map. Yellow colour of CPD signal is attributed to low work function, while blue colour to higher work function. Line profiles through the images are presented in **(c)**. For clarity, the number of layers is indicated from 1L to bilayer (2L) as well as the work function values, Φ . Scan sizes: $(1 \times 1) \mu\text{m}^2$. Process parameters: pre-growth substrate UHV annealing (380 °C, 1.5 h), growth on the heated substrate (220 °C).

To focus on local air exposure effects, we applied KPFM to investigate the surface potential and WF under ambient conditions. Figure 24 shows a KPFM measurement of HOPG with MoO₃ nanosheets. Topography, in Figure 24a, presents monolayer (1L) MoO₃ nanosheets on three HOPG terraces. In the centre, there is also a small nanosheet indicating two stacked MoO₃ layers (2L). The smooth topography is affected by height variations in the form of unevenly distributed perturbations over nanosheets, which are typically observed in air. The contact potential difference between the HOPG substrate and MoO₃ is clear in Figure 24b. Yellow colour is attributed to a high CPD signal, which corresponds to a low WF (HOPG), while blue colour indicates a higher WF (MoO₃). Figure 24c presents overlaid profiles extracted from the topography and the corresponding CPD (marked by lines in the images). The heights of MoO₃

nanosheets are 0.9 ± 0.2 nm for monolayer (1L) on each terrace and 0.8 ± 0.1 nm for 2L. The potential values of two materials are calculated by taking the average values from an area where values are constant away from nanosheet edges, e.g. see horizontal plateaus in the CPD profile ($CPD_{HOPG} = 0.29$ V; $CPD_{MoO_3} = 0.03$ V). The surface potential in the middle of the MoO_3 nanosheets is lower than the HOPG background by 0.26 V (the CPD difference changed from place to place and varied in range of 150 meV). Note that the gradient at edges of MoO_3 is not related to properties of the interface of HOPG– MoO_3 , but it is a matter of measurement method.

We reference CPD measurement to a known work function, which allows calculation of WF (see Experimental Section 2.5). With reference to the HOPG WF, $\Phi_{HOPG} = 4.50 \pm 0.10$ eV (see UPS results in Figure 15b), it gives $\Phi_{MoO_3} = 4.80 \pm 0.10$ eV and agrees with the trend of WF reduction after air exposure presented by UPS (Figure 15b).

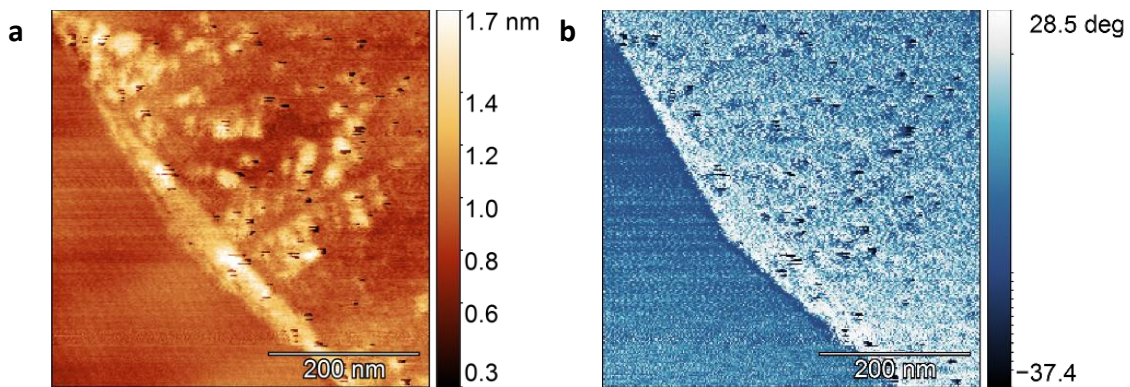


Figure 25: Surface perturbations on MoO_3 monolayer: semi-contact AFM in air. (a) topography image of HOPG/1L- MoO_3 . **(b)** the corresponding phase distribution map allows easily distinguish the perturbations from MoO_3 surface (where MoO_3 is lighter blue). The uncovered HOPG region is also distinguished from MoO_3 . Scan size: $(1 \times 1) \mu m^2$. Process parameters: pre-growth substrate UHV annealing (380 °C, 1.5 h), growth on the heated substrate (220 °C).

To magnify the air-induced impurities, we present the topography of an edge of MoO_3 island (Figure 25a). The corresponding phase distribution map is shown in Figure 25b, where a clear contrast between MoO_3 surface and HOPG can be recognised due to different interaction of both materials with AFM tip. In both images a clear perturbations can be observed in form of large protrusions and very small area dips. In particular, dips are related to strong point interaction between AFM tip apex and surface material and lead to characteristic dark spots on the topography image and disturbances of phase. The exact nature of both types of defects is unknown and may be related to the presence of some adsorbates at the structure defects, such as physisorbates or chemisorbates formed with oxygen, moisture [43,147], or other impurities because of exposure to the atmosphere. It is worth mentioning that one can notice similar

perturbations in AFM scans on MoO₃ and MoO₂ in other works [74,149–151], which were not discussed; thus, as a common feature, it may lead to crucial implications on properties such as work function and requires further investigation.

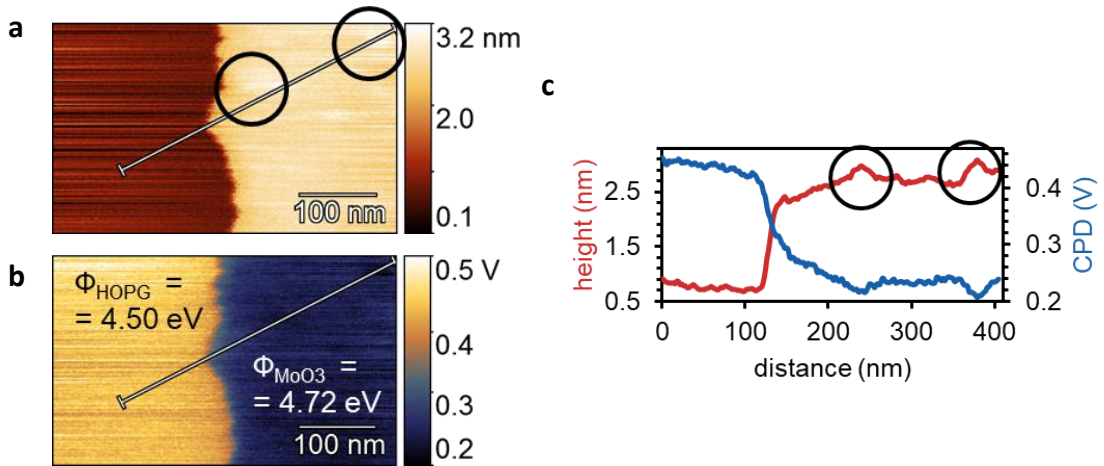


Figure 26. Local surface potential of MoO₃ monolayer on HOPG: KPFM measurement of perturbations in ambient. (a) smooth topography affected by perturbations – marked by black circles. **(b)** corresponding contact potential map. Yellow colour is attributed to large CPD signal (low work function), while blue colour corresponds to low CPD (higher work function). The perturbations are accompanied by changes in the CPD pointing towards higher work function. The extracted profiles (indicated by lines in (a) and (b); average of 10 px) are overlaid in **(c)**. Process parameters: pre-growth substrate UHV annealing (350 °C, 1 h), growth on the heated substrate (220 °C).

Next, we study CPD distribution over the topographic perturbations – see Figure 26. In the AFM topography image (Figure 26a), the smooth surface is affected by protrusions marked by black circles. These topographic protrusions are barely seen in the exact locations in the corresponding CPD map shown in Figure 26b, but are well resolved in cross-section profiles. Figure 26c shows overlaid profiles of height and CPD extracted along lines shown in Figure 26a-b using average of 10 px. The height of the topographic protrusions is roughly 0.3 nm, while CPD between protrusions and defect-free MoO₃ surface is $\Delta = 0.03$ V ($CPD_{HOPG} = 0.45$ V; $CPD_{MoO_3} = 0.23$ V).

On the other hand, air exposure does not degrade the 1L MoO₃ from STM perspective. While STM does not observe any aggregates on the surface (see Figure 14), scanning by AFM in semi-contact mode reveals a significant number of aggregates on the surface, and those structures affect the electronic properties of 1L MoO₃. Therefore, KPFM examination of molybdenum oxide in UHV is highly desired (see Section 5.2.2). Although recent studies shed some light on this issue, suggesting adsorption of hydrogen and wetting surface by water [150], it does not explain the nature of the surface aggregates observed in the experiment. It is also clear that observed in air value of WF is far lower than measured using UPS in vacuum, which

indicates crucial influence of aggregates on the electronic properties of MoO_3 . We encourage further investigations as this issue is out of the scope of this study. However, it is worth mentioning that those protrusions are more common for monolayers than the subsequent layers (they are not exclusive for monolayers; however, the density is significantly lower for the successive layers).

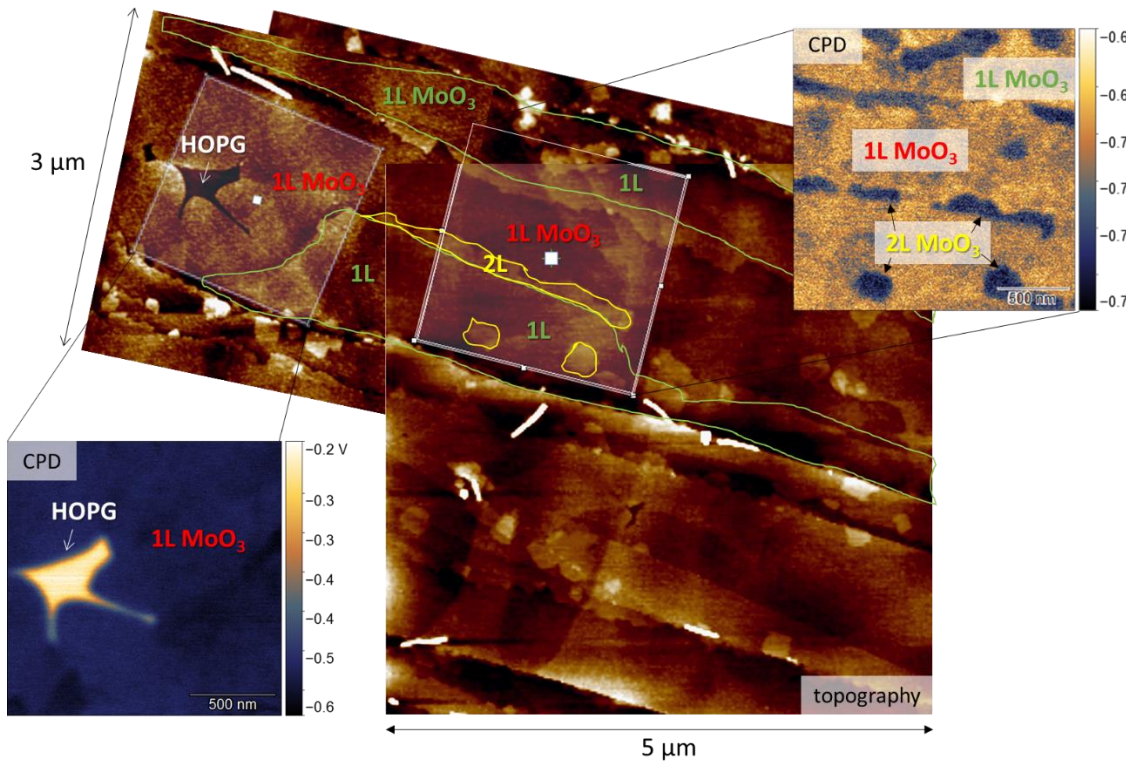


Figure 27: Topography and local surface potential of MoO_3 layers (1–2 L) on HOPG: KPFM measurement in ambient. The centre was imaged by AFM in semi-contact mode. The number of layers is indicated – different font colours are used for particular HOPG terraces. Process parameters: pre-growth substrate UHV annealing (350 °C, 2 h), growth on the heated substrate (220 °C).

As the literature reports claim that work function of MoO_3 increases with thickness (for amorphous growth), it is worth investigating also WF in function of a number of layers of crystalline α - MoO_3 . The previous results from Kim *et al.* [71] presented KPFM measurements of layered MoO_3 , did not show any WF variation from 2 to 7 layers in ambient conditions. In contrast, our investigations prove a relatively small but noticeable difference between 1L and 2L of MoO_3 . Note that a sharp tip and very low tip-surface distance are required to observe these differences (see Figure 24 where no CPD contrast was observed on 2L).

Figure 27 presents a wide AFM topography of MoO_3 nanosheets on HOPG. The majority of the coverage is built up by monolayer; however, minor 2 and at least 3 or more stacked layers can be found. The magnifications of topography regions show KPFM imaging: CPD signals

between 1L MoO₃-HOPG and 1L-2L MoO₃. There is clear CPD contrast between subsequent layers, although the intra-layer difference (1L-2L MoO₃) is low, approx. 0.03 V, while the difference between 1L MoO₃-HOPG is equal to 0.26 V. This shows that thicker MoO₃ film in air indeed increases the WF but the change of 1 layer is little.

Further investigation and understanding of the variation in WF with thickness of MoO₃ – showing for the first time the variation in WF with the number of layers of MoO₃ in ambient – could explain the reported thickness dependence (for thicker films) on graphene-like substrates. In accordance with local electronic structure study by STS in Section 3.2.3, we believe that the first MoO₃ layer on HOPG has local variations of electronic structure in contrast to subsequent layers. At this point, we state a hypothesis that the first layer of MoO₃ is more defective, which makes it more prompt to physisorption or chemisorption of foreign species, thus reducing WF in higher extent than for the subsequent layers. This explanation is supported by topographic perturbations observed on monolayers in much higher numbers than on subsequent layers. Nevertheless, it has to be kept in mind that measurements in ambient are known to make KPFM difficult to precisely assess CPD, and thus work function. The absolute surface potential is altered by moisture and atmospheric adsorbates as well as intrinsic limitations of KPFM [152–154].

5.2.2. Local Surface Potential on Monolayer MoO₃ & HOPG in UHV

Next, we performed *in-situ* KPFM measurements in UHV to minimise influence of the environment. For determination of actual properties of MoO₃, the UHV conditions are essential as air contaminants critically influence work function of 1L-MoO₃. The difference between work function value for bulk (6.9 eV [42,43]) and air-exposed monolayer (4.7 eV) is notable.

Figure 28a shows KPFM topography of a 1L MoO₃ nanosheet on HOPG, consisting of multiple domains. Note that MoO₃ nanosheet boundaries are affected by an nc-AFM artefact, lifting the edges to a height of around 10 nm. This artefact arose due to impossibility of compensation of electrostatic forces at the boundary of two materials with relatively high differences in CPD values – as it is in the presented case (see discussion below). Therefore, the AFM tip was repulsed at the boundary of two materials, i.e. where the tip apex interacts with HOPG and 1L MoO₃ [155]. Also, one can recognise that the 1L-MoO₃ nanosheet is divided by domain boundaries in this image. However, the smooth surface of MoO₃ is free from the protrusions observed in air.

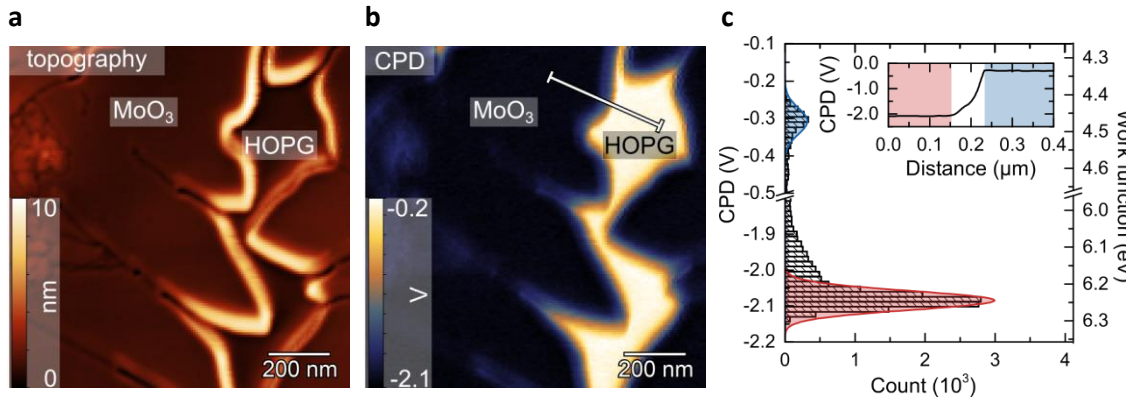


Figure 28: Local surface potential of MoO₃ monolayer (1L) on HOPG: KPFM measurement in UHV. (a) topography of HOPG/1L MoO₃, where 1L-MoO₃ edges are artificially lifted. **(b)** the corresponding CPD map. Yellow colour of CPD signal corresponds to a low WF (HOPG), whereas blue corresponds to higher WF (MoO₃). **(c)** CPD histogram extracted from (b). Shaded areas represent Gaussian fits for 1L MoO₃ (red) and HOPG (blue). The right axis indicate the work function obtained using the calibration on HOPG. Inset: line scan of the CPD signal corresponding to the line marked in (b) where rectangles highlight plateaus in CPD for: MoO₃ (red) and HOPG (blue). Scan size: (1 × 1) μm². Process parameters: pre-growth substrate UHV annealing (390 °C, 2 h), growth on the heated substrate (220 °C).

The corresponding CPD map (Figure 28b) presents a clear contrast between MoO₃ and the HOPG substrate. The yellow colour is attributed to high CPD signal, which corresponds to low WF values at the HOPG surface, while the blue colour indicates lower CPD and higher WF at the MoO₃ monolayer. To show CPD values over those materials, a line profile was taken over HOPG/1L-MoO₃ surface as indicated in the CPD map – the inset in Figure 28c exhibits two plateaus highlighted blue and red respectively. The CPD between the HOPG and 1L MoO₃ extracted from the profile is negative, which indicates that the MoO₃ work function is higher than HOPG WF.

Figure 28c presents a histogram extracted from the CPD map. Additionally, the scale on the right represents WF values (calibrated using WF of HOPG). Two Gaussian distributions fitted the data for quantitative evaluation. They allowed determination of mean CPD and full width at half maximum (FWHM) for MoO₃ and HOPG: $CPD_{MoO_3} = -2.10$ V and $CPD_{HOPG} = -0.30$ V, while FWHM for each material is 0.03 V. This gives the surface potential difference of $\Delta_{MoO_3/HOPG} = -1.80 \pm 0.05$ V. With the calibration to the known WF value of HOPG, $\Phi_{HOPG} = 4.50 \pm 0.10$ eV, the MoO₃ monolayer exhibits work function as high as $\Phi_{MoO_3} = 6.30 \pm 0.12$ eV. The observed WF for MoO₃ monolayer in UHV is significantly higher than the value measured in air (the difference is approx. 1.50 eV) indicating destructive character of contaminations.

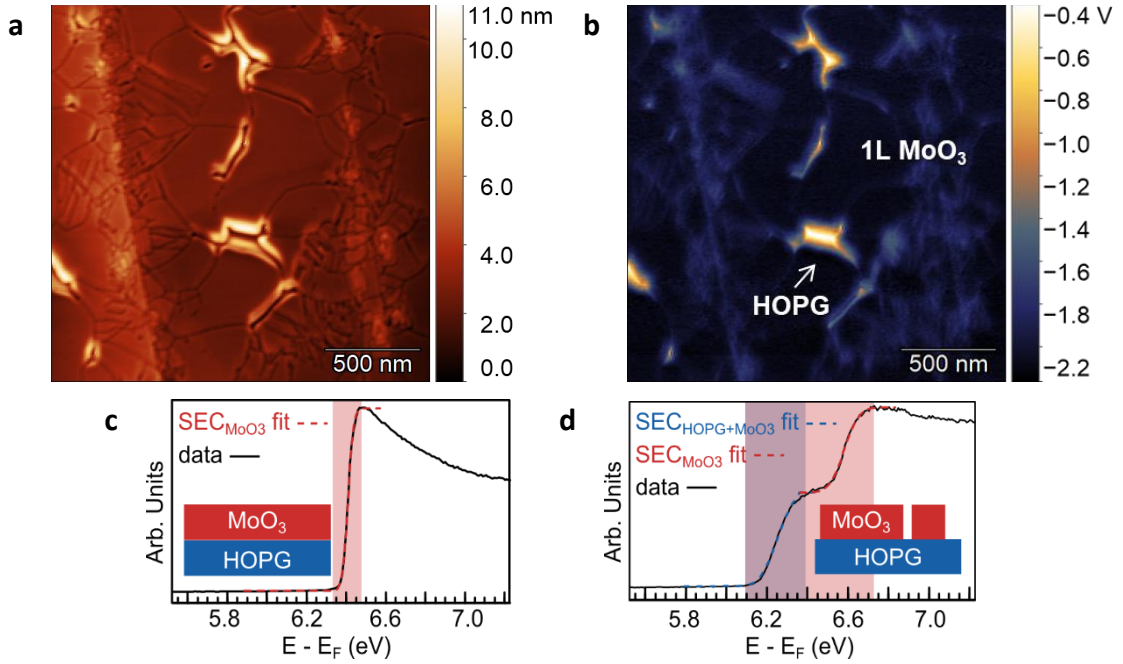


Figure 29: Work function of MoO₃ monolayer on HOPG. KPFM surface potential and UPS in UHV. (a) topography of 1L MoO₃ on HOPG. **(b)** the corresponding CPD map. Yellow colour of CPD signal corresponds to a low WF (HOPG), whereas blue corresponds to higher WF (MoO₃). Scan sizes: (2 × 2) μm². He I UPS spectra of secondary electron cut-off regions: **(c)** monolayer film of MoO₃. **(d)** partially covered HOPG with nanosheets of monolayer MoO₃. The coloured dashed curves indicate the fits of SECs; while the shaded areas highlight SEC widths. Insets: schematic illustrations of a HOPG/1L-MoO₃ sample coverage. Process parameters: pre-growth substrate UHV annealing (390 °C, 2 h), growth on the heated substrate (220 °C).

To confirm the local work function over wider area with a global technique, we use UPS, which requires sufficient MoO₃ coverage. Figure 29 shows KPFM measurements of almost coalesced 1L MoO₃ film satisfying the coverage requirement. While topography reveals mainly domain boundaries and artificially lifted edges of 1L MoO₃, the CPD map clearly shows minor holes to the substrate. Full coverage enables using the HOPG substrate as a direct reference. Thus, such a system requires additional measurements on a reference, e.g. another HOPG crystal, making it a disadvantage of KPFM. In such cases, UPS becomes useful for direct measurement of arbitrary WF value.

He I UPS spectrum in SEC region of a coalesced 1L-MoO₃ film is given in Figure 29c; for clarity, the inset illustrates the HOPG/MoO₃ coverage. The work function is determined from the intersection of linear extrapolation of an edge of SEC with the background [20,67], as it was described in Experimental Section 2.4. The x-axis of photoelectron energy is calibrated to Au(111) Fermi level, so the energy indicated by SEC corresponds to the WF. The WF of MoO₃ is determined as $\Phi_{\text{MoO}_3} = 6.40 \pm 0.10$ eV, in agreement with our UHV KPFM measurements.

It is worth noting that the shape of the SEC is a measure of uniformity of work function and surface cleanliness [33,34]. 1L MoO₃ film features a homogenous work function as the SEC

width, i.e., FWHM = 0.05 eV, as highlighted by shaded area in red (Figure 29c). Furthermore, the absence of any low kinetic energy tail (towards lower energies) indicates high surface cleanliness since air-derived contaminants are known to lower the work function of MoO₃ [67].

Interestingly, the UPS approach can also be applied for WF assessment of partially covered substrate by nanosheets of 1L MoO₃. A UPS spectrum from a sample of fractional coverage is given in Figure 29d. For clarity, the inset illustrates the HOPG/MoO₃ coverage. Providing sufficient coverage by MoO₃ nanosheets yet not complete within the probed area, the observed SEC consists of two edges. We assign the SEC edge at high energy 6.50 ± 0.15 eV (highlighted in red) to the MoO₃ monolayer only. The UPS spectrum of coalesced monolayer (Figure 29c) confirms that the high energy SEC accurately measures WF of 1L MoO₃. The other SEC edge observed at low energy at 6.15 ± 0.15 eV (highlighted in purple) corresponds to a complicated horizon of electrostatic potential distribution above the HOPG/MoO₃ surface, where photoelectrons emitted from HOPG (low WF) face an additional energy barrier created by MoO₃ (high WF). The explanation of double-edge SEC has been well described by Schultz *et al.* [119] – see also Experimental Section 2.4, including details on fitting distinct SEC.

The above example emphasises that UPS spectra for uncoalesced films are prone to misinterpretation of SEC and thus the work function of studied material.

Overall, the measured values of WF (~ 6.40 eV confirmed by KPFM and UPS) proved that it is possible to achieve the HOPG/1L-MoO₃ heterostructure, where the modification of initial WF is efficiently enhanced by deposition of a single monolayer. Here, the 4.50 eV of WF for graphene-like substrate was increased by nearly 2 eV, proving that crystallinity of deposited material and provided UHV environment are beneficial in excluding the need for thicker deposition of films.

5.2.3. Restoration of High Work Function of Air-Exposed MoO₃ Monolayers: Post-Processing by UHV Annealing

This Section describes a post-processing method applied to samples kept in UHV and samples that underwent air exposure in order to recover the high WF of MoO₃ films. We investigate the influence of annealing in UHV on work function, morphology, and chemical structure. To mimic possible transportation procedures and check effect of exposure duration, the samples are exposed to air for a few minutes or days.

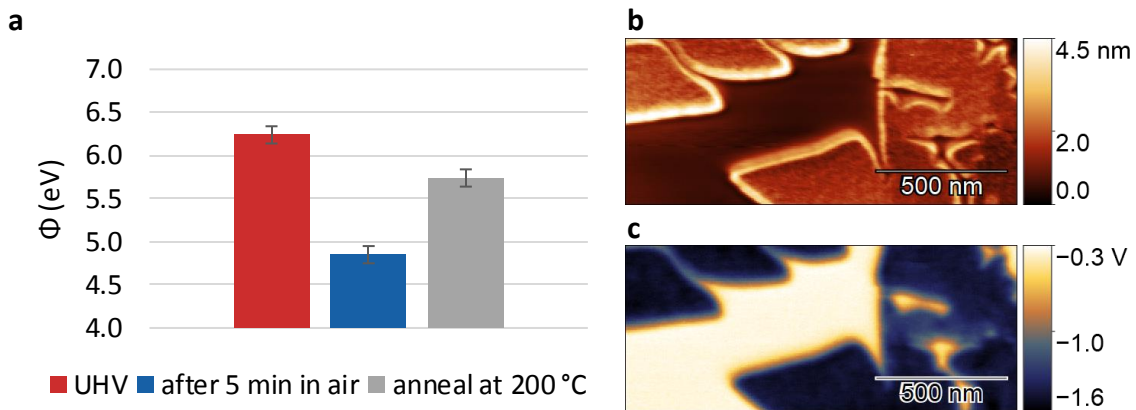


Figure 30: Work function evolution of 1L MoO₃ on HOPG: KPFM measurements in UHV. (a) column chart of work function Φ measured in UHV (red), after air exposure of 5 min (blue), and after annealing in UHV for 1 h at 200 °C (grey). Φ calculation was referenced to uncovered HOPG. UHV KPFM images taken after annealing in UHV (1 h, 200 °C) (b) topography and (c) corresponding CPD map. Yellow corresponds to low WF (HOPG), whereas blue corresponds to higher WF (MoO₃). Scan sizes: (1.5 × 0.7) μm². Process parameters: pre-growth substrate UHV annealing (380 °C, 2 h), growth on the heated substrate (220 °C).

First, we investigate work function evolution after controlled short exposure to air, which leads to a decrease in WF. For reference to the initial WF, we performed KPFM measurements in UHV on a HOPG/1L MoO₃ sample, where uncovered HOPG was used as known WF. Average CPD of HOPG/1L MoO₃ ($\Delta = 1.75$ V) was taken to calculate 1L MoO₃ work function – $\Phi_{MoO_3} = 6.25 \pm 0.10$ eV. Next, the HOPG/1L MoO₃ sample was exposed to air for 5 minutes and introduced back to UHV. The short exposure to air decreased the WF to 4.85 ± 0.10 eV in repeated KPFM measurements (average CPD between HOPG and MoO₃ is $\Delta = 0.35$ V, which agrees with previous results from air – Section 5.2.1). Finally, annealing at 200 °C for 1 h in UHV leads to WF increase to 5.75 eV ($\Delta = 1.25$ V), which gives 92% of the initial value. The column chart in Figure 30a depicts the evolution of WF in those three steps.

Simultaneously with CPD, we studied the morphology of the sample surface – after annealing, the surface of 1L MoO₃ appears rough with visible corrugations (see Figure 30b and compare with the initial smooth surface in Figure 28a). Despite clear roughness observed in topographic image (RMS on nanosheets is around 0.15 nm), the corresponding surface potential image in Figure 30c remains uniform without any local WF variations in a given spatial resolution. The origin of molybdenum oxide surface corrugation introduced during annealing in UHV remains unclear. More investigations are required to understand underlying physical phenomena. For example it may be explained by induced material degradation by higher density of oxygen vacancies or be related to mechanical stress during heating/cooling process, deforming the monolayers.

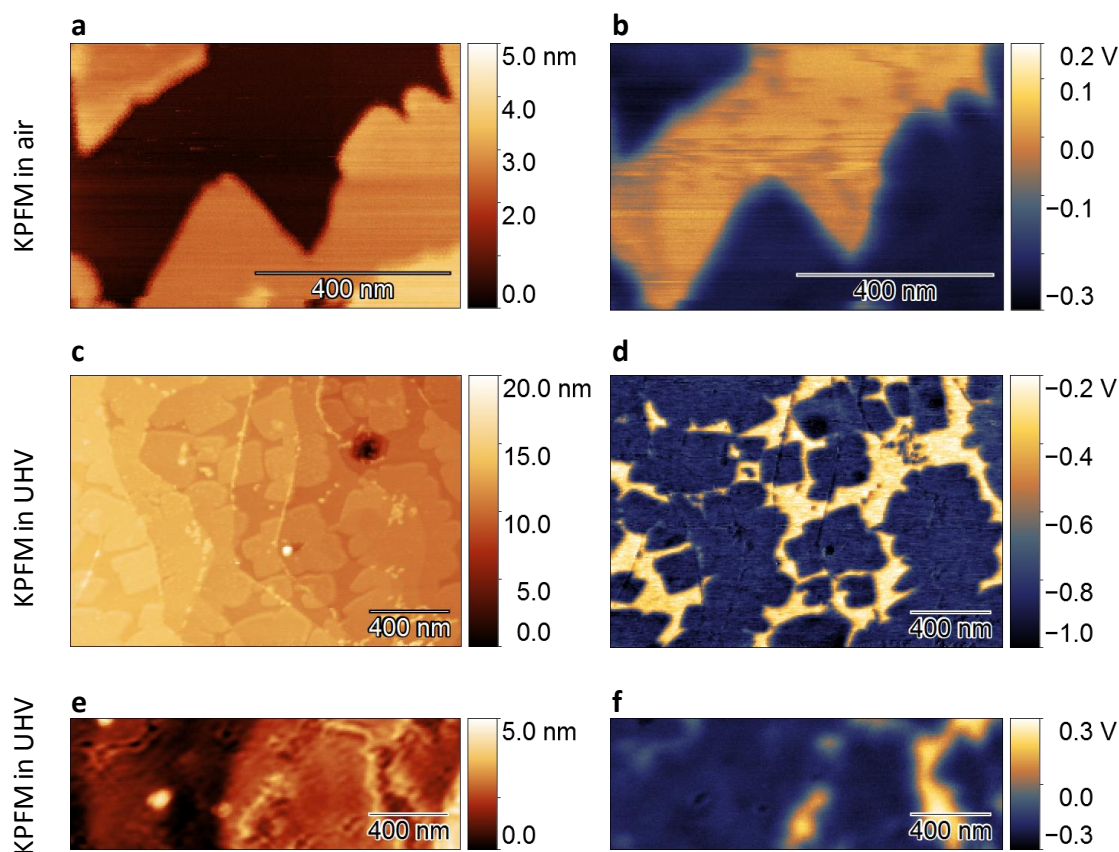


Figure 31: Work function evolution of 1L MoO₃ on graphene: KPFM measurements. Sequence of KPFM images: topography and corresponding CPD map. Yellow corresponds to low WF (graphene), whereas blue corresponds to higher WF (MoO₃). **(a-b)** taken in air. **(c-d)** taken in UHV after annealing (1 h, 100 °C). **(e-f)** taken after annealing in UHV (1 h, 100 °C). Process parameters: pre-growth substrate UHV annealing (440 °C, 3 h), growth on the heated substrate (250 °C).

The second case to be investigated is prolonged, few-day air exposure. The starting point is a sample of MoO₃ grown on FL-graphene taken to air after the growth. It was immediately taken to AFM for imaging (in air) – see Figure 31a-b. The topography shows the smooth surface of MoO₃ nanosheets (RMS = 0.25 nm, Figure 31a). The corresponding CPD map is disturbed by changing tip (Figure 31b) – note some horizontal lines at a different voltage (also visible at the topography image). Nevertheless, the contact potential difference between graphene and MoO₃ remains constant and equal to 0.23 V, consistent with previous results on HOPG.

Next, after prolonged air exposure of a few days, we introduced the sample into UHV, annealed the sample at 100 °C for 1 h, and repeated KPFM measurements – see Figure 31c-d. The annealing temperature was set lower than for the previously discussed HOPG/MoO₃ sample in attempt to avoid roughening the surface of MoO₃ nanosheets. AFM topography image recorded on the sample prepared in a such way is shown in Figure 31c. Unfortunately, the reduced annealing temperature also caused changes of the film morphology as before. The

changes seem to occur in smaller extend, i.e. the measured RMS is equal to 0.27 nm while for sample annealed at 200 °C RMS was 0.15 nm.

In Figure 31d CPD map of annealed graphene/MoO₃ sample is shown. Clearly, the gentle annealing led to higher surface potential difference between graphene and MoO₃ if compared to air exposed sample. The CPD difference estimated from Figure 31d is 0.55 V which is by 0.32 V more than before annealing. Such increase of the CPD difference after gentle annealing indicate that the WF of 2D MoO₃ on graphene can reach around 5 eV. Note, that for HOPG/MoO₃ sample annealed at 200 °C the final WF is even larger therefore, we decided to anneal the graphene/MoO₃ sample again.

The results after the second UHV annealing in the same conditions (100 °C, 1 h) can be seen in Figure 31e-f. Clearly, the second annealing resulted in further increase of film roughness reaching RMS = 0.67 nm (see the topography image shown in Figure 31e). Moreover, the corresponding CPD map does not satisfy expectations for further recovery of WF value due to yielding contact potential difference at the same level ($\Delta = 0.50$ V). This leads to the conclusions that prolonged air exposure may hinder the WF recovery, and efficient restoration of high WF value can only be achieved at the cost of deformation of the layer morphology as the nanoscale structural evolution was previously observed at the MoO₃ crystal surface at elevated temperatures [156].

With the two above examples, we continue to study the WF evolution of UHV annealed and air-exposed 1L MoO₃ using UPS. To monitor changes in WF, we tested samples in two variants. As a reference, we gradually annealed a HOPG/1L-MoO₃ sample in temperatures between 100 and 325 °C for 2 h each step, while this sample was kept in UHV without any exposure. As a test sample, we exposed a HOPG/1L-MoO₃ sample for a few days and introduced it back into the UHV chamber, where it was similarly annealed.

In Figure 32, the WF of 1L MoO₃ films is presented as a function of increasing UHV annealing temperature from room temperature (RT) to 325 °C. The initial value of WF of 1L MoO₃ in UHV was measured to be 6.40 ± 0.10 eV. The reference sample (data points marked by blue dots) gradually annealed shows little increase in the WF up to 6.50 ± 0.10 eV.

The situation is completely different for test sample (data points marked by blue stars). The initial WF is reduced to 4.70 eV (see arrow pointing down at RT), which is consistent with previously discussed results. Next, the sample was gradually annealed in UHV. At 100, 150, 200, and 270 °C temperatures, the WF were measured to be 5.05, 5.30, 5.45 and 5.46 eV, respectively. With a further increase in annealing temperature, we expect no further changes in WF, as the saturation in WF recovery was reached around the annealing temperature of

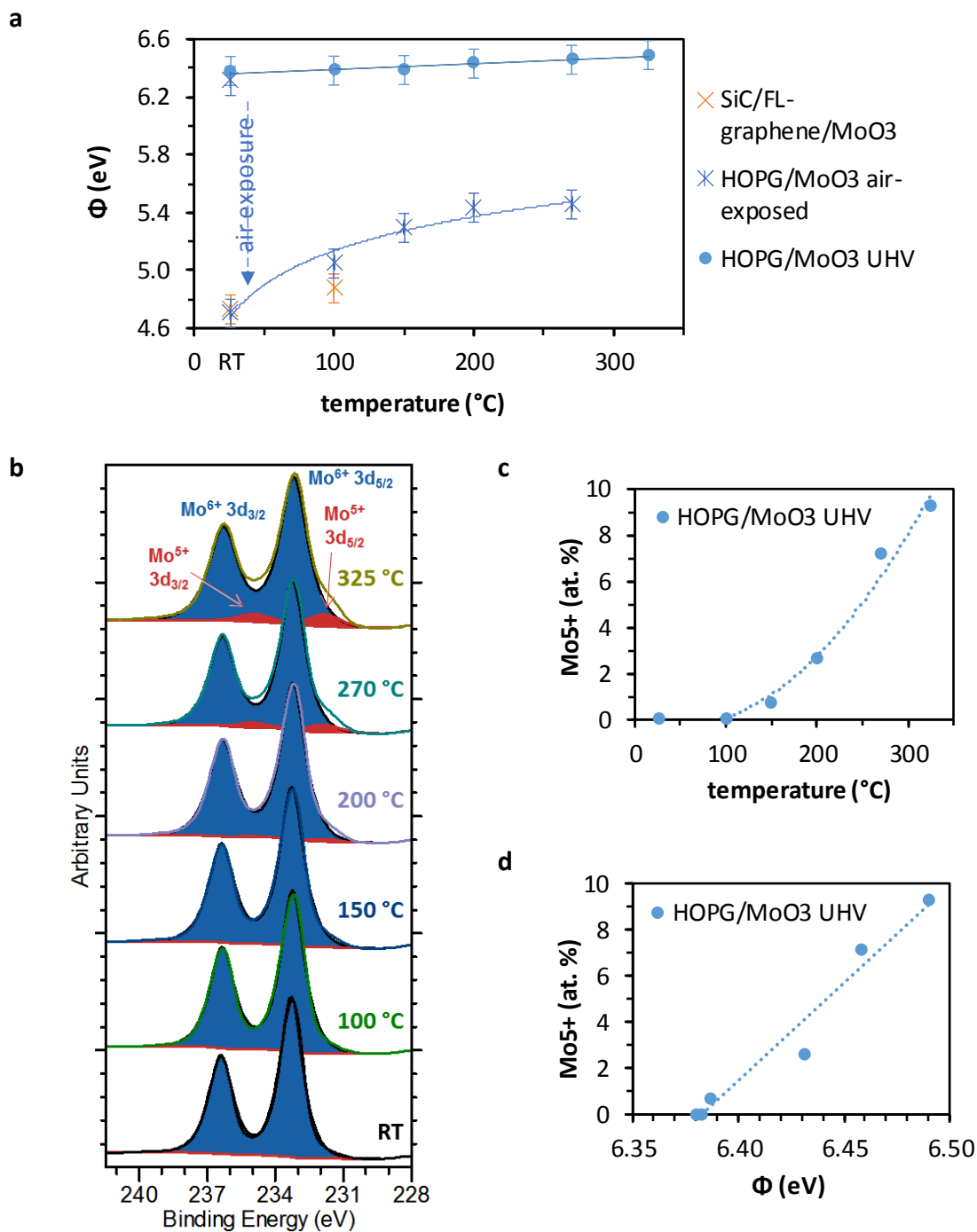


Figure 32: Sequence of annealing: UPS and XPS measurements. (a) Work function of evaporated MoO₃ films versus annealing temperature: HOPG/MoO₃ kept in UHV, along with air exposed heterostructures graphene/MoO₃ and HOPG/MoO₃. Chemical structure HOPG/MoO₃ kept in UHV: (b) Mo3d XPS spectra at exit angle of 60° to the surface normal; experimental data and fitting with a two-component Gaussian-Lorentzian shaded profiles corresponding to Mo⁶⁺ (blue) and Mo⁵⁺ (red). The Mo oxidation states and annealing temperatures are indicated. (c-d) atomic concentrations of Mo⁵⁺ versus annealing temperature and work function, respectively.

270 °C. The saturation is in line with previous results of annealing thick evaporated MoO₃ films [148]. Clearly, the WF recovery suggests removal of impurities from the surface. However, our experiments show also that the surface morphology changes in consequence of sample annealing, thus, there might be some concurrent processes leading to increase of WF coexisting with removal of impurities.

The overall WF recovery at the final annealing reaches 85% of the initial value, which is lower than that achieved after short air exposure, further confirming the conclusion that prolonged exposure may hinder WF recovery. Incomplete recovery suggests that some impurities remained on the surface, which is difficult to remove with the annealing. In addition, we added to the plot two data points (marked by orange crosses) from the above described FL-graphene/MoO₃, which agree with the trend of the WF recovery upon annealing.

To monitor the corresponding chemical evolution of coalesced 1L MoO₃ film (without air exposure) over annealing, we performed XPS measurements at 60° grazing electron exit angle with respect to the surface normal increasing the surface sensitivity. Figure 32b shows the Mo3d photoemission spectra along with peak fits and assignments at increasing UHV annealing temperature. The spectra were fitted with two double components corresponding to Mo⁶⁺ (3d_{5/2} at binding energy (BE) of 233.2 eV) and Mo⁵⁺ (3d_{5/2} at BE of 231.8 eV) [19,43,65,69,71,79]. For details of the fitting curve parameters, see Experimental Section 2.3. The Mo3d region shows no indication of the presence of Mo⁴⁺ (3d_{5/2} typically observed at 229.4 eV [41,43,65,71,79]), however, it cannot be entirely excluded within the given resolution.

During annealing in UHV, 1L MoO₃ becomes reduced, giving rise to one oxidation state, Mo⁵⁺ – see increasing area of red peaks with increasing annealing temperature. For quantitative analysis, Figure 32c plots atomic concentration on Mo⁵⁺ in function of annealing temperature. The plot reveals a positive trend (see dash line) representing the behaviour of reduction of 1L MoO₃. After combining UPS and XPS data, we arrived at Figure 32d plots atomic concentration on Mo⁵⁺ in function of WF. This plot similarly reveals a positive trend of increase in WF along with further reduction of the oxide and introduction of defects to the initial chemical structure. This observation is contrary to previously reported results of decrease in WF at deviating from stoichiometric MoO₃ [148]. On the other hand, the observed WF changes are minor and are close to the experimental error. As previous results were obtained on different thicknesses of the layers a direct comparison is impossible. However, our results suggest that introducing defects (defect engineering) may pave the way to precise WF tuning of 1L-MoO₃ heterostructures as suggested for bulk MoO₃ and related annealing changes [59,65].

5.3. Conclusions

In this Chapter a performed comprehensive study of work function of 1L MoO₃ was described. To sum up, we answer to questions asked at the beginning of the Chapter grouped by three topics.

- I. The first Section described how work function is reduced by air exposure on the local scale by KPFM.
 - 1L MoO₃ after contact with air exhibited the WF of 4.80 ± 0.10 eV, which is significantly lower than the predicted theoretical value. Our findings highlighted the need for a controlled environment to maintain access to the high WF of MoO₃.
 - Topographical protrusions were observed on the MoO₃ surface exposed to air with a notable higher density on 1L than 2L.
 - 2L MoO₃ exhibited higher WF by 0.03 V than 1L that is close to the resolution limit but suggests the dependence, which has not been reported yet. The observed difference may be related to properties of electronic structure or the concentration of surface defects. This observation is consistent with the results of STS that were described in previous Chapter 3.
- II. The second Section elucidated WF of MoO₃ monolayer in UHV, emphasising its potential as an effective buffer layer for relevant applications in organic electronics.
 - We determined experimentally that 1L MoO₃ boosts the work function of the graphite-based heterostructures to high values according to KPFM 6.30 ± 0.12 eV, which agrees with UPS-derived 6.40 ± 0.10 eV.
 - So high efficiency of WF tuning with MoO₃ has never been reported before for crystalline coverages with thicknesses below 1 nm.
 - Therefore, we proved that the controlled environment, unbroken UHV conditions for both growth and characterisation, was the critical factor in observing and further applying the high work function of 1L MoO₃.
- III. The third Section describes an attempt to restore high WF values of MoO₃ monolayers on graphene and HOPG.
 - After 5 min exposure, the material lost its initially high WF, but UHV annealing at 200 °C led to WF recovery of 1.25 eV to 5.75 eV, which gives 92% of the initial value of 6.25 eV.

- After a few days of exposure, UHV annealing at 200 °C led to WF recovery of 0.75 eV to 5.45 eV, which gives 85% of the initial value of 6.40 eV. WF saturation was observed for annealing temperatures at 200–270 °C. The recovery after prolonged exposure was poorer than for short air exposure. This suggested that the material degradation process occurred, which could not be reversed by simple UHV annealing.
- Annealing in UHV induced roughening of the 1L MoO₃ film. This process remains unclear. However, could be both related to material degradation or with mechanical stress during heating/cooling process, which is able to deform monolayers.
- We monitored the chemical changes as a function of annealing temperature. While the gradual reduction of films was observed, it was accompanied by WF. The changes are relatively small and are close to experimental error but may show the way of precise WF tailoring.

For a clear view of the above WF data, we gathered them in Table 2 with relevant available WF values in the literature, including a method of obtaining the data. Note that KPFM data from UHV is taken exclusively from this work as it is not available in the literature. It is worth comparing the data with the experimental literature WF value of $\Phi_{\text{lit},\text{MoO}_3} = 6.90$ eV for bulk α -MoO₃ [19,38,42,43].

Material	Sample	WF (eV)	Method	Reference
MoO ₃	1L MoO ₃ (010) on HOPG(0001)	6.30 ± 0.12	KPFM in UHV	this work
	1L MoO ₃ (010) on HOPG(0001)	6.40 ± 0.10	He I UPS	this work
	amorphous MoO _{2.86} of nominal thickness of 1.4 nm on 1L graphene on Cu	5.92	He I UPS	[6]
	2 nm coalesced film of reduced MoO _x on transferred 1L graphene on Si/SiO ₂	6.42	He I UPS	[19]
	bulk MoO ₃	6.90	He I UPS	[19,38,42,43]
	air-exposed bulk MoO ₃	5.20	He I UPS	[42,43]
	air-exposed 1L MoO ₃ (010) on HOPG(0001)	4.70 ± 0.10 4.80 ± 0.10	He I UPS KPFM in air	this work this work
	5-min air-exposed 1L MoO ₃ (010) on HOPG(0001) and annealed (200 °C)	5.75	KPFM in UHV	this work
	air-exposed 1L MoO ₃ (010) on HOPG(0001) and annealed (200 °C)	5.45	He I UPS	this work
	HOPG	UHV-cleaved HOPG(0001)	4.50 ± 0.10	He I UPS
graphene	2L graphene on SiC(0001)	4.50	He I UPS	this work
	UHV-annealed (350 °C) 2L graphene on SiC(0001)	4.19	He I UPS	this work

Table 2: Summary of the obtained results and the literature values of MoO₃ and HOPG/graphene work functions.

6. Graphene Heterostructures with Rhenium Oxide

In the previous Chapters, we provided examples of successful work function (WF) tuning of graphene heterostructures with MoO_3 , which belongs to the target group of transition metal oxides (TMOs). However, to be compatible with organic components in electronics with inverted structures, low-temperature evaporable materials are highly desirable. Similarly to the case of graphene/ MoO_3 heterostructures, energy alignment between graphene and organic layers can be achieved by modifying the electronic properties by depositing a layer of another TMO – rhenium heptoxide (Re_2O_7). Re_2O_7 has the lowest melting temperature among TMOs [89].

Therefore, exploring Re_2O_7 potential in the role of WF modifying layer is a prerequisite for further realising graphene-based anodes, which have not yet been much studied [89]. This mainly concerns the modification of graphene heterostructures with rhenium oxides. Furthermore, to guarantee the high quality of both heterostructure components, no structural defects should be developed in graphene during the TMO growth process. Due to the lack of such information on graphene/ Re_2O_7 we assess this topic.

Some of the results discussed in this Chapter have already been reported in the article entitled '*Work Function Tunability of Graphene with Thermally Evaporated Rhenium Heptoxide for Transparent Electrode Applications*', which was published in *Advanced Engineering Materials* on November 20, 2019 [20]. The Raman measurements were performed by Paweł Ciepielewski. The author acknowledges the contribution.

The topic undertaken in **this Chapter is aimed at deposition Re_2O_7 and investigation of the physical and chemical mechanisms occurring in graphene heterostructures with Re_2O_7 .** With such a motivation, the studies were carried out on the layers of Re_2O_7 thermally deposited on graphene grown by chemical vapour deposition (CVD) on silicon carbide crystals by several characterisation techniques: X-ray photoelectron spectroscopy (XPS), atomic force microscopy (AFM), Raman spectroscopy, scanning tunnelling microscope (STM), and ultraviolet photoelectron spectroscopy (UPS).

The following list describes the highlights of this Chapter:

- I. Chemical properties of rhenium oxide structures, including dependence on nominal thickness, i.e., duration of deposition.
- II. Morphology of rhenium oxide structures deposited on graphene by thermal evaporation in UHV, including a test of the potential damage of graphene during deposition.

- III. Test of mobility of obtained structures on the graphene surface – challenging STM characterisation.
- IV. Tuning the work function of obtained heterostructures by controlled deposition of Re oxide species.

6.1. Introduction

The literature provides examples of successful work function tuning of graphene heterostructures by MoO_3 [6,19]. This agrees with our results from the previous Chapters with MoO_3 . Expanding the TMO family in terms of studying candidates with low evaporating temperatures may be useful for compatibility with low melting-point organic materials. This turns our attention toward rhenium oxides. In this group, we can find ReO_3 with a melting point of $340\text{ }^\circ\text{C}$ [26] and Re_2O_7 , which starts to melt at temperatures as low as $225\text{ }^\circ\text{C}$ [89]. To broaden the potential WF enhancement candidates from the target group of TMOs, we selected Re_2O_7 with the highest valence state of rhenium.

Up to now, TMOs with low evaporating temperature were reported by Leem *et al.* [26], who doped ReO_3 into a hole transporting layer in organic light-emitting diode (OLED). The second example is the work by Jia *et al.* [89], who doped Re_2O_7 into a hole transporting layer in OLED, where higher stability was reported for Re_2O_7 -doped layers than ReO_3 in air.

In the literature, there are not many reports on rhenium oxides on the graphene surface. Miramontes *et al.* [157] reported on ultra-small rhenium clusters supported on graphene. Despite not discussing rhenium oxides, it is worth noting that octahedral and tetrahedral Re structures worked as seeds to create more complex morphologies. Interestingly, they claim that a higher catalytic effect could be expected in adsorbed clusters on graphene than when clusters are isolated. For other works in the literature considering Re and graphene, see for example: computations on Re–Pt clusters on monovacancy sites in graphene [158]; or graphene directly grown on a superconducting $\text{Re}(0001)$ thin film, where the superconducting behaviour was studied [159]; or, in reverse, Re deposited on graphene, where no intercalation or chemical reaction was observed even after annealing [143]. Regarding local electronic structure measurements, attempts of STS studies have been taken on bulk ReO_3 [160] and metallic ReO_3 nanoparticles on HOPG of sizes between 4–10 nm, where resistance increased with decrease in particle size [145].

For designing heterostructures, it may be advantageous if a material contacting graphene does not form carbide, thus, rhenium can be a good candidate [143]. However, rhenium oxide species can intercalate graphite [161,162]. In particular, Fröba *et al.* [161]

investigated the electronic structure and the medium-range order of Re_2O_7 graphite intercalation compounds by X-ray absorption near edge structure (XANES), revealing a charge transfer from graphite to rhenium.

From this Thesis perspective, the most prominent study of Re oxides work function was undertaken by Baikie *et al.* [28] on strongly temperature-dependent WF of oxidised surface using UHV scanning Kelvin probe. They presented that oxidation substantially increases the WF of Re from clean 5.1 eV at room temperature (RT) to as high as 7.1 eV at around 525 °C [28]. This suggests that Re_2O_7 may become an effective WF enhancement for graphene.

6.2. Results and Discussion

6.2.1. Chemical Structure: XPS Characterisation

We start with XPS studies in order to determine the oxidation states of Re on the obtained graphene/rhenium oxide heterostructures.

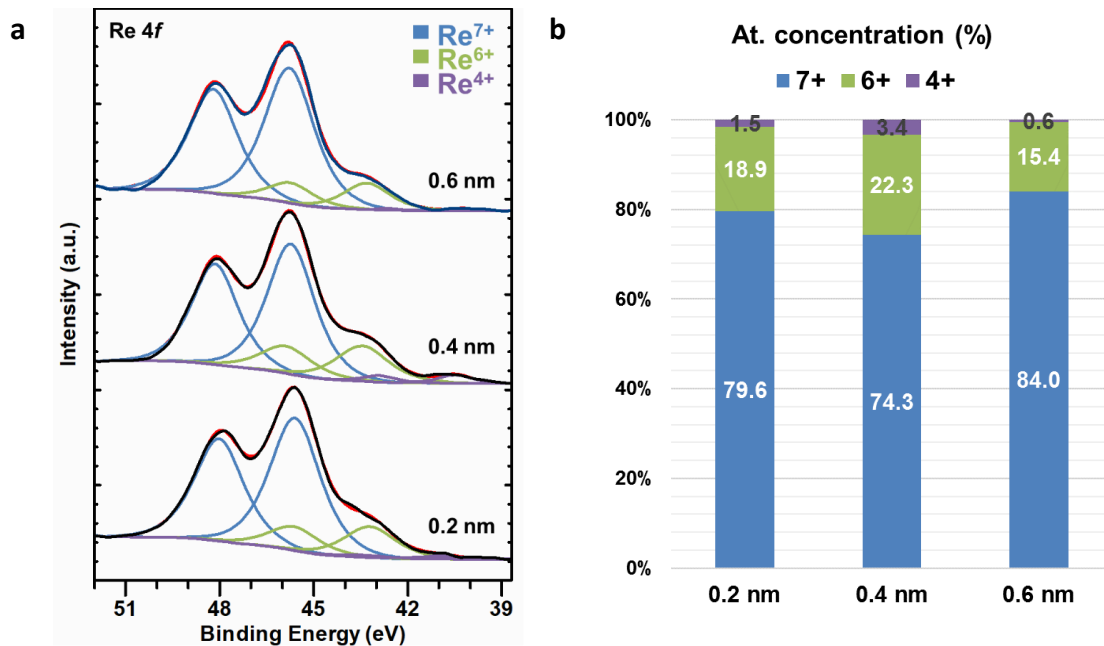


Figure 33: Chemical structure of deposited rhenium oxide on graphene. (a) XPS spectra in Re4f region with increasing nominal thicknesses. The Re oxidation states are indicated in the legends. The red line represents the raw data, while the black line represents the sum of all synthetic peak fits. **(b)** extracted atomic concentrations of Re oxidation states. Processes parameters: pre-growth substrate UHV annealing (300–330 °C, 1 h), growth on substrate at RT.

For all investigations described below the ReO_3 powder was used as an initial material for evaporation processes. As mentioned in Introductory Section 1.3.3, the chemistry of rhenium

oxides is complicated. The vapour composition during deposition process in UHV may vary from pure Re_2O_7 to mixtures of $\text{Re}_2\text{O}_7/\text{ReO}_3$, $\text{Re}_2\text{O}_7/\text{Re}$, or $\text{Re}_2\text{O}_7/\text{ReO}_3/\text{Re}$ [89]. Even though the temperature of the effusion cell was controlled to form only Re_2O_7 , namely, the temperature was kept below ReO_3 melting point, we cannot exclude the presence of other oxide mixtures by default – see Experimental Section 2.2.3 for details.

Figure 33a shows XPS spectra of the Re4f core-level region for graphene covered with rhenium oxide in the function of a nominal thickness (i.e. thickness according to measured deposition rate). A description of the peak fitting is given in Experimental Section 2.3. The $4f_{7/2}$ and $4f_{5/2}$ spin-orbit doublet peaks of the predominant Re^{7+} are found at binding energies of about 45.6 and 48.0 eV, respectively. The Re^{6+} oxidation state with $4f_{7/2}$ and $4f_{5/2}$ spin-orbit doublet peaks is found at binding energies of about 43.1 and 45.6 eV, respectively. These binding energies agree with the reference work by Greiner *et al.* [88], who performed comprehensive studies of rhenium oxides identification. The XPS spectra, along with peak fits, indicate that deposited films mainly consist of two oxidation states of Re. These are, respectively – relative to the atomic percentage – 7+, 6+ and a small amount of 4+. When comparing the three given spectra, there is no significant change seen with the increase of the deposited amount of the oxide material.

To quantitatively analyse changes in the function of nominal thickness, Figure 33b shows a plot of atomic concentrations of Re^{7+} , Re^{6+} , and Re^{4+} extracted from the XPS spectra. The three deposited layers predominantly consist of Re_2O_7 phase (represented by the presence of Re^{7+}) in an average 80% of atomic concentration, which is the most stable thermodynamically phase of rhenium oxides [21]. The rest, in average 19%, corresponds to Re^{6+} , while a non-negligible 1% corresponds to the lower oxidation state, Re^{4+} . The observed Re^{6+} may be described as a presence of ReO_3 component in the obtained material, however, as it has minor concentration we should rather relate it to the (sub stoichiometric) defects in the obtained Re_2O_7 system. It should be noted, however, that the non-stoichiometry of our material is relatively high.

Comparable contents of individual oxidation states of Re testify to the repeatability of the deposition process and the independence of the chemical structure from the size or number of deposited nanoparticles, as the morphology is presented in the following Sections.

6.2.2. Thermally Evaporated Re_2O_7 Nanoparticles on Graphene

To check the surface morphology of graphene synthesised on 6H-SiC(0001) covered with thermally evaporated Re_2O_7 , we have performed AFM investigations in semi-contact mode in ambient conditions.

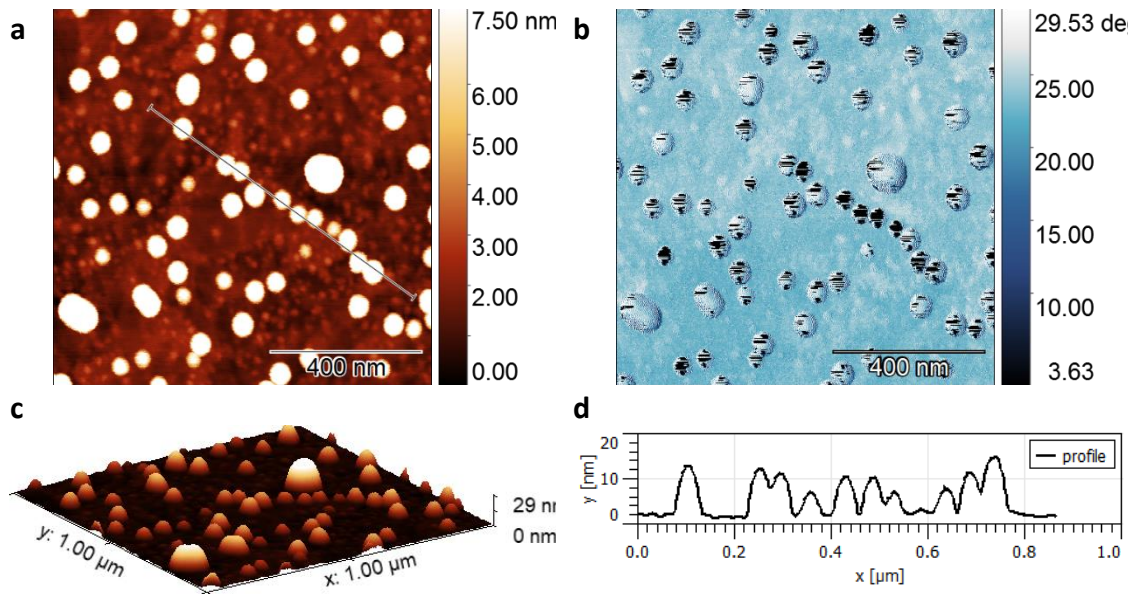


Figure 34: Typical appearance of Re_2O_7 nanoparticles produced by thermal evaporation in UHV on graphene on SiC: AFM micrographs in ambient. Semi-contact topography in (a), together with corresponding phase in (b), which highlights Re_2O_7 deposited structures. Scan size: $(1 \times 1) \mu\text{m}^2$. Roughness: (a) RMS = 3.5 nm. (c) AFM topography from (a) visualised in 3D highlighting size and height distribution of particles. (d) height profile taken along the line marked in (a) and averaged over 10 px, showing representative height variations of particles. Process parameters: pre-growth substrate UHV annealing (330 °C, 1 h), growth on substrate at RT.

A surface of representative graphene/ Re_2O_7 heterostructure is shown in Figure 34 (the preparation of the samples is discussed in Experimental Section 2.2.3). In the topography image (Figure 34a), Re_2O_7 nanoparticles are evenly distributed across the graphene surface and tend also to decorate the edges or defects; in the phase image (Figure 34b), the lack of vivid contrast may suggest full coverage of the graphene surface by Re_2O_7 . However, note that the dark spots in the phase image are related to strong point interaction between the AFM tip apex and the surface of high nanoparticles, leading to characteristic phase disturbances only at those spots and not in between.

The Re_2O_7 nanoparticles vary in size, which is presented in 3D visualisation in Figure 34c. Figure 34d shows the height profile, measured along the line marked in the topography image (Figure 34a) and averaged over 10 neighbouring pixels. The nanoparticles have an average height of 12 nm and a diameter of 40 nm with significant size distribution (note that the diameter measurement value may be affected by the shape of the scanning tip). The area in between the relatively big nanoparticles seem to be flat, which may indicate that the graphene has not been entirely covered by Re_2O_7 . This is further discussed in Section 6.2.3.

In all our experiments, we observed that the deposition of films of Re_2O_7 is problematic in obtaining full coverage on the graphene substrates. Our method does not lead to formation

of a homogenous layer on chosen type of graphene synthesised on SiC. It may be explained by the used temperatures and the oxide tendency to evaporate both at low temperatures and in UHV conditions, which in our case may lead to re-evaporation of the deposited material. The film of Re_2O_7 was found to sublime at a very low temperature of around $150\text{ }^\circ\text{C}$ [88], which is lower than was previously reported for bulk Re_2O_7 [163]. Another possible explanation is the influence of moisture in the ambient condition, to which the material was exposed between evaporation and the characterisation process. Re_2O_7 is highly hygroscopic [90] and decomposes into perrhenic acid (HReO_4) [164], suggesting that dewetting process may occur and form nanoparticles in air. In both scenarios, we may conclude low adhesion to the substrate, which is a strong factor hindering any coalescence.

From a technical point of view, in our experience AFM scanning on Re_2O_7 nanoparticles on graphene is difficult due to the high mobility of oxide nanoparticles caused by low adhesion to the graphene surface. Little oxide coverage is nearly impossible to catch on scans. Only at higher nominal coverage and with very low interaction between AFM tip and nanoparticles, it is feasible to visualise the surface morphology. More on high mobility of Re_2O_7 particles will be discussed in Section 6.2.3.

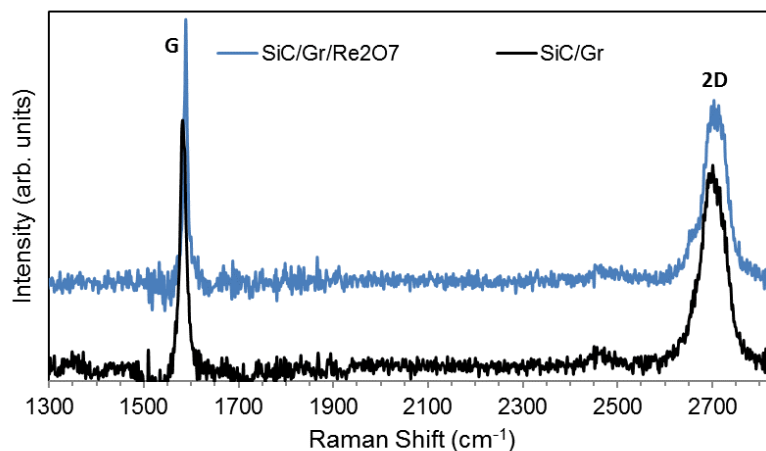


Figure 35: Raman spectra for the vibrational modes of graphene. Spectra recorded on pristine bilayer graphene (black) and graphene/ Re_2O_7 heterostructure with 2 nm of nominal oxide thickness (blue).

In order to test the potential structural damage of graphene during the evaporation process of Re_2O_7 , we used the Raman spectroscopy technique, which is a non-destructive and powerful tool to determine the quality of the graphene and the number of graphene layers [165]. Figure 35 shows the Raman spectra of pristine graphene before Re_2O_7 evaporation (black spectrum) and after the oxide deposition (blue spectrum).

Obtained Raman spectrum show typical features of the graphene, which exhibits two strong peaks at 1583 cm^{-1} and at 2700 cm^{-1} , corresponding to G- and 2D-modes, respectively [165]. The intensity ratio of the 2D to G peak of 0.9 and the FWHM of 2D band of 57 cm^{-1} agree with the literature values for graphene [165]. The high crystalline quality of used graphene is proven by barely seen D peak at 1350 cm^{-1} , whose mode is activated by structural defects.

After deposition of Re_2O_7 film, the Raman spectrum (top in Figure 35) is very similar to pristine graphene, where the two vibrational modes associated with graphene are unchanged. The lack of the D peak at about 1350 cm^{-1} indicates a non-destructive evaporation process onto graphene, during which additional defects in the structure of graphene were barely developed.

6.2.3. Re_2O_7 Nanoparticles Misplacement by STM/AFM Tips on Graphene Surface

As mentioned in the previous Section, thermally evaporated Re_2O_7 nanoparticles are highly mobile on graphene. While for little coverage, even semi-contact mode does not allow morphological characterisation, for high enough coverage or for nanoparticles big enough, that mode can provide morphological information. Nevertheless, if we try to investigate the electronic properties on the nanoscale, it turns out that it is highly challenging. The Re_2O_7 nanoparticles formed on the surface of graphene are easily misplaced by tips of both STM and AFM in contact mode. Tip acts as a broom sweeping the particles from the scan area. The interfacial adhesion is too weak to enable STM and AFM-contact imaging.

Exhaustive STM imaging of Re_2O_7 nanoparticles on graphene substrates, performed in ambient conditions at various combinations of bias voltage and tunnelling current, showed migratory species across the substrate surface (see Figure 36a–b). Images in Figure 36a–b were acquired by the use of Au tip at 4 V and 0.1 nA and show spikes of moving species, which is particularly vivid in the top parts of the images. Imaging trials were made with hand-cut Pt–Ir (70%–30%) and Au tips as well as etched W tips. We did not attain imaging conditions for any particular value of working parameters (for biases in the range of -5 – 5 V), as reported earlier for ReO_3 nanocrystals on HOPG [145].

However, following the STM scanning, semi-contact mode AFM images were obtained in the exact locations of STM scans and are shown in Figure 36c–d. The tilted squares in the images are areas of STM scans. The topography image (Figure 36c) clearly shows the frames of the prior STM scans, where the material accumulated. The phase image (Figure 36d) highlights

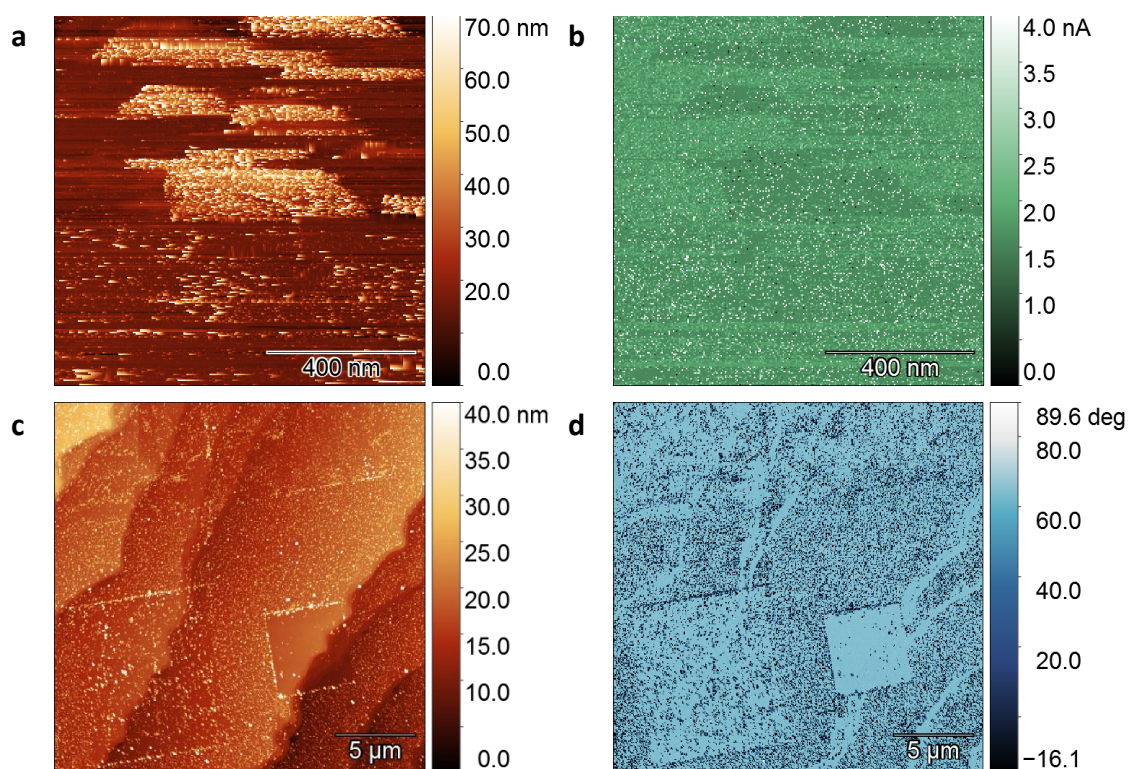


Figure 36: Re_2O_7 nanoparticles misplacement by STM tip on graphene: STM and AFM micrographs. STM topography in (a), together with current in (b). Scan size: $(1 \times 1) \mu\text{m}^2$. Semi-contact AFM topography including areas of prior STM scans in (c), together with corresponding phase in (d), which highlights Re_2O_7 deposited structures. Scan size: $(30 \times 30) \mu\text{m}^2$. All scans taken in ambient. Process parameters: pre-growth substrate UHV annealing (350°C , 1 h), growth on substrate at RT.

the efficiency of sweeping the material as the smallest size scan window is the cleanest. Note that the particles were removed equally regardless of terraces edges. Those patterns confirm that Re_2O_7 nanoparticles were misplaced or removed from the STM-scanned locations. The smaller size STM scan, the more efficient sweeping the particles from the scan area – due to longer interaction time of the tip with each nanoparticle (the constant frequency scanning is typically used in our experiments and as a result of zooming in - the tip speed is decreased and the density of scanned lines increased).

AFM is a powerful tool for imaging and lithography of nanoparticles. Contact mode AFM is known for sweeping loose particles aside while scanning [166,167]. Such sweeping is shown in a sequence of scans in AFM semi-contact, contact, and semi-contact mode (see Figure 37). The initial condition of distributed Re_2O_7 nanoparticles on the graphene surface is shown in the topography image (Figure 37a). The corresponding phase image (Figure 37b) shows characteristic phase disturbances at the Re_2O_7 nanoparticles.

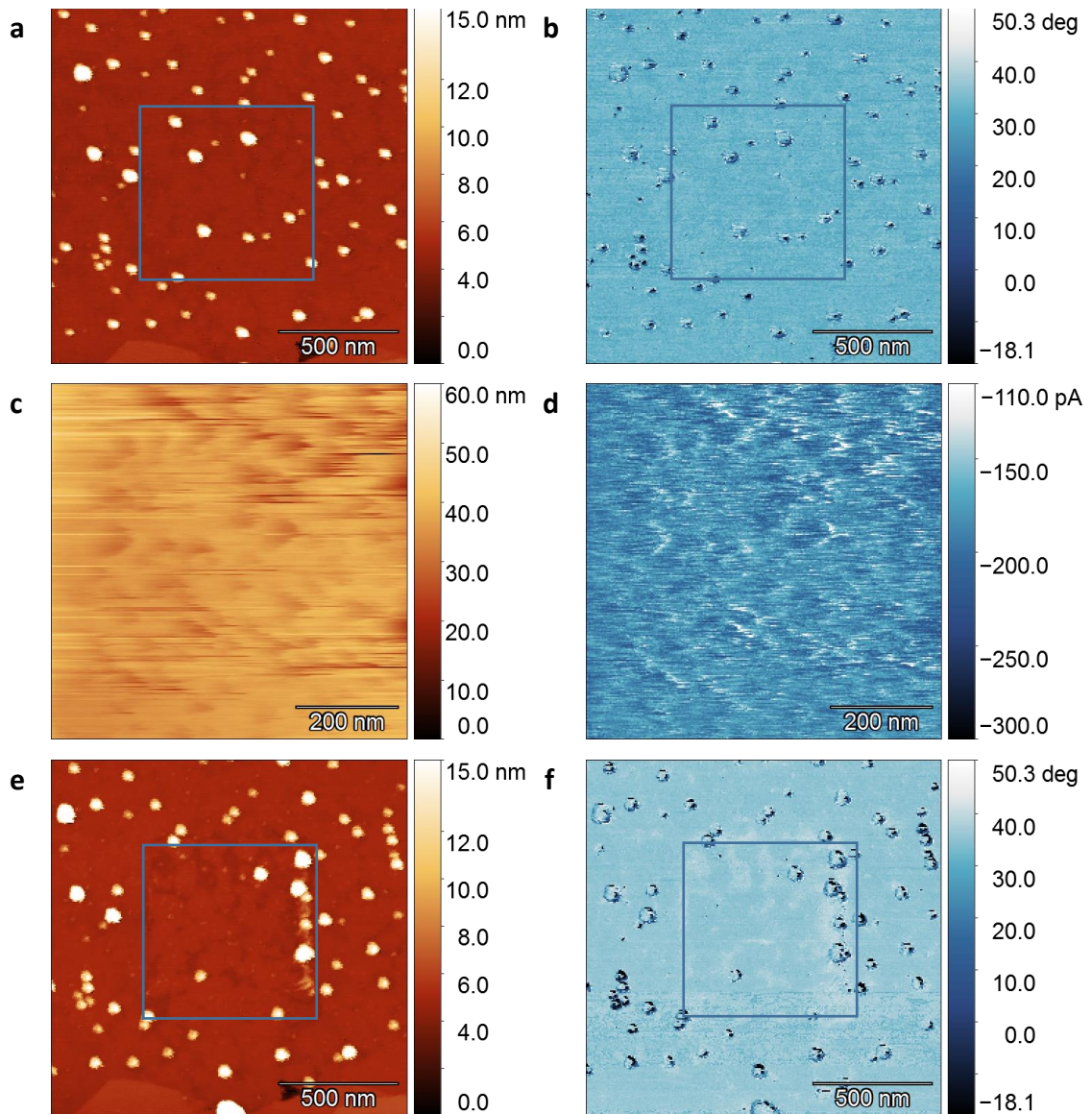


Figure 37: Sequence of AFM scanning in semi-contact, contact, and semi-contact mode: Re_2O_7 nanoparticles misplacement by AFM tip on graphene. AFM micrographs: topography in semi-contact mode in (a), together with phase in (b), which highlights Re_2O_7 initially deposited structures. Scan size: $(2 \times 2) \mu\text{m}^2$. Topography in contact mode in (c), together with DFL signal in (d). Scan size: $(1 \times 1) \mu\text{m}^2$; taken in marked area in (a-b). Topography in semi-contact mode in (e), together with corresponding phase in (f). Scan size: $(2 \times 2) \mu\text{m}^2$. All scans taken in ambient. Process parameters: pre-growth substrate UHV annealing (350°C , 1 h), growth on substrate at RT.

For this experiment, only one tip has been used. Because the tip is devoted to semi-contact operation, the imaging in contact mode leads to an only smeared image in all of the collected signals (Figure 37c–d). Such a scan should be understood in terms of nanolithography on the surface using shear forces. The scan in contact mode was taken in a framed window as shown in Figure 37a–b. The following scan in semi-contact mode and the exact location again shows misplacement of Re_2O_7 nanoparticles on graphene (see Figure 37e–f). Note that the

accumulation of the swept particles is at the right scan boundary. This can be explained by tip push mechanism, i.e. the tip initially moves from left to right pushing all nanoparticles to the right side of the scan frame. When the tip returns (moves from right to left) the interaction with nanoparticles is not strong enough to pull them toward left side of the scan frame. In consequence, the region at which nanoparticles are accumulating is selected by the first scan line, e.g. right (left) if forward scan direction if from left to right (right to left).

The presented sequence of the AFM scanning demonstrates the possibility of creating precise surface patterns or particle arrangements of Re_2O_7 nanoparticles on the graphene surface, offering the potential for an easy approach to nanolithography.

6.2.4. Controlling work function of graphene/ Re_2O_7 heterostructure: UPS Characterisation

We carried out UPS measurements to determine the work function of graphene/ Re_2O_7 heterostructure in function of nominal deposited thickness.

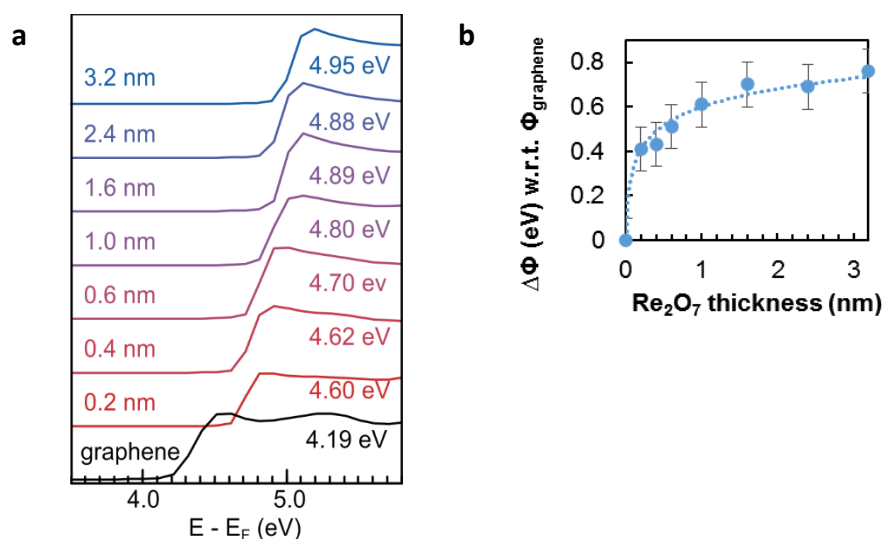


Figure 38: Work function evolution in function of deposition. (a) He I UPS spectra in secondary electron cut-off (SEC) region of graphene/ Re_2O_7 heterostructure. **(b)** changes of work function in function of nominal thickness of deposited Re_2O_7 . Nominal thicknesses of the oxide layers, and work functions, are denoted.

Figure 38a shows UPS spectra in the secondary electron cut-off (SEC) region for graphene and graphene/ Re_2O_7 heterostructures with gradually increasing oxide thickness. Note that the initial work function of graphene (not shown) and after annealing at 350 °C for 1 h (bottom spectrum, Figure 38a) were equal to 4.50 and 4.19 eV, respectively. The determined values agree with the theoretical predictions (4.35 eV [168]) and previous experiments (4.25 eV [169]) performed on bilayer graphene synthesised on SiC(0001). The WF of air-exposed

graphene is affected by the presence of moisture, oxygen, and other species; whereas annealing leads to decrease in WF of graphene by about 0.31 eV, confirming the effectiveness of contamination desorption.

Upon deposition of Re_2O_7 , the WF of graphene heterostructure increases rapidly up to a value of 4.60 eV for nominal oxide thickness of 0.2 nm. With increasing deposition time, thus increasing the nominal thickness of the oxide film, a gradual shift of the SEC position towards lower binding energy was observed, which is equivalent to an increase in WF of the heterostructure. Interestingly, even a small amount of Re_2O_7 leads to a relatively large shift of SEC position towards lower binding energy in comparison with pristine graphene. Upon deposition of nominally 3.2-nm-thick Re_2O_7 layer, the WF of heterostructure starts to saturate at a value of 4.95 eV (top spectrum, Figure 38a).

The above evolution is plotted in function of the nominal thickness of deposited Re_2O_7 in Figure 38b. Those results indicate that graphene heterostructure work function tuning in the range of 0.76 eV can be achieved. In accordance with XPS results (Figure 33), the observed changes in the electronic structure of the heterostructures should be related only to the thickness of the oxide film, which is chemically homogenous (in the meaning of oxidation states).

Finally, as was described in the case of MoO_3 uncoalesced films (see Section 2.4 and 5.2.2), the interpretation of UPS results is not easily conclusive for two-component surfaces. Because our observation in characterisation performed in ambient showed that Re_2O_7 nanoparticles do not fully cover the graphene surface, we believe the WF tuning by Re_2O_7 can achieve higher values. The trend of increasing the WF is accurate, however, the apparent saturation may lead to underestimation of intrinsic WF of Re_2O_7 in given conditions governed by limited coverage (some patches of graphene may be exposed). Moreover, if the coverage area by the oxide is insufficient to provide high intensity signal at SEC edge in UPS spectra, we may not be able to see in the measured evolution double-component features, as we could successfully distinguish for MoO_3 nanosheets on HOPG (Figure 5 and 29). The main factor is the lack of coalescence hindering the fully conclusive WF tuning, which remains a challenge to be met.

However, it should be also emphasised that the morphology of Re_2O_7 structures grown on graphene may be initially different than which we observed in air. Further studies in UHV are necessary to shine the light of this topic.

6.3. Conclusions

In this Chapter the synthesis of heterostructures of Re_2O_7 on graphene are described with the focus on the morphology and work function tuning. To sum up, we elaborate on the highlights stated at the beginning of the Chapter.

- I. The chemical structure of rhenium oxide structures was investigated in function of nominal thickness, i.e., duration of deposition.
 - The chemical composition of the rhenium oxide does not depend on its thickness, which was studied by XPS. The deposited structures were composed of Re_2O_7 , in average of 80% of composition, with nearly 20% of ReO_3 phase.
- II. The experiments involved the morphological characterisation of Re_2O_7 nanoparticles thermally evaporated on graphene in UHV and their high mobility on the substrate surface.
 - Morphology of rhenium oxide structures deposited on graphene was investigated by AFM in semi-contact mode, which allowed characterisation. The studies revealed created 3D structures of Re_2O_7 evenly distributed over the substrate surface, however fully coalesced films were hard to achieve.
 - Raman spectroscopy proved that deposited metal oxide films do not cause structural defects in graphene. This highlights that chosen method of deposition with selected working parameters is a non-destructive process for graphene.
- III. Test of mobility of obtained structures on the graphene surface.
 - One of the biggest problems we faced with the imaging by AFM (contact mode) and STM of the graphene/ Re_2O_7 system is the choice of operating parameters that allow scanning the nanoparticles without inducing their motion on the graphene surface. Re_2O_7 nanoparticles are highly mobile on the graphene surface, and STM investigations of electronic structure on the nanoscale seem very challenging as it has not been achieved yet.
 - Our experiments show that the nanoparticle system graphene/ Re_2O_7 is an ideal candidate for nanomanipulation studies aimed at investigating, e.g., the underlying friction mechanisms under both ultrahigh vacuum and air conditions.
- IV. We tuned the work function of graphene/ Re_2O_7 heterostructure by controlled deposition of Re oxide species.

- Particular emphasis was on discussing the electronic properties of the fabricated graphene/Re₂O₇ heterostructures studied globally by the UPS technique, as STS measurements on the nanoscale were not allowed due to the instability of Re₂O₇ structures on graphene.
- We presented WF modification from 4.2 eV to near 5.0 eV. UPS shows that upon deposition of Re₂O₇ on top of graphene, the WF of as-synthesised heterostructure increases gradually with film thickness. We believe that the WF can be further increased with further optimisation of achieving coalesced films of Re₂O₇.

We showed that apart from other previously used materials, Re₂O₇ can be successfully applied to tune the WF of graphene-based anodes. Our results emphasised the great potential of the modified graphene layer for use as a transparent anode and hole transport layer for organic electronic devices. As the evaporation of this material is processed at relatively low temperatures, it can be beneficial for fabricating organic electronic devices in combination with temperature-sensitive functional layers.

Conclusions

Driven by the interest in modifying graphene-based anodes, this Thesis has addressed the synthesis of selected transition metal oxides, namely molybdenum and rhenium oxides, on graphene and graphite substrates. As a result, the morphology of grown structures was studied, with particular emphasis on molybdenum oxide monolayers and differences between a few first layers. The electronic structure of obtained heterostructures was thoroughly investigated, particularly values of their work function under given environments.

The narration of the Thesis followed a trace of the ideal case of the crystalline, stable monolayer of MoO_3 grown on nearly defect-free graphene counterpart, HOPG, to switch to more practical choices of graphene synthesised on different substrates and with different thicknesses surrogating various MoO_3 structures. When layers of MoO_3 were achieved on graphene, we focused on workfunction investigation under ambient and UHV. Motivated by the success of high work function MoO_3 heterostructures, we compared it with a second oxide, Re_2O_7 .

In this study, a great emphasis was on MoO_3 in 2D form, so more detailed background information on MoO_3 mono- to few monolayers was provided that has not been gathered anywhere else so far.

As a first step, the study focused on the direct synthesis and *in-situ* characterisation of MoO_3 monolayer on HOPG, by thermal evaporation in UHV. In **Chapter 3**, the study of MoO_3 monolayers on HOPG was described in detail, using its surface as a model graphene system. We identified the 2D and single-crystal nature of the irregular-shaped MoO_3 domains by using various methods, including STM, c-AFM, LEED, and HR-TEM. To establish a base for 2D form of MoO_3 concerning growth habits and local electronic structure, we studied a model heterostructure of HOPG/ MoO_3 . XPS study identified little deviation from stoichiometry of MoO_3 . We found by STS narrow apparent bandgap uniform for the first layers, which is a novelty. Our analyses suggested the presence of an electron state around 1.3 eV below Fermi level, which is present for the first MoO_3 monolayer wetting the substrate. We connect this state with structure defects or interaction with the substrate. Additionally, the effect of air exposure was investigated by STM/STS and UPS, suggesting further closing of the bandgap. DFT calculations supported the experimental analysis predicting narrowing of the bandgap with reduction of monolayer MoO_3 .

Next, we addressed the deposition process of MoO_3 on graphene with different properties depending on a substrate (Cu or SiC) and thickness (from monolayer to few-layer graphene) to ultimately get as thin MoO_3 layer as possible on the graphene. **Chapter 4** presented a growth study of MoO_3 on graphene substrates revealing the difficulties in reproducing monolayers of MoO_3 grown on HOPG. Among the studied graphene substrates, we achieved lateral growth of MoO_3 only on few-layer graphene synthesised on SiC. MoO_3 was prone to form nanoparticles on monolayer graphene obtained on Cu and SiC under the same preparation and growth conditions. While monolayer graphene led to various undesired structures, we found high instability of MoO_3 on the graphene surface hindering STM characterisation. Moreover, by using LEED, we described that the chosen deposition method was harmless to graphene.

The third step was to explore the WF of MoO_3 under different conditions in order to determine the highest value of WF that MoO_3 had to offer while reaching the limit of the minimal thickness of films, i.e. going down to monolayers. **Chapter 5** was devoted to work function measurements in ambient and UHV conditions of MoO_3 monolayers on HOPG and graphene. In contrast to previous reports, we emphasised that crystalline MoO_3 guaranteed high work function of 6.4 eV and smooth surface, and in this case, this material does not require thicker films but coalesced monolayers. Moreover, with maturing of the synthesis of continuous 2D MoO_3 films, this material becomes a great candidate for ultrathin buffer layers for work function enhancement. Our results assess the high WF homogeneity of MoO_3 monolayers on the nanoscale by KPFM in UHV.

Therefore, the contribution of this study is going beyond the usual approach of finding the final saturation of WF with an increase in film thickness. Those findings suggest new approach in optimization of functional materials properties that is replacing the parameter of amount of material by focusing on its crystallographic and electronic structure. Results collected for this heterostructure were the subject of a scientific article which has been submitted and is currently under review.

Testing different conditions in this study defined the critical environment, UHV, for utilising the highest qualities of MoO_3 monolayers and possible threads found by air exposure. Moreover, the restoration method after air exposure was proposed and tested. Post-processing method of annealing after air exposure was investigated leading to main conclusion of limit of WF recovery lower for long exposures and higher for few-minutes exposures. However, the WF recovery is linked with structural changes visible on topography and chemical structure in reduction of MoO_3 monitored by KPFM, UPS and XPS.

The ability to synthesise 2D high-quality $\alpha\text{-MoO}_3$ films under UHV conditions allowed fundamental research on their surfaces and great advance in our understanding on their

properties. The ability to grow such structures in a controllable fashion on graphene opens possibilities for practical applications in organic electronics.

Finally, the another transition metal oxide grown on graphene, namely Re_2O_7 was investigated with focus on increasing the substrate work function. In contrast to MoO_3 , rhenium oxides are not yet commonly used in organic electronic devices. **Chapter 6** focused on studying graphene heterostructure with Re_2O_7 obtained by thermal evaporation in UHV. In particular, it described morphology, chemical composition, and the electronic properties, including increasing WF by deposition of Re_2O_7 structures monitored by AFM, XPS, and UPS respectively. Studying Re_2O_7 is not only much room for new applications and development of new heterostructures but also an advantage of lower temperatures of deposition as we found 260°C ideal for evaporation of Re_2O_7 structures with uniform chemical structure independent of thickness. Raman spectroscopy proved that deposition of Re_2O_7 do not cause structural defects in graphene. Most importantly, we presented WF increase of 0.8 eV. UPS showed that upon deposition of Re_2O_7 , the WF of graphene heterostructure increases gradually with film thickness.

In addition, the knowledge gained during the studies involved in the Thesis led to developing of a practical guide for interpretation of work function measurements on uncoalesced 2D films or nanosheets given in **Chapter 2**, where we comment on UPS measurement on 2D- MoO_3 nanosheets on HOPG with various area ratio between those two surface components. Such contribution carries universal implications for the work function characterisation of 2D materials beyond MoO_3 . Another practical guideline can be found in our optimised procedure of MoO_3 deposition on HOPG, with emphasis on cleaving the top surface under UHV conditions prior to MoO_3 growth. Furthermore, we gathered a database of available literature results helpful for Mo3d analysis by XPS in **Appendix A**.

The results presented in this Thesis proved that it is possible to synthesise MoO_3 monolayers on graphene, creating heterostructures of high work function. This is the first step in utilising the ultrathin graphene/ MoO_3 heterostructures with smooth surfaces in further applications. Re_2O_7 follows the same trend of enhancing work function at a specific thickness, which proves its potential in tuning heterostructure electronic structure. The main conclusion is that both graphene heterostructures are great candidates for anodes in organic electronics.

We thus consider this work an essential material for applied research, particularly for functionalising graphene with TMOs for application as transparent and flexible electrodes and employing 2D MoO_3 films in catalytic applications where high work function is required. We believe this Thesis contribution carries important implications and paves the way for designing more complex van der Waals heterostructures.

References

- [1] I.J. Park, T.S.I. Kim, T. Yoon, S. Kang, H. Cho, N.S. Cho, J.I. Lee, T.S.I. Kim, S.Y. Choi, Flexible and Transparent Graphene Electrode Architecture with Selective Defect Decoration for Organic Light-Emitting Diodes, *Adv. Funct. Mater.* 28 (2018) 1704435. <https://doi.org/10.1002/adfm.201704435>.
- [2] A. Klein, K. Christoph, C. Körber, A. Wachau, F. Säuberlich, Y. Gassenbauer, S.P. Harvey, D.E. Proffit, T.O. Mason, A. Klein, C. Körber, A. Wachau, F. Säuberlich, Y. Gassenbauer, S.P. Harvey, D.E. Proffit, T.O. Mason, Transparent Conducting Oxides for Photovoltaics: Manipulation of Fermi Level, Work Function and Energy Band Alignment, *Materials*. 3 (2010) 4892–4914. <https://doi.org/10.3390/ma3114892>.
- [3] J.-P. Yang, F. Bussolotti, S. Kera, N. Ueno, Origin and role of gap states in organic semiconductor studied by UPS: as the nature of organic molecular crystals, *J. Phys. D: Appl. Phys.* 50 (2017) 423002. <https://doi.org/10.1088/1361-6463/aa840f>.
- [4] V. V. Afanas'Ev, G. Delie, M. Houssa, I. Shlyakhov, A. Stesmans, V. Trepalin, V. V. Afanas'ev, G. Delie, M. Houssa, I. Shlyakhov, A. Stesmans, V. Trepalin, Band alignment at interfaces of two-dimensional materials: Internal photoemission analysis, *J. Phys. Condens. Matter*. 32 (2020) 413002. <https://doi.org/10.1088/1361-648X/ab937c>.
- [5] M.T. Greiner, M.G. Helander, W.-M. Tang, Z.-B. Wang, J. Qiu, Z.-H. Lu, Universal energy-level alignment of molecules on metal oxides, *Nat. Mater.* 11 (2012) 76–81. <https://doi.org/10.1038/nmat3159>.
- [6] Q.-H. Wu, Y. Zhao, G. Hong, J.-G. Ren, C. Wang, W. Zhang, S.-T. Lee, Electronic structure of MoO₃-x/graphene interface, *Carbon*. 65 (2013) 46–52. <https://doi.org/10.1016/j.carbon.2013.07.091>.
- [7] P. Kumbhakar, C. Chowde Gowda, P.L. Mahapatra, M. Mukherjee, K.D. Malviya, M. Chaker, A. Chandra, B. Lahiri, P.M. Ajayan, D. Jariwala, A. Singh, C.S. Tiwary, Emerging 2D metal oxides and their applications, *Mater. Today*. (2021). <https://doi.org/10.1016/j.mattod.2020.11.023>.
- [8] R.G. Gordon, Criteria for Choosing Transparent Conductors, *MRS Bull.* 25 (2000) 52–57. <https://doi.org/10.1557/mrs2000.151>.
- [9] D.S. Schulman, A.J. Arnold, S. Das, Contact engineering for 2D materials and devices, *Chem. Soc. Rev.* 47 (2018) 3037–3058. <https://doi.org/10.1039/C7CS00828G>.
- [10] C. Backes, A.M. Abdelkader, C. Alonso, A. Andrieux-Ledier, R. Arenal, J. Azpeitia, N. Balakrishnan, L. Banszerus, J. Barjon, R. Bartali, S. Bellani, C. Berger, R. Berger, M.M.B. Ortega, C. Bernard, P.H. Beton, A. Beyer, A. Bianco, P. Bøggild, F. Bonaccorso, G.B. Barin, C. Botas, R.A. Bueno, D. Carriazo, A. Castellanos-Gomez, M. Christian, A. Ciesielski, T. Ciuk, M.T. Cole, J. Coleman, C. Coletti, L. Crema, H. Cun, D. Dasler, D. De Fazio, N. Díez, S. Drieschner, G.S. Duesberg, R. Fasel, X. Feng, A. Fina, S. Forti, C. Galiotis, G. Garberoglio, J.M. García, J.A. Garrido, M. Gibertini, A. Götzhäuser, J. Gómez, T. Greber, F. Hauke, A. Hemmi, I. Hernandez-Rodriguez, A. Hirsch, S.A. Hodge, Y. Huttel, P.U. Jepsen, I. Jimenez, U. Kaiser, T. Kaplas, H. Kim, A. Kis, K. Papagelis, K. Kostarelos, A. Krajewska, K. Lee, C. Li, H. Lipsanen, A. Liscio, M.R. Lohe, A. Loiseau, L. Lombardi, M. Francisca López, O. Martin, C. Martín, L. Martínez, J.A. Martin-Gago, J. Ignacio Martínez, N. Marzari, Á. Mayoral, J. McManus, M. Melucci, J. Méndez, C. Merino, P. Merino, A.P. Meyer, E. Miniussi, V. Miseikis, N. Mishra, V. Morandi, C. Munuera, R. Muñoz, H. Nolan, L. Ortolani, A.K. Ott, I. Palacio, V. Palermo, J. Parthenios, I. Pasternak, A. Patane, M. Prato, H. Prevost, V. Prudkovskiy, N. Pugno, T. Rojo, A. Rossi, P. Ruffieux, P. Samorì, L. Schué, E. Setijadi, T. Seyller, G. Speranza, C. Stampfer, I. Stenger, W. Strupinski, Y. Svirko, S. Taioli, K.B.K. Teo, M. Testi, F. Tomarchio, M. Tortello, E. Treossi, A. Turchanin, E. Vazquez, E. Villaro, P.R. Whelan, Z. Xia, R. Yakimova, S. Yang, G.R. Yazdi, C. Yim, D. Yoon, X. Zhang, X. Zhuang, L. Colombo, A.C. Ferrari, M. Garcia-Hernandez, Production and processing of graphene and related materials, *2D Mater.* 7 (2020) 022001. <https://doi.org/10.1088/2053-1583/ab1e0a>.
- [11] T.H. Bointon, G.F. Jones, A. De Sanctis, R. Hill-Pearce, M.F. Craciun, S. Russo, Large-area functionalized CVD graphene for work function matched transparent electrodes, *Sci. Rep.* 5 (2015) 16464. <https://doi.org/10.1038/srep16464>.
- [12] W. Marchal, I. Verboven, J. Kesters, B. Moeremans, C. De Dobbelaere, G. Bonneux, K. Elen, B.

- Conings, W. Maes, H.G. Boyen, W. Deferme, M. Van Bael, A. Hardy, M. Van Bael, A. Hardy, Steering the properties of MoOx hole transporting layers in OPVs and OLEDs: Interface morphology vs. electronic structure, *Materials*. 10 (2017) 123. <https://doi.org/10.3390/ma10020123>.
- [13] J. Wei, D. Bai, L. Yang, Polymer Photovoltaic Cells with Rhenium Oxide as Anode Interlayer, *PLoS One*. 10 (2015) e0133725. <https://doi.org/10.1371/journal.pone.0133725>.
- [14] W. Choi, I. Lahiri, R. Seelaboyina, Y.S. Kang, Synthesis of Graphene and Its Applications: A Review, *Crit. Rev. Solid State Mater. Sci.* 35 (2010) 52–71. <https://doi.org/10.1080/10408430903505036>.
- [15] M. Qian, Q. Liu, W.S. Li, J.X. Man, Y.B. Zhao, Z.H. Lu, Dual Ag electrodes for semitransparent organic light-emitting diodes, *Org. Electron. Physics, Mater. Appl.* 57 (2018) 98–103. <https://doi.org/10.1016/j.orgel.2018.02.028>.
- [16] A.H. Castro Neto, F. Guinea, N.M.R. Peres, K.S. Novoselov, A.K. Geim, The electronic properties of graphene, *Rev. Mod. Phys.* 81 (2009) 109–162. <https://doi.org/10.1103/RevModPhys.81.109>.
- [17] R.R. Nair, P. Blake, A.N. Grigorenko, K.S. Novoselov, T.J. Booth, T. Stauber, N.M.R. Peres, A.K. Geim, Fine Structure Constant Defines Visual Transparency of Graphene, *Science*. 320 (2008) 1308–1308. <https://doi.org/10.1126/science.1156965>.
- [18] A. Sinterhauf, G.A. Traeger, D. Momeni Pakdehi, P. Schädlich, P. Willke, F. Speck, T. Seyller, C. Tegenkamp, K. Pierz, H.W. Schumacher, M. Wenderoth, D.M. Pakdehi, P. Schädlich, P. Willke, F. Speck, T. Seyller, C. Tegenkamp, K. Pierz, H.W. Schumacher, M. Wenderoth, Substrate induced nanoscale resistance variation in epitaxial graphene, *Nat. Commun.* 11 (2020) 1–9. <https://doi.org/10.1038/s41467-019-14192-0>.
- [19] J. Meyer, P.R. Kidambi, B.C. Bayer, C. Weijtens, A. Kuhn, A. Centeno, A. Pesquera, A. Zurutuza, J. Robertson, S. Hofmann, Metal oxide induced charge transfer doping and band alignment of graphene electrodes for efficient organic light emitting diodes., *Sci. Rep.* 4 (2014) 5380. <https://doi.org/10.1038/srep05380>.
- [20] P. Krukowski, D.A. Kowalczyk, M. Piskorski, P. Dabrowski, M. Rogala, P. Caban, P. Ciepielewski, J. Jung, J.M. Baranowski, J. Ulanski, Z. Klusek, Work Function Tunability of Graphene with Thermally Evaporated Rhenium Heptoxide for Transparent Electrode Applications, *Adv. Eng. Mater.* 22 (2020) 1900955. <https://doi.org/10.1002/adem.201900955>.
- [21] G. Franceschi, M. Wagner, J. Hofinger, T. Krajňák, M. Schmid, U. Diebold, M. Riva, Growth of In2O3 (111) thin films with optimized surfaces, *Phys. Rev. Mater.* 3 (2019) 103403. <https://doi.org/10.1103/PhysRevMaterials.3.103403>.
- [22] S.Y. Quek, M.M. Biener, J. Biener, C.M. Friend, E. Kaxiras, Tuning electronic properties of novel metal oxide nanocrystals using interface interactions: MoO3 monolayers on Au(111), *Surf. Sci.* 577 (2005) L71–L77. <https://doi.org/10.1016/j.susc.2005.01.012>.
- [23] D.J. Gaspar, E. Polikarpov, *OLED Fundamentals*, CRC Press, 2015. <https://doi.org/10.1201/b18485>.
- [24] J. Meyer, S. Hamwi, M. Kröger, W. Kowalsky, T. Riedl, A. Kahn, Transition Metal Oxides for Organic Electronics: Energetics, Device Physics and Applications, *Adv. Mater.* 24 (2012) 5408–5427. <https://doi.org/10.1002/adma.201201630>.
- [25] D.-S. Leem, J.-H. Lee, J.-J. Kim, J.-W. Kang, Highly efficient tandem p-i-n organic light-emitting diodes adopting a low temperature evaporated rhenium oxide interconnecting layer, *Appl. Phys. Lett.* 93 (2008) 103304. <https://doi.org/10.1063/1.2979706>.
- [26] D.-S. Leem, H.-D. Park, J.-W. Kang, J.-H. Lee, J.W. Kim, J.-J. Kim, Low driving voltage and high stability organic light-emitting diodes with rhenium oxide-doped hole transporting layer, *Appl. Phys. Lett.* 91 (2007) 011113. <https://doi.org/10.1063/1.2754635>.
- [27] I.A. de Castro, R.S. Datta, J.Z. Ou, A. Castellanos-Gomez, S. Sriram, T. Daeneke, K. Kalantar-zadeh, Molybdenum Oxides – From Fundamentals to Functionality, *Adv. Mater.* 29 (2017) 1701619. <https://doi.org/10.1002/adma.201701619>.
- [28] I.D. Baikie, U. Petermann, A. Speakman, B. Lägél, K.M. Dirscherl, P.J. Estrup, Work function study of rhenium oxidation using an ultra high vacuum scanning Kelvin probe, *J. Appl. Phys.* 88 (2000) 4371–4375. <https://doi.org/10.1063/1.1289486>.
- [29] Q. Zhou, W.C. Gong, L. Xie, C.G. Zheng, W. Zhang, B. Wang, Y.F. Zhang, X. Huang, Theoretical studies on the electronic structures and photoelectron spectra of tri-rhenium oxide clusters: Re3On - And Re3On (n = 1-6), *Spectrochim. Acta - Part A Mol. Biomol. Spectrosc.* 117 (2014) 651–657. <https://doi.org/10.1016/j.saa.2013.09.059>.

- [30] J.M. Fernandes, M.R. Kiran, H. Ulla, M.N. Satyanarayan, G. Umesh, Investigation of hole transport in α -NPD using impedance spectroscopy with F4TCNQ as hole-injection layer, *Superlattices Microstruct.* 83 (2015) 766–775. <https://doi.org/10.1016/j.spmi.2015.04.019>.
- [31] M.T. Greiner, Z.H. Lu, Thin-film metal oxides in organic semiconductor devices: Their electronic structures, work functions and interfaces, *NPG Asia Mater.* 5 (2013) e55–e55. <https://doi.org/10.1038/am.2013.29>.
- [32] C. Wang, I. Irfan, X. Liu, Y. Gao, Role of molybdenum oxide for organic electronics: Surface analytical studies, *J. Vac. Sci. Technol. B, Nanotechnol. Microelectron. Mater. Process. Meas. Phenom.* (2014). <https://doi.org/10.1116/1.4886364>.
- [33] M.G. Helander, M.T. Greiner, Z.B. Wang, Z.H. Lu, Pitfalls in measuring work function using photoelectron spectroscopy, *Appl. Surf. Sci.* 256 (2010) 2602–2605. <https://doi.org/10.1016/j.apsusc.2009.11.002>.
- [34] Y. Ishida, J.K. Jung, M.S. Kim, J. Kwon, Y.S. Kim, D. Chung, I. Song, C. Kim, T. Otsu, Y. Kobayashi, Work function seen with sub-meV precision through laser photoemission, *Commun. Phys.* 3 (2020) 158. <https://doi.org/10.1038/s42005-020-00426-x>.
- [35] T.C. Leung, C.L. Kao, W.S. Su, Y.J. Feng, C.T. Chan, Relationship between surface dipole, work function and charge transfer: Some exceptions to an established rule, *Phys. Rev. B.* 68 (2003) 195408. <https://doi.org/10.1103/PhysRevB.68.195408>.
- [36] D.K. Choi, D.H. Kim, C.M. Lee, H. Hafeez, S. Sarker, J.S. Yang, H.J. Chae, G.-W. Jeong, D.H. Choi, T.W. Kim, S. Yoo, J. Song, B.S. Ma, T.-S. Kim, C.H. Kim, H.J. Lee, J.W. Lee, D. Kim, T.-S. Bae, S.M. Yu, Y.-C. Kang, J. Park, K.-H. Kim, M. Sujak, M. Song, C.-S. Kim, S.Y. Ryu, Highly efficient, heat dissipating, stretchable organic light-emitting diodes based on a MoO₃/Au/MoO₃ electrode with encapsulation, *Nat. Commun.* 12 (2021) 2864. <https://doi.org/10.1038/s41467-021-23203-y>.
- [37] L. D’Arsié, S. Esconjauregui, R. Weatherup, Y. Guo, S. Bhardwaj, A. Centeno, A. Zurutuza, C. Cepek, J. Robertson, Stability of graphene doping with MoO₃ and I₂, *Appl. Phys. Lett.* 105 (2014) 103103. <https://doi.org/10.1063/1.4895025>.
- [38] M.T. Greiner, L. Chai, M.G. Helander, W.-M.M. Tang, Z.-H.H. Lu, Metal/Metal-Oxide Interfaces: How Metal Contacts Affect the Work Function and Band Structure of MoO₃, *Adv. Funct. Mater.* 23 (2013) 215–226. <https://doi.org/10.1002/adfm.201200993>.
- [39] R. Tokarz-Sobieraj, K. Hermann, M. Witko, A. Blume, G. Mestl, R. Schlögl, Properties of oxygen sites at the MoO₃(010) surface: density functional theory cluster studies and photoemission experiments, *Surf. Sci.* 489 (2001) 107–125. [https://doi.org/10.1016/S0039-6028\(01\)01169-4](https://doi.org/10.1016/S0039-6028(01)01169-4).
- [40] D.O. Scanlon, G.W. Watson, D.J. Payne, G.R. Atkinson, R.G. Egdell, D.S.L. Law, Theoretical and Experimental Study of the Electronic Structures of MoO₃ and MoO₂, *J. Phys. Chem. C.* 114 (2010) 4636–4645. <https://doi.org/10.1021/jp9093172>.
- [41] L. Zhang, X. He, K. Xing, W. Zhang, A. Tadich, P.K.J. Wong, D.-C. Qi, A.T.S. Wee, Is Charge-Transfer Doping Possible at the Interfaces of Monolayer VSe₂ with MoO₃ and K?, *ACS Appl. Mater. Interfaces.* 11 (2019) 43789–43795. <https://doi.org/10.1021/acsami.9b16822>.
- [42] J. Meyer, Electronic structure of molybdenum-oxide films and associated charge injection mechanisms in organic devices, *J. Photonics Energy.* 1 (2011) 011109. <https://doi.org/10.1117/1.3555081>.
- [43] Irfan, H. Ding, Y. Gao, C. Small, D.Y. Kim, J. Subbiah, F. So, Energy level evolution of air and oxygen exposed molybdenum trioxide films, *Appl. Phys. Lett.* 96 (2010) 243307. <https://doi.org/10.1063/1.3454779>.
- [44] A.J. Molina-Mendoza, J.L. Lado, J. Island, M.A. Niño, L. Aballe, M. Foerster, F.Y. Bruno, A. López-Moreno, L. Vaquero-Garzon, H.S.J. van der Zant, G. Rubio-Bollinger, N. Agrait, E. Perez, J. Fernandez-Rossier, A. Castellanos-Gomez, Centimeter-scale synthesis of ultrathin layered MoO₃ by van der Waals epitaxy, *Chem. Mater.* 28 (2015) 4042–4051. <https://doi.org/10.1021/acs.chemmater.6b01505>.
- [45] T. Das, S. Tosoni, G. Pacchioni, Structural and electronic properties of bulk and ultrathin layers of V₂O₅ and MoO₃, *Comput. Mater. Sci.* 163 (2019) 230–240. <https://doi.org/10.1016/j.commatsci.2019.03.027>.
- [46] E.D. Hanson, L. Lajaunie, S. Hao, B.D. Myers, F. Shi, A.A. Murthy, C. Wolverton, R. Arenal, V.P. Dravid, Systematic Study of Oxygen Vacancy Tunable Transport Properties of Few-Layer MoO_{3-x} Enabled by Vapor-Based Synthesis, *Adv. Funct. Mater.* 27 (2017) 1605380. <https://doi.org/10.1002/adfm.201605380>.
- [47] Y. Guo, L. Ma, K. Mao, M. Ju, Y. Bai, J. Zhao, X.C. Zeng, Eighteen functional monolayer metal

- oxides: wide bandgap semiconductors with superior oxidation resistance and ultrahigh carrier mobility, *Nanoscale Horizons*. 4 (2019) 592–600. <https://doi.org/10.1039/C8NH00273H>.
- [48] F. Li, Z. Chen, Tuning electronic and magnetic properties of MoO₃ sheets by cutting, hydrogenation, and external strain: a computational investigation, *Nanoscale*. 5 (2013) 5321. <https://doi.org/10.1039/c3nr33009e>.
- [49] S. Prada, U. Martinez, G. Pacchioni, Work function changes induced by deposition of ultrathin dielectric films on metals: A theoretical analysis, *Phys. Rev. B*. 78 (2008) 235423. <https://doi.org/10.1103/PhysRevB.78.235423>.
- [50] L. Giordano, F. Cinquini, G. Pacchioni, Tuning the surface metal work function by deposition of ultrathin oxide films: Density functional calculations, *Phys. Rev. B*. 73 (2006) 045414. <https://doi.org/10.1103/PhysRevB.73.045414>.
- [51] K. Pabianek, P. Krukowski, K. Polański, P. Ciepielewski, J.M. Baranowski, M. Rogala, W. Kozłowski, A. Busiakiewicz, Interactions of Ti and its oxides with selected surfaces: Si(100), HOPG(0001) and graphene/4H-SiC(0001), *Surf. Coatings Technol.* 397 (2020) 126033. <https://doi.org/10.1016/j.surfcoat.2020.126033>.
- [52] D. Kim, D. Lee, Y. Lee, D.Y. Jeon, Work-Function Engineering of Graphene Anode by Bis(trifluoromethanesulfonyl)amide Doping for Efficient Polymer Light-Emitting Diodes, *Adv. Funct. Mater.* 23 (2013) 5049–5055. <https://doi.org/10.1002/adfm.201301386>.
- [53] S. Bae, H. Kim, Y. Lee, X. Xu, J.-S. Park, Y. Zheng, J. Balakrishnan, T. Lei, H. Ri Kim, Y. Il Song, Y.-J. Kim, K.S. Kim, B. Özyilmaz, J.-H. Ahn, B.H. Hong, S. Iijima, Roll-to-roll production of 30-inch graphene films for transparent electrodes, *Nat. Nanotechnol.* 5 (2010) 574–578. <https://doi.org/10.1038/nnano.2010.132>.
- [54] H. Kanno, R.J. Holmes, Y. Sun, S. Kena-Cohen, S.R. Forrest, White Stacked Electrophosphorescent Organic Light-Emitting Devices Employing MoO₃ as a Charge-Generation Layer, *Adv. Mater.* 18 (2006) 339–342. <https://doi.org/10.1002/adma.200501915>.
- [55] Suchitra, J. Pan, U. V. Waghmare, High tunability of the work function of (001) surface of ReO₃ with O-vacancies: First principles analysis, *J. Appl. Phys.* 116 (2014) 034304. <https://doi.org/10.1063/1.4887521>.
- [56] S. Walia, S. Balendhran, H. Nili, S. Zhuyikov, G. Rosengarten, Q.H. Wang, M. Bhaskaran, S. Sriram, M.S. Strano, K. Kalantar-zadeh, Transition metal oxides – Thermoelectric properties, *Prog. Mater. Sci.* 58 (2013) 1443–1489. <https://doi.org/10.1016/j.pmatsci.2013.06.003>.
- [57] C.N.R. Rao, Transition Metal Oxides, *Annu. Rev. Phys. Chem.* 40 (1989) 291–326. <https://doi.org/10.1146/annurev.pc.40.100189.001451>.
- [58] S.Y. Quek, E. Kaxiras, Applications of Thin Film Oxides in Catalysis, in: *Thin Film Met.*, Springer US, Boston, MA, 2010: pp. 281–301. https://doi.org/10.1007/978-1-4419-0664-9_9.
- [59] M.T. Greiner, L. Chai, M.G. Helander, W.-M. Tang, Z.-H. Lu, Transition Metal Oxide Work Functions: The Influence of Cation Oxidation State and Oxygen Vacancies, *Adv. Funct. Mater.* 22 (2012) 4557–4568. <https://doi.org/10.1002/adfm.201200615>.
- [60] M. Rellán-Piñeiro, N. López, One Oxygen Vacancy, Two Charge States: Characterization of Reduced α -MoO₃ (010) through Theoretical Methods, *J. Phys. Chem. Lett.* 9 (2018) 2568–2573. <https://doi.org/10.1021/acs.jpcclett.8b00536>.
- [61] K. Kalantar-zadeh, J.Z. Ou, T. Daeneke, A. Mitchell, T. Sasaki, M.S. Fuhrer, Two dimensional and layered transition metal oxides, *Appl. Mater. Today*. 5 (2016) 73–89. <https://doi.org/10.1016/j.apmt.2016.09.012>.
- [62] G. Hu, Q. Ou, G. Si, Y. Wu, J. Wu, Z. Dai, A. Krasnok, Y. Mazor, Q. Zhang, Q. Bao, C.-W. Qiu, A. Alù, Topological polaritons and photonic magic angles in twisted α -MoO₃ bilayers, *Nature*. 582 (2020) 209–213. <https://doi.org/10.1038/s41586-020-2359-9>.
- [63] R.L. Smith, G.S. Rohrer, Scanning probe microscopy of cleaved molybdates: α -MoO₃(010), Mo₁₈O₅₂(100), Mo₈O₂₃(010), and η -Mo₄O₁₁(100), *J. Solid State Chem.* 124 (1996) 104–115. <https://doi.org/10.1006/jssc.1996.0213>.
- [64] Y. Guo, J. Robertson, Origin of the high work function and high conductivity of MoO₃, *Appl. Phys. Lett.* 105 (2014) 222110. <https://doi.org/10.1063/1.4903538>.
- [65] X. Liao, A.R. Jeong, R.G. Wilks, S. Wiesner, M. Rusu, R. Félix, T. Xiao, C. Hartmann, M. Bär, Tunability of MoO₃ Thin-Film Properties Due to Annealing in Situ Monitored by Hard X-ray Photoemission, *ACS Omega*. 4 (2019) 10985–10990. <https://doi.org/10.1021/acsomega.9b01027>.
- [66] M. Rogala, S. Sokółowski, U. Ukegbu, A. Mierzwa, R. Szoszkiewicz, Direct Identification of Surface

- Bound MoO₃ on Single MoS₂ Flakes Heated in Dry and Humid Air, *Adv. Mater. Interfaces*. 8 (2021) 2100328. <https://doi.org/10.1002/admi.202100328>.
- [67] D.A. Kowalczyk, M. Rogala, K. Szałowski, W. Kozłowski, I. Lutsyk, M. Piskorski, P. Krukowski, P. Dąbrowski, D. Belić, M. Cichomski, Z. Kłusek, P.J. Kowalczyk, Local electronic structure of stable monolayers of α -MoO_{3-x} grown on graphite substrate, *2D Mater.* 8 (2021) 025005. <https://doi.org/10.1088/2053-1583/abc10>.
- [68] L.E. Firment, A. Ferretti, Stoichiometric and oxygen deficient MoO₃(010) surfaces, *Surf. Sci.* 129 (1983) 155–176. [https://doi.org/10.1016/0039-6028\(83\)90100-0](https://doi.org/10.1016/0039-6028(83)90100-0).
- [69] Z. Zhang, Y. Xiao, H.-X. Wei, G.-F. Ma, S. Duhm, Y.-Q. Li, J.-X. Tang, Impact of Oxygen Vacancy on Energy-Level Alignment at MoO_x/Organic Interfaces, *Appl. Phys. Express*. 6 (2013) 095701. <https://doi.org/10.7567/APEX.6.095701>.
- [70] J.H. Kim, J.K. Dash, J. Kwon, C. Hyun, H. Kim, E. Ji, G.-H. Lee, van der Waals epitaxial growth of single crystal α -MoO₃ layers on layered materials growth templates, *2D Mater.* 6 (2018) 015016. <https://doi.org/10.1088/2053-1583/aaedc8>.
- [71] J.H. Kim, C. Hyun, H. Kim, J.K. Dash, K. Ihm, G.-H. Lee, Thickness-Insensitive Properties of α -MoO₃ Nanosheets by Weak Interlayer Coupling, *Nano Lett.* 19 (2019) 8868–8876. <https://doi.org/10.1021/acs.nanolett.9b03701>.
- [72] Y. Du, G. Li, E.W. Peterson, J. Zhou, X. Zhang, R. Mu, Z. Dohnálek, M. Bowden, I. Lyubinetzky, S.A. Chambers, Iso-oriented monolayer α -MoO₃(010) films epitaxially grown on SrTiO₃(001), *Nanoscale*. 8 (2016) 3119–3124. <https://doi.org/10.1039/c5nr07745a>.
- [73] T. Radlinger (Master Thesis), Growth and structure of 2D MoO₃ and WO₃ layers on Pd(100), Graz, (2019). urn:nbn:at:at-ubg:1-136826. <https://unipub.uni-graz.at/urn:urn:nbn:at:at-ubg:1-136826>.
- [74] D. Wang, J.-N. Li, Y. Zhou, D.-H. Xu, X. Xiong, R.-W. Peng, M. Wang, Van der Waals epitaxy of ultrathin α -MoO₃ sheets on mica substrate with single-unit-cell thickness, *Appl. Phys. Lett.* 108 (2016) 053107. <https://doi.org/10.1063/1.4941402>.
- [75] L. Cai, C.J. McClellan, A.L. Koh, H. Li, E. Yalon, E. Pop, X. Zheng, C.J. McClellan, L. Cai, A.L. Koh, E. Pop, C.J. McClellan, A.L. Koh, H. Li, E. Yalon, E. Pop, X. Zheng, Rapid flame synthesis of atomically thin MoO₃ down to monolayer thickness for effective hole doping of WSe₂, *Nano Lett.* 17 (2017) 3854–3861. <https://doi.org/10.1021/acs.nanolett.7b01322>.
- [76] M.M. Biener, C.M. Friend, Heteroepitaxial growth of novel MoO₃ nanostructures on Au(111), *Surf. Sci.* 559 (2004) L173–L179. <https://doi.org/10.1016/j.susc.2004.04.021>.
- [77] M.M. Biener, J. Biener, R. Schalek, C.M. Friend, Growth of nanocrystalline MoO₃ on Au(111) studied by in situ scanning tunneling microscopy, *J. Chem. Phys.* 121 (2004) 12010–12016. <https://doi.org/10.1063/1.1808422>.
- [78] X. Deng, S.Y. Quek, M.M. Biener, J. Biener, D.H. Kang, R. Schalek, E. Kaxiras, C.M. Friend, Selective thermal reduction of single-layer MoO₃ nanostructures on Au(111), *Surf. Sci.* 602 (2008) 1166–1174. <https://doi.org/10.1016/j.susc.2008.01.014>.
- [79] S. Guimond, D. Göbke, J.M. Sturm, Y. Romanyshyn, H. Kuhlenbeck, M. Cavalleri, H.J. Freund, Well-ordered molybdenum oxide layers on Au(111): Preparation and properties, *J. Phys. Chem. C*. 117 (2013) 8746–8757. <https://doi.org/10.1021/jp3113792>.
- [80] E. Primorac, H. Kuhlenbeck, H.-J. Freund, LEED I/V determination of the structure of a MoO₃ monolayer on Au(111): Testing the performance of the CMA-ES evolutionary strategy algorithm, differential evolution, a genetic algorithm and tensor LEED based structural optimization, *Surf. Sci.* 649 (2016) 90–100. <https://doi.org/10.1016/j.susc.2016.01.030>.
- [81] T.Y. Ko, A. Jeong, W. Kim, J. Lee, Y. Kim, J.E. Lee, G.H. Ryu, K. Park, D. Kim, Z. Lee, M.H. Lee, C. Lee, S. Ryu, On-stack two-dimensional conversion of MoS₂ into MoO₃, *2D Mater.* 4 (2017) 014003. <https://doi.org/10.1088/2053-1583/4/1/014003>.
- [82] L. Cai, P.M. Rao, X. Zheng, Morphology-Controlled Flame Synthesis of Single, Branched, and Flower-like α -MoO₃ Nanobelt Arrays, *Nano Lett.* 11 (2011) 872–877. <https://doi.org/10.1021/nl104270u>.
- [83] S. Puebla, R. D'Agosta, G. Sanchez-Santolino, R. Frisenda, C. Munuera, A. Castellanos-Gomez, In-plane anisotropic optical and mechanical properties of two-dimensional MoO₃, *Npj 2D Mater. Appl.* 5 (2021) 37. <https://doi.org/10.1038/s41699-021-00220-5>.
- [84] M.H. Alam, S. Chowdhury, A. Roy, X. Wu, R. Ge, M.A. Rodder, J. Chen, Y. Lu, C. Stern, L. Houben, R. Chrostowski, S.R. Burlison, S.J. Yang, M.I. Serna, A. Dodabalapur, F. Mangolini, D. Naveh, J.C. Lee, S.K. Banerjee, J.H. Warner, D. Akinwande, Wafer-Scalable Single-Layer Amorphous

- Molybdenum Trioxide, *ACS Nano*. 16 (2022) 3756–3767.
<https://doi.org/10.1021/acsnano.1c07705>.
- [85] K.G. Azzam, I. V. Babich, K. Seshan, B.L. Mojet, L. Lefferts, Stable and Efficient Pt-Re/TiO₂ catalysts for Water-Gas-Shift: On the Effect of Rhenium, *ChemCatChem*. 5 (2013) 557–564.
<https://doi.org/10.1002/cctc.201200492>.
- [86] J.C. Mol, Olefin metathesis over supported rhenium oxide catalysts, *Catal. Today*. 51 (1999) 289–299. [https://doi.org/10.1016/S0920-5861\(99\)00051-6](https://doi.org/10.1016/S0920-5861(99)00051-6).
- [87] M. Komiyama, Y. Ogino, Y. Akai, M. Goto, X-ray photoelectron spectroscopic studies of unsupported and supported rhenium using argon-ion bombardment, *J. Chem. Soc. Faraday Trans. 2 Mol. Chem. Phys.* 79 (1983) 1719–1728. <https://doi.org/10.1039/F29837901719>.
- [88] M.T. Greiner, T.C.R. Rocha, B. Johnson, A. Klyushin, A. Knop-Gericke, R. Schlögl, The Oxidation of Rhenium and Identification of Rhenium Oxides During Catalytic Partial Oxidation of Ethylene: An In-Situ XPS Study, *Zeitschrift Für Phys. Chemie*. 228 (2014) 521–541.
<https://doi.org/10.1515/zpch-2014-0002>.
- [89] Y. Jia, L. Duan, D. Zhang, J. Qiao, G. Dong, L. Wang, Y. Qiu, Low-temperature evaporable Re₂O₇: An efficient p-dopant for OLEDs, *J. Phys. Chem. C*. 117 (2013) 13763–13769.
<https://doi.org/10.1021/jp400003m>.
- [90] M. Ghanashyam Krishna, A.K. Bhattacharya, Growth of rhenium oxide thin films, *Solid State Commun.* 116 (2000) 637–641. [https://doi.org/10.1016/S0038-1098\(00\)00386-0](https://doi.org/10.1016/S0038-1098(00)00386-0).
- [91] D. Adler, Insulating and Metallic States in Transition Metal Oxides, in: 1968: pp. 1–113.
[https://doi.org/10.1016/S0081-1947\(08\)60739-0](https://doi.org/10.1016/S0081-1947(08)60739-0).
- [92] K. V. Lawler, B.C. Childs, D.S. Mast, K.R. Czerwinski, A.P. Sattelberger, F. Poineau, P.M. Forster, Molecular and Electronic Structures of M₂O₇ (M = Mn, Tc, Re), *Inorg. Chem.* 56 (2017) 2448–2458. <https://doi.org/10.1021/acs.inorgchem.6b02503>.
- [93] A. Jain, S.P. Ong, G. Hautier, W. Chen, W.D. Richards, S. Dacek, S. Cholia, D. Gunter, D. Skinner, G. Ceder, K.A. Persson, Commentary: The Materials Project: A materials genome approach to accelerating materials innovation, *APL Mater.* 1 (2013) 011002.
<https://doi.org/10.1063/1.4812323>.
- [94] B. Krebs, A. Mueller, H.H. Beyer, Crystal structure of rhenium(VII) oxide, *Inorg. Chem.* 8 (1969) 436–443. <https://doi.org/10.1021/ic50073a006>.
- [95] M. Stachiotti, F. Cora, C. Catlow, First-principles investigation of rhenium related oxides, *Phys. Rev. B - Condens. Matter Mater. Phys.* 55 (1997) 7508–7514.
<https://doi.org/10.1103/PhysRevB.55.7508>.
- [96] S.-S. Wang, Y. Liu, Z.-M. Yu, X.-L. Sheng, S.A. Yang, Hourglass Dirac chain metal in rhenium dioxide, *Nat. Commun.* 8 (2017) 1844. <https://doi.org/10.1038/s41467-017-01986-3>.
- [97] G. Rouschias, Recent advances in the chemistry of rhenium, *Chem. Rev.* 74 (1974) 531–566.
<https://doi.org/10.1021/cr60291a002>.
- [98] K.M. Shapiro, E S and Avaev, V I and Antoshin, G N and Ryashentseva, M A and Minachev, XPS (X-ray photoelectron spectroscopy) studies of the rhenium state in supported Re catalysts, *J. Catal.; (United States)*. 55:3 (1978). <https://www.osti.gov/biblio/7139029>.
- [99] A. Cimino, B.A. De Angelis, D. Gazzoli, M. Valigi, Photoelectron Spectroscopy (XPS) and Thermogravimetry (TG) of Pure and Supported Rhenium Oxides. 2. Rhenium Oxides on Titanium Dioxide, *Zeitschrift Fur Anorg. Und Allg. Chemie*. 471 (1980) 208–226.
<https://doi.org/10.1002/zaac.19804710124>.
- [100] W.T. Tysoe, F. Zaera, G.A. Somorjai, An XPS study of the oxidation and reduction of the rhenium-platinum system under atmospheric conditions, *Surf. Sci.* 200 (1988) 1–14.
[https://doi.org/10.1016/0039-6028\(88\)90428-1](https://doi.org/10.1016/0039-6028(88)90428-1).
- [101] K.S. Novoselov, A.K. Geim, S. V. Morozov, D. Jiang, Y. Zhang, S. V. Dubonos, I. V. Grigorieva, A.A. Firsov, Electric field in atomically thin carbon films, *Science*. 306 (2004) 666–669.
<https://doi.org/10.1126/science.1102896>.
- [102] S. Das Sarma, S. Adam, E.H. Hwang, E. Rossi, Electronic transport in two-dimensional graphene, *Rev. Mod. Phys.* 83 (2011) 407–470. <https://doi.org/10.1103/RevModPhys.83.407>.
- [103] S. Pang, Y. Hernandez, X. Feng, K. Müllen, Graphene as Transparent Electrode Material for Organic Electronics, *Adv. Mater.* 23 (2011) 2779–2795.
<https://doi.org/10.1002/adma.201100304>.
- [104] S.-M. Lee, J.-H. Kim, J.-H. Ahn, Graphene as a flexible electronic material: mechanical limitations by defect formation and efforts to overcome, *Mater. Today*. 18 (2015) 336–344.

- <https://doi.org/10.1016/j.mattod.2015.01.017>.
- [105] W. Tian, W. Li, W. Yu, X. Liu, A review on lattice defects in graphene: Types generation effects and regulation, *Micromachines*. 8 (2017) 163. <https://doi.org/10.3390/mi8050163>.
- [106] I.A. Kostogrud, E. V. Boyko, D. V. Smovzh, CVD Graphene Transfer from Copper Substrate to Polymer, in: *Mater. Today Proc.*, Elsevier Ltd, 2017: pp. 11476–11479. <https://doi.org/10.1016/j.matpr.2017.09.032>.
- [107] A. Di Bartolomeo, Graphene Schottky diodes: An experimental review of the rectifying graphene/semiconductor heterojunction, *Phys. Rep.* 606 (2016) 1–58. <https://doi.org/10.1016/j.physrep.2015.10.003>.
- [108] F. Xia, V. Perebeinos, Y.M. Lin, Y. Wu, P. Avouris, The origins and limits of metal-graphene junction resistance, *Nat. Nanotechnol.* 6 (2011) 179–184. <https://doi.org/10.1038/nnano.2011.6>.
- [109] H. Park, P.R. Brown, V. Bulović, J. Kong, Graphene As Transparent Conducting Electrodes in Organic Photovoltaics: Studies in Graphene Morphology, Hole Transporting Layers, and Counter Electrodes, *Nano Lett.* 12 (2012) 133–140. <https://doi.org/10.1021/nl2029859>.
- [110] P.J. Kowalczyk, S.A. Brown, T. Maerkl, Q. Lu, C.-K. Chiu, Y. Liu, S.A. Yang, X. Wang, I. Zasada, F. Genuzio, T.O. Montes, A. Locatelli, T.-C. Chiang, G. Bian, Realization of Symmetry-Enforced Two-Dimensional Dirac Fermions in Nonsymmorphic α -Bismuthene, *ACS Nano*. 14 (2020) 1888–1894. <https://doi.org/10.1021/acsnano.9b08136>.
- [111] O. Mahapatra, P.J. Kowalczyk, S.A. Brown, Growth and electronic properties of NaCl on HOPG, *Surf. Sci.* 620 (2014) 45–50. <https://doi.org/10.1016/j.susc.2013.09.028>.
- [112] E. Meyer, H.J. Hug, R. Bennewitz, *Scanning Probe Microscopy*, Springer Berlin Heidelberg, Berlin, Heidelberg, 2004. <https://doi.org/10.1007/978-3-662-09801-1>.
- [113] N. Niliius, Properties of oxide thin films and their adsorption behavior studied by scanning tunneling microscopy and conductance spectroscopy, *Surf. Sci. Rep.* 64 (2009) 595–659. <https://doi.org/10.1016/j.surfrep.2009.07.004>.
- [114] W. Strupinski, K. Grodecki, A. Wyszomolek, R. Stepniowski, T. Szkopek, P.E. Gaskell, A. Grüneis, D. Haberer, R. Bozek, J. Krupka, J.M. Baranowski, Graphene Epitaxy by Chemical Vapor Deposition on SiC, *Nano Lett.* 11 (2011) 1786–1791. <https://doi.org/10.1021/nl200390e>.
- [115] P. Ciochoń, Ł. Bodek, M. Garb, Ł. Zajac, J.J. Kołodziej, Si beam-assisted graphitization of SiC (0001), *Appl. Phys. A*. 124 (2018) 727. <https://doi.org/10.1007/s00339-018-2145-9>.
- [116] M. Ohkubo, K. Fukai, M. Kohji, N. Iwata, H. Yamamoto, Preparation of conductive ReO₃ thin films, *Supercond. Sci. Technol.* 15 (2002) 1778–1780. <https://doi.org/10.1088/0953-2048/15/12/332>.
- [117] I. Horcas, R. Fernández, J.M. Gómez-Rodríguez, J. Colchero, J. Gómez-Herrero, A.M. Baro, WSXM: A software for scanning probe microscopy and a tool for nanotechnology, *Rev. Sci. Instrum.* 78 (2007) 013705. <https://doi.org/10.1063/1.2432410>.
- [118] D. Nečas, P. Klapeček, Gwyddion: an open-source software for SPM data analysis, *Open Phys.* 10 (2012). <https://doi.org/10.2478/s11534-011-0096-2>.
- [119] T. Schultz, T. Lenz, N. Kotadiya, G. Heimel, G. Glasser, R. Berger, P.W.M.M. Blom, P. Amsalem, D.M. De Leeuw, N. Koch, Reliable Work Function Determination of Multicomponent Surfaces and Interfaces: The Role of Electrostatic Potentials in Ultraviolet Photoelectron Spectroscopy, *Adv. Mater. Interfaces*. 4 (2017) 1700324. <https://doi.org/10.1002/admi.201700324>.
- [120] A. Sharma, R. Berger, D.A. Lewis, G.G. Andersson, Invisible high workfunction materials on heterogeneous surfaces, *Appl. Surf. Sci.* 327 (2015) 22–26. <https://doi.org/10.1016/j.apsusc.2014.11.089>.
- [121] T. Schultz, P. Amsalem, N.B. Kotadiya, T. Lenz, P.W.M. Blom, N. Koch, Importance of Substrate Work Function Homogeneity for Reliable Ionization Energy Determination by Photoelectron Spectroscopy, *Phys. Status Solidi*. 256 (2019) 1800299. <https://doi.org/10.1002/pssb.201800299>.
- [122] P. Giannozzi, O. Andreussi, T. Brumme, O. Bunau, M. Buongiorno Nardelli, M. Calandra, R. Car, C. Cavazzoni, D. Ceresoli, M. Cococcioni, N. Colonna, I. Carnimeo, A. Dal Corso, S. de Gironcoli, P. Delugas, R.A. DiStasio, A. Ferretti, A. Floris, G. Fratesi, G. Fugallo, R. Gebauer, U. Gerstmann, F. Giustino, T. Gorni, J. Jia, M. Kawamura, H.-Y. Ko, A. Kokalj, E. Küçükbenli, M. Lazzeri, M. Marsili, N. Marzari, F. Mauri, N.L. Nguyen, H.-V. Nguyen, A. Otero-de-la-Roza, L. Paulatto, S. Poncé, D. Rocca, R. Sabatini, B. Santra, M. Schlipf, A.P. Seitsonen, A. Smogunov, I. Timrov, T. Thonhauser, P. Umari, N. Vast, X. Wu, S. Baroni, Advanced capabilities for materials modelling with Quantum

- ESPRESSO, *J. Phys. Condens. Matter.* 29 (2017) 465901. <https://doi.org/10.1088/1361-648X/aa8f79>.
- [123] P. Giannozzi, S. Baroni, N. Bonini, M. Calandra, R. Car, C. Cavazzoni, D. Ceresoli, G.L. Chiarotti, M. Cococcioni, I. Dabo, A. Dal Corso, S. de Gironcoli, S. Fabris, G. Fratesi, R. Gebauer, U. Gerstmann, C. Gougoussis, A. Kokalj, M. Lazzeri, L. Martin-Samos, N. Marzari, F. Mauri, R. Mazzarello, S. Paolini, A. Pasquarello, L. Paulatto, C. Sbraccia, S. Scandolo, G. Sclauzero, A.P. Seitsonen, A. Smogunov, P. Umari, R.M. Wentzcovitch, QUANTUM ESPRESSO: a modular and open-source software project for quantum simulations of materials, *J. Phys. Condens. Matter.* 21 (2009) 395502. <https://doi.org/10.1088/0953-8984/21/39/395502>.
- [124] K. Momma, F. Izumi, VESTA 3 for three-dimensional visualization of crystal, volumetric and morphology data, *J. Appl. Crystallogr.* 44 (2011) 1272–1276. <https://doi.org/10.1107/S0021889811038970>.
- [125] K. Hermann, M. Van Hove, LEEDpat, Version 4.2, www.fhi-berlin.mpg.de/KHsoftware/LEEDpat/index.htm, (2014).
- [126] F. Werfel, E. Minni, Photoemission study of the electronic structure of Mo and Mo oxides, *J. Phys. C Solid State Phys.* 16 (1983) 6091–6100. <https://doi.org/10.1088/0022-3719/16/31/022>.
- [127] K.P. Reddy, N.B. Mhamane, M.K. Ghosal, C.S. Gopinath, Mapping Valence Band and Interface Electronic Structure Changes during the Oxidation of Mo to MoO₃ via MoO₂ and MoO₃ Reduction to MoO₂: A NAPPE Study, *J. Phys. Chem. C.* 122 (2018) 23034–23044. <https://doi.org/10.1021/acs.jpcc.8b07024>.
- [128] M. Kröger, S. Hamwi, J. Meyer, T. Riedl, W. Kowalsky, A. Kahn, Role of the deep-lying electronic states of MoO₃ in the enhancement of hole-injection in organic thin films, *Appl. Phys. Lett.* 95 (2009) 123301. <https://doi.org/10.1063/1.3231928>.
- [129] V. Nasretdinova, Y.A. Gerasimenko, J. Mravlje, G. Gatti, P. Sutar, D. Svetin, A. Meden, V. Kabanov, A.Y. Kuntsevich, M. Grioni, D. Mihailovic, Unveiling the electronic transformations in the semi-metallic correlated-electron transitional oxide Mo₈O₂₃, *Sci. Rep.* 9 (2019) 15959. <https://doi.org/10.1038/s41598-019-52231-4>.
- [130] J.G. Choi, L.T. Thompson, XPS study of as-prepared and reduced molybdenum oxides, *Appl. Surf. Sci.* 93 (1996) 143–149. [https://doi.org/10.1016/0169-4332\(95\)00317-7](https://doi.org/10.1016/0169-4332(95)00317-7).
- [131] A. Arash, T. Ahmed, A. Govind Rajan, S. Walia, F. Rahman, A. Mazumder, R. Ramanathan, S. Sriram, M. Bhaskaran, E. Mayes, M.S. Strano, S. Balendhran, Large-Area synthesis of 2D MoO_{3-x} for enhanced optoelectronic applications, *2D Mater.* 6 (2019) 035031. <https://doi.org/10.1088/2053-1583/ab1114>.
- [132] R.S. Datta, F. Haque, M. Mohiuddin, B.J. Carey, N. Syed, A. Zavabeti, B. Zhang, H. Khan, K.J. Berean, J.Z. Ou, N. Mahmood, T. Daeneke, K. Kalantar-zadeh, Highly active two dimensional α -MoO_{3-x} for the electrocatalytic hydrogen evolution reaction, *J. Mater. Chem. A.* 5 (2017) 24223–24231. <https://doi.org/10.1039/C7TA07705J>.
- [133] M. Setvín, M. Wagner, M. Schmid, G.S. Parkinson, U. Diebold, Surface point defects on bulk oxides: atomically-resolved scanning probe microscopy, *Chem. Soc. Rev.* 46 (2017) 1772–1784. <https://doi.org/10.1039/C7CS00076F>.
- [134] C. Rodenbücher, G. Bihlmayer, W. Speier, J. Kubacki, M. Wojtyniak, M. Rogala, D. Wrana, F. Krok, K. Szot, Local surface conductivity of transition metal oxides mapped with true atomic resolution, *Nanoscale.* 10 (2018) 11498–11505. <https://doi.org/10.1039/C8NR02562B>.
- [135] A.R. Head, C. Gattinoni, L. Trotochaud, Y. Yu, O. Karslıoğlu, S. Pletincx, B. Eichhorn, H. Bluhm, Water (Non-)Interaction with MoO₃, *J. Phys. Chem. C.* 123 (2019) 16836–16842. <https://doi.org/10.1021/acs.jpcc.9b03822>.
- [136] H.K. Jeong, C. Yang, B.S. Kim, K. Kim, Valence band of graphite oxide, *Europhys. Lett.* 92 (2010) 37005. <https://doi.org/10.1209/0295-5075/92/37005>.
- [137] P.A. Fernández Garrillo, B. Grévin, N. Chevalier, L. Borowik, Ł. Borowik, Calibrated work function mapping by Kelvin probe force microscopy, *Rev. Sci. Instrum.* 89 (2018) 043702. <https://doi.org/10.1063/1.5007619>.
- [138] K. Inzani, M. Nematollahi, F. Vullum-Bruer, T. Grande, T.W. Reenaas, S.M. Selbach, Electronic properties of reduced molybdenum oxides, *Phys. Chem. Chem. Phys.* 19 (2017) 9232–9245. <https://doi.org/10.1039/C7CP00644F>.
- [139] K. Inzani, T. Grande, F. Vullum-Bruer, S.M. Selbach, A van der Waals Density Functional Study of MoO₃ and Its Oxygen Vacancies, *J. Phys. Chem. C.* 120 (2016) 8959–8968. <https://doi.org/10.1021/acs.jpcc.6b00585>.

- [140] X. Li, W. Cai, J. An, S. Kim, J. Nah, D. Yang, R. Piner, A. Velamakanni, I. Jung, E. Tutuc, S.K. Banerjee, L. Colombo, R.S. Ruoff, Large-Area Synthesis of High-Quality and Uniform Graphene Films on Copper Foils, *Science*. 324 (2009) 1312–1314. <https://doi.org/10.1126/science.1171245>.
- [141] G. Giovannetti, P.A. Khomyakov, G. Brocks, V.M. Karpan, J. van den Brink, P.J. Kelly, Doping Graphene with Metal Contacts, *Phys. Rev. Lett.* 101 (2008) 026803. <https://doi.org/10.1103/PhysRevLett.101.026803>.
- [142] I. Wlasny, P. Dabrowski, M. Rogala, P.J. Kowalczyk, I. Pasternak, W. Strupinski, J.M. Baranowski, Z. Klusek, Role of graphene defects in corrosion of graphene-coated Cu(111) surface, *Appl. Phys. Lett.* 102 (2013) 111601. <https://doi.org/10.1063/1.4795861>.
- [143] C. Xia, A.A. Tal, L.I. Johansson, W. Olovsson, I.A. Abrikosov, C. Jacobi, Effects of rhenium on graphene grown on SiC(0001), *J. Electron Spectros. Relat. Phenomena*. 222 (2018) 117–121. <https://doi.org/10.1016/j.elspec.2017.07.006>.
- [144] D. Momeni Pakdehi, P. Schädlich, T.T.N. Nguyen, A.A. Zakharov, S. Wundrack, E. Najafidehaghani, F. Speck, K. Pierz, T. Seyller, C. Tegenkamp, H.W. Schumacher, Silicon Carbide Stacking-Order-Induced Doping Variation in Epitaxial Graphene, *Adv. Funct. Mater.* 30 (2020) 2004695. <https://doi.org/10.1002/adfm.202004695>.
- [145] K. Biswas, C.N.R. Rao, Metallic ReO₃ nanoparticles, *J. Phys. Chem. B*. 110 (2006) 842–845. <https://doi.org/10.1021/jp055670b>.
- [146] J. Grobelny, D.-H. Tsai, D.-I. Kim, N. Pradeep, R.F. Cook, M.R. Zachariah, Mechanism of nanoparticle manipulation by scanning tunnelling microscopy, *Nanotechnology*. 17 (2006) 5519–5524. <https://doi.org/10.1088/0957-4484/17/21/037>.
- [147] J. Meyer, A. Shu, M. Kröger, A. Kahn, Effect of contamination on the electronic structure and hole-injection properties of MoO₃/organic semiconductor interfaces, *Appl. Phys. Lett.* 96 (2010) 133308. <https://doi.org/10.1063/1.3374333>.
- [148] I. Irfan, A. James Turinske, Z. Bao, Y. Gao, Work function recovery of air exposed molybdenum oxide thin films, *Appl. Phys. Lett.* 101 (2012) 093305. <https://doi.org/10.1063/1.4748978>.
- [149] A. Apte, K. Mozaffari, F.S. Samghabadi, J.A. Hachtel, L. Chang, S. Susarla, J.C. Idrobo, D.C. Moore, N.R. Glavin, D. Litvinov, P. Sharma, A.B. Puthirath, P.M. Ajayan, 2D Electrets of Ultrathin MoO₂ with Apparent Piezoelectricity, *Adv. Mater.* 32 (2020) 2000006. <https://doi.org/10.1002/adma.202000006>.
- [150] W. Xie, M. Su, Z. Zheng, Y. Wang, L. Gong, F. Xie, W. Zhang, Z. Luo, J. Luo, P. Liu, N. Xu, S. Deng, H. Chen, J. Chen, Nanoscale Insights into the Hydrogenation Process of Layered α -MoO₃, *ACS Nano*. 10 (2016) 1662–1670. <https://doi.org/10.1021/acsnano.5b07420>.
- [151] Y. Wang, X. Du, J. Wang, M. Su, X. Wan, H. Meng, W. Xie, J. Xu, P. Liu, Growth of Large-Scale, Large-Size, Few-Layered α -MoO₃ on SiO₂ and Its Photoresponse Mechanism, *ACS Appl. Mater. Interfaces*. 9 (2017) 5543–5549. <https://doi.org/10.1021/acsami.6b13743>.
- [152] V. Panchal, R. Pearce, R. Yakimova, A. Tzalenchuk, O. Kazakova, Standardization of surface potential measurements of graphene domains, *Sci. Rep.* 3 (2013) 2597. <https://doi.org/10.1038/srep02597>.
- [153] T. Filleter, K. V. Emtsev, T. Seyller, R. Bennewitz, Local work function measurements of epitaxial graphene, *Appl. Phys. Lett.* 93 (2008) 133117. <https://doi.org/10.1063/1.2993341>.
- [154] D.S. Jakob, H. Wang, X.G. Xu, Pulsed Force Kelvin Probe Force Microscopy, *ACS Nano*. 14 (2020) 4839–4848. <https://doi.org/10.1021/acsnano.0c00767>.
- [155] M. Bielecki, T. Hynninen, T.M. Soini, M. Pivetta, C.R. Henry, A.S. Foster, F. Esch, C. Barth, U. Heiz, Topography and work function measurements of thin MgO(001) films on Ag(001) by nc-AFM and KPFM, *Phys. Chem. Chem. Phys.* 12 (2010) 3203. <https://doi.org/10.1039/b923296f>.
- [156] R.L. Smith, G.S. Rohrer, An Atomic Force Microscopy Study of the Morphological Evolution of the MoO₃(010) Surface during Reduction Reactions, *J. Catal.* 163 (1996) 12–17. <https://doi.org/10.1006/jcat.1996.0300>.
- [157] O. Miramontes, F. Bonafé, U. Santiago, E. Larios-Rodriguez, J.J. Velázquez-Salazar, M.M. Mariscal, M.J. Yacamán, Ultra-small rhenium clusters supported on graphene, *Phys. Chem. Chem. Phys.* 17 (2015) 7898–7906. <https://doi.org/10.1039/C4CP05660D>.
- [158] F. Ferrante, A. Prestianni, R. Cortese, R. Schimmenti, D. Duca, Density Functional Theory Investigation on the Nucleation of Homo- and Heteronuclear Metal Clusters on Defective Graphene, *J. Phys. Chem. C*. 120 (2016) 12022–12031. <https://doi.org/10.1021/acs.jpcc.6b02833>.

- [159] C. Tonnoir, A. Kimouche, J. Coraux, L. Magaud, B. Delsol, B. Gilles, C. Chapelier, Induced Superconductivity in Graphene Grown on Rhenium, *Phys. Rev. Lett.* 111 (2013) 246805. <https://doi.org/10.1103/PhysRevLett.111.246805>.
- [160] S. Ikebe, K. Suzuki, H. Nishikawa, D. Shimada, N. TSuda, Scanning Tunneling Microscopy of the ReO₃ Surface, *Jpn. J. Appl. Phys.* 31 (1992) 2221–2225. <https://doi.org/10.1143/JJAP.31.2221>.
- [161] M. Fröba, K. Lochte, W. Metz, XANES studies on rhenium L absorption edges of Re₂O₇ graphite intercalation compounds and of other rhenium-oxygen compounds, *J. Phys. Chem. Solids.* 57 (1996) 635–641. [https://doi.org/10.1016/0022-3697\(95\)00242-1](https://doi.org/10.1016/0022-3697(95)00242-1).
- [162] P. Scharff, E. Stumpp, M. Höhne, Y.X. Wang, Upon the intercalation of rhenium heptoxide and rhenium trioxide nitrate into graphite, *Carbon.* 29 (1991) 595–597. [https://doi.org/10.1016/0008-6223\(91\)90125-3](https://doi.org/10.1016/0008-6223(91)90125-3).
- [163] H. Oppermann, Gesamtdruckmessungen und Gasphasenzusammensetzung ueber Re₂O₇, ReO₃ und ReO₂, *Zeitschrift Foer Anorg. Und Allg. Chemie.* 523 (1985) 135–144. <https://doi.org/10.1002/zaac.19855230417>.
- [164] N.R. Murphy, R.C. Gallagher, L. Sun, J.G. Jones, J.T. Grant, Optical and chemical properties of mixed-valent rhenium oxide films synthesized by reactive DC magnetron sputtering, *Opt. Mater.* 45 (2015) 191–196. <https://doi.org/10.1016/J.OPTMAT.2015.03.035>.
- [165] F. Banhart, J. Kotakoski, A. V. Krasheninnikov, Structural Defects in Graphene, *ACS Nano.* 5 (2011) 26–41. <https://doi.org/10.1021/nn102598m>.
- [166] T. Junno, S. Anand, K. Deppert, L. Montelius, L. Samuelson, Contact mode atomic force microscopy imaging of nanometer-sized particles, *Appl. Phys. Lett.* 66 (1995) 3295–3297. <https://doi.org/10.1063/1.113735>.
- [167] M. Sitti, Atomic Force Microscope Probe Based Controlled Pushing for Nanotribological Characterization, *IEEE/ASME Trans. Mechatronics.* 9 (2004) 343–349. <https://doi.org/10.1109/TMECH.2004.828654>.
- [168] A. Mattausch, O. Pankratov, Ab Initio Study of Graphene on SiC, *Phys. Rev. Lett.* 99 (2007) 076802. <https://doi.org/10.1103/PhysRevLett.99.076802>.
- [169] T. Yoneda, M. Shibuya, K. Mitsuhashi, A. Visikovskiy, Y. Hoshino, Y. Kido, Graphene on SiC(0001) and SiC(000I) surfaces grown via Ni-silicidation reactions, *Surf. Sci.* 604 (2010) 1509–1515. <https://doi.org/10.1016/j.susc.2010.05.019>.
- [170] S. Hussain, J. Singh, D. Vikraman, A.K. Singh, M.Z. Iqbal, M.F. Khan, P. Kumar, D.-C. Choi, W. Song, K.-S. An, J. Eom, W.-G. Lee, J. Jung, Large-area, continuous and high electrical performances of bilayer to few layers MoS₂ fabricated by RF sputtering via post-deposition annealing method, *Sci. Rep.* 6 (2016) 30791. <https://doi.org/10.1038/srep30791>.
- [171] X. Xiong, W. Luo, X. Hu, C. Chen, L. Qie, D. Hou, Y. Huang, Flexible Membranes of MoS₂/C Nanofibers by Electrospinning as Binder-Free Anodes for High-Performance Sodium-Ion Batteries, *Sci. Rep.* 5 (2015) 9254. <https://doi.org/10.1038/srep09254>.
- [172] N. Salazar, I. Beinik, J. V. Lauritsen, Single-layer MoS₂ formation by sulfidation of molybdenum oxides in different oxidation states on Au(111), *Phys. Chem. Chem. Phys.* 19 (2017) 14020–14029. <https://doi.org/10.1039/C7CP00958E>.
- [173] B. Zheng, Z. Wang, Y. Chen, W. Zhang, X. Li, Centimeter-sized 2D α -MoO₃ single crystal: Growth, Raman anisotropy, and optoelectronic properties, *2D Mater.* 5 (2018) 045011. <https://doi.org/10.1088/2053-1583/aad2ba>.
- [174] R.I. Romanov, M.G. Kozodaev, D.I. Myakota, A.G. Chernikova, S.M. Novikov, V.S. Volkov, A.S. Slavich, S.S. Zarubin, P.S. Chizhov, R.R. Khakimov, A.A. Chouprik, C.S. Hwang, A.M. Markeev, Synthesis of Large Area Two-Dimensional MoS₂ Films by Sulfurization of Atomic Layer Deposited MoO₃ Thin Film for Nanoelectronic Applications, *ACS Appl. Nano Mater.* 2 (2019) 7521–7531. <https://doi.org/10.1021/acsanm.9b01539>.
- [175] S. Yazdani, R. Kashfi-Sadabad, T.D. Huan, M.D. Morales-Acosta, M.T. Pettes, Polyelectrolyte-Assisted Oxygen Vacancies: A New Route to Defect Engineering in Molybdenum Oxide, *Langmuir.* 34 (2018) 6296–6306. <https://doi.org/10.1021/acs.langmuir.8b00539>.
- [176] Irfan, F. So, Y. Gao, Photoemission Spectroscopy Characterization of Attempts to Deposit MoO₂ Thin Film, *Int. J. Photoenergy.* 2011 (2011) 1–6. <https://doi.org/10.1155/2011/314702>.

Appendix A: XPS Database for Mo3d

While details of analysis and peak modelling are given in Experimental Section 2.3, here in Table 3 is presented a database of Mo3d analysis by XPS. The literature data of binding energy values and energy separation of Mo oxidation states served as a base for interpretation of Mo samples described in this thesis. Table 3 is summarized with a line of chosen energies used in this study.

It is worth noting that some of the references highlight energy separation with respect to oxygen as well as carbon. Yet with those data one should be careful and first make sure of trustworthy analysis of contaminants at measured surface.

Ref.	Mo oxidation state: Mo3d						Binding Energy Separation (eV)						
	Binding Energy (eV)						6+	5/2	5/2	$\Delta O1s-Mo3d$		$\Delta C1s-Mo3d$	
	4+ 5/2	4+ 3/2	5+ 5/2	5+ 3/2	6+ 5/2	6+ 3/2	3/2-5/2	(4+)- (6+)	(5+)- (6+)	5+ 5/2	6+ 5/2	5+ 5/2	6+ 5/2
[81]	229.5	232.6			232.7	235.7	3.1	3.2					
[170]	229.1	232.2			232.8	235.9	3.1	3.7					
[171]	229.5	232.8			232.7	236.0	3.3	3.2					
[6]			231.6	234.8	232.6	235.8	3.2		1.0			52.6	51.6
[19]			231.6	234.7	232.4	235.5	3.1		0.8			52.4	51.6
[37]													
[41]	228.6	231.8	230.8	234.0	232.1	235.3	3.2	3.5	1.3			53.4	52.1
[172]	229.7	232.8	231.2	234.3	232.5	235.6	3.1	2.8	1.3				
[71]	230.1		231.4		232.7			2.6	1.3				
[70]			231.7	234.8	232.8	235.8	3.0		1.0	299.6	297.2		
[72]					232.5								
[79]	229.2	232.3			232.7	235.9	3.2	3.5					
[173]					232.5	235.6	3.2						
[44]					232.8	236.0	3.2			297.7			
[78]			231.1	234.2	232.3	235.4	3.1		1.2				
[174]					233.2	236.3	3.1						
[131]	230.3	233.5	231.8		233.2	236.4	3.2	2.9	1.4	301.0	297.8		
[65]	230.7	233.9	231.6	234.8	232.5	235.7	3.16	1.8	0.9	300.1	298.0		
[175]	229.1	233.0	231.5	234.8	233.2	236.3	3.1	4.1	1.7				
[138]	229.8		232.2		233.4			3.6	1.2				
[127]	229.1				232.5			3.4		297.5			
[32]										297.8			
[176]	228.8		230.4		232.0		3.2	3.2	1.6	297.8			
[151]			231.8	235.1	232.8	235.9	3.1		1.0	299.1	297.8		
this work			231.8	234.9	233.2	236.3	3.1		1.4	300.5	297.8	52.7	51.3

Table 3: Database of Mo3d region analysis by XPS. Literature data of binding energy values and energy separation of Mo oxidation states.

Appendix B: Academic achievements

B1. Publications

The list of author's papers, which are under revision, is presented below. The relevant findings are included in this Thesis.

- I. **D.A. Kowalczyk**, M. Rogala, K. Szałowski, D. Belić, P. Dąbrowski, P. Krukowski, I. Lutsyk, M. Piskorski, A. Nadolska, P. Krempieński, M. Le Ster, P.J. Kowalczyk
Two-dimensional crystals as a buffer layer for high work function applications: the case of monolayer MoO₃
submitted to ACS Applied Materials & Interfaces (2022)
- II. Y. Lei, T. Zhang, Y-C. Lin, T. Granzier-Nakajima, G. Bepete, **D.A. Kowalczyk**, Z. Lin, D. Zhou, T. Schranghamer, A. Dodda, A. Sebastian, Y. Chen, Y. Liu, G. Pourtois, T. Kempa, B. Schuler, M. Edmonds, S.Y. Quek, U. Wurstbauer, S. Wu, N. Glavin, S. Das, S. Dash, J. Redwing, J. Robinson, M. Terrones;
Graphene and Beyond: Recent Advances in Two-Dimensional Materials Synthesis, Properties, and Devices;
submitted to ACS Nanoscience Au (2022)

The list of author's papers, which are included in this Thesis, is presented below.

- III. P.J. Kowalczyk, P. Krukowski, **D.A. Kowalczyk**, K. Pabianek, I. Lutsyk, M. Rogala, P. Dąbrowski, A. Busiakiewicz, M. Piskorski, W. Kozłowski, B. Łuszczynska, R. Udovyt'ska, J. Jung, J. Ulański, J.M. Baranowski, S.A. Brown, G. Bian
Elastyczne ogniwa fotowoltaiczne na bazie materiałów dwuwymiarowych i ich hybryd
Przełęcz Elektrotechniczny, 2, 117 (2022) DOI:10.15199/48.2022.02.26
- IV. **D.A. Kowalczyk**, M. Rogala, K. Szałowski, W. Kozłowski, I. Lutsyk, M. Piskorski, P. Krukowski, P. Dąbrowski, D. Belić, M. Cichomski, Z. Klusek, P.J. Kowalczyk
Local electronic structure of stable monolayers of α -MoO_{3-x} grown on graphite substrate
2D Materials, 8, 25005 (2021) DOI:10.1088/2053-1583/abcf10
- V. P. Krukowski, **D.A. Kowalczyk**, M. Piskorski, P. Dąbrowski, M. Rogala, P. Caban, P. Ciepielewski, J. Jung, J.M. Baranowski, J. Ulański, Z. Klusek
Work Function Tunability of Graphene with Thermally Evaporated Rhenium Heptoxide for Transparent Electrode Applications
Advanced Engineering Materials, 22, 1900955 (2019) DOI:10.1002/adem.201900955

The list of author's papers, which are excluded from this Thesis, is presented below.

- VI. M. Cichomski, M. Prowizor, **D.A. Kowalczyk**, A. Sikora, D. Batory, M. Dudek
Comparison of the Physicochemical Properties of Carboxylic and Phosphonic Acid Self-Assembled Monolayers Created on a Ti-6Al-4V Substrate
Materials, 13, 5137 (2020) DOI:10.3390/ma13225137
- VII. P. Dąbrowski, M. Rogala, I. Pasternak, P. Krukowski, J.M. Baranowski, W. Strupiński, I. Lutsyk, **D.A. Kowalczyk**, S. Pawłowski, Z. Klusek;
Early oxidation stages of germanium substrate in the graphene/Ge(001) system;
Carbon, 149, 290-296 (2019) DOI:10.1016/j.carbon.2019.04.036
- VIII. Lutsyk, M. Rogala, P. Dąbrowski, P. Krukowski, P.J. Kowalczyk, A. Busiakiewicz, **D.A. Kowalczyk**, E. Łacińska, J. Binder, N. Olszowska, M. Kopciuszynski, K. Szałowski, M. Gmitra, R. Stępniewski, M. Jałochowski, J.J. Kołodziej, A. Wyszomłek, Z. Klusek;

Electronic structure of commensurate, nearly commensurate, and incommensurate phases of 1T-TaS₂ by angle-resolved photoelectron spectroscopy, scanning tunneling spectroscopy, and density functional theory;

Physical Review B, 98, 195425 (2018) DOI:10.1103/PhysRevB.98.195425

B2. Dissemination of Results: Conference Contribution

The list of personal author's conference contributions both in oral and poster form is presented below. The disseminated results are included in this Thesis.

- I. **D.A. Kowalczyk**, M. Rogala, P. Dąbrowski, K. Szałowski, P. Krukowski, Z. Klusek
POSTER: **Re₂O₇/graphene heterostructure towards transparent anode in OLEDs**
Graphene Week 2019 September 23 - 27 2019, Helsinki, Finland
- II. **D.A. Kowalczyk**, M. Rogala, P. Dąbrowski, K. Szałowski, P. Krukowski, Z. Klusek
POSTER: **Heterostruktuury grafenu z tlenkami renu do zastosowań w organicznych diodach emitujących światło**
IX Krajowa Konferencja Nanotechnologii 2019 July 01 - 03 2019, Wrocław, Poland
- III. **D.A. Kowalczyk**, M. Rogala, P. Dąbrowski, P. Krukowski, Z. Klusek
POSTER: **Manipulacja nanocząstkami Re₂O₇ osadzonymi na grafenie**
III Doktoranckie Sympozjum Nanotechnologii NanoMat June 13 - 14 2019, Łódź, Poland
- IV. **D.A. Kowalczyk**, P. Krukowski, M. Rogala, P. Dąbrowski, P. Ciepielewski, P. Caban, J.M. Baranowski, Z. Klusek
ORAL: **Układy hybrydowe grafen-tlenek metalu przejściowego w zastosowaniu do elastycznej elektroniki organicznej (eng. The hybrid systems of graphene-oxide of transition metal in application to flexible organic electronics)**
X Seminarium Badania prowadzone metodami skaningowej mikroskopii bliskich oddziaływań STM/AFM 2018 November 28 - December 02 2018, Zakopane, Poland
- V. **D.A. Kowalczyk**, P. Krukowski, M. Rogala, P. Dąbrowski, P. Ciepielewski, P. Caban, J.M. Baranowski, Z. Klusek
ORAL: **Badania układów hybrydowych grafen-tlenek metalu przejściowego w zastosowaniu do elastycznej elektroniki organicznej (eng. Investigations of hybrid graphene-transition metal oxide systems towards application to flexible organic electronics)**
IV Krajowa Konferencja „Grafen i inne materiały 2D” September 24 - 26 2018, Szczecin, Poland
- VI. **D.A. Kowalczyk**, P. Krukowski, M. Rogala, P. Dąbrowski, P. Ciepielewski, P. Caban, J.M. Baranowski, Z. Klusek
ORAL: **Układy hybrydowe grafen-tlenek metalu przejściowego w zastosowaniu do elastycznej elektroniki organicznej - osadzanie i charakteryzacja tlenków molibdenu i renu (eng. Graphene-transition metal hybrid systems in application to flexible organic electronics - deposition and characterization of molybdenum and rhenium oxides)**
II Doktoranckie Sympozjum Nanotechnologii NanoMat June 21 - 22 2018, Łódź, Poland

The list of co-authored conference contributions both in oral and poster form is presented below.

- VII. **M. Kim**, N. Ahsan, N. Trainor, C. Chen, **D.A. Kowalczyk**, J. M. Redwing, Y. Okada
Epitaxial Growth of Molybdenum Disulfide on Off-angle Sapphire by Metal-organic Chemical Vapor Deposition
9th International Symposium on Control of Semiconductor Interfaces, September 5 - 8 2022, Nagoya, Japan

- VIII. M. Kim, N. Ahsan, N. Trainor, C. Chen, **D.A. Kowalczyk**, J. M. Redwing, Y. Okada
Epitaxial Growth of Molybdenum Disulfide on Different Planes of Sapphire by MOCVD
8th Korea-Japan Joint Seminar on PV, July 6 - 8 2022, Jeju, Korea
- IX. N. Trainor, C. Chen, M. Kim, **D.A. Kowalczyk**, J.M. Redwing
ORAL: **Kinetics of wafer-scale epitaxial growth of MoS₂ on sapphire**
The Electronic Materials Conference (EMC), Jun 29-Jul 1 2022, Ohio, USA
- X. M. Kim, N. Ahsan, N. Trainor, C. Chen, **D.A. Kowalczyk**, J. M. Redwing, Y. Okada
ORAL: **Epitaxial growth of MoS₂ on c-Al₂O₃ by MOCVD**
The Japan Society of Applied Physics Spring Meeting 2022 (JSAP), March 22 -26 2022, hybrid:
Japan and online
- XI. M. Piskorski, W. Kozłowski, I. Lutsyk, **D.A. Kowalczyk**, P. Dąbrowski, M. Rogala, P. Krukowski,
P.J. Kowalczyk
Raman spectroscopy of reactive 2D materials under an inert gas atmosphere
Graphene and other 2D materials, September 13 - 15 2021, Online, Poland
- XII. P. Krukowski, M. Piskorski, R. Udovyt'ska, **D.A. Kowalczyk**, I. Lutsyk, P. Dąbrowski, M. Rogala, W.
Kozłowski, J.M. Baranowski, J. Jung, J. Ulański, Z. Klusek, A. Saito, H. Osuga, Y. Kuwahara, P.J.
Kowalczyk
**Organic light-emitting diode based on graphene electrode modified with transition metal
oxides and light emission induced by scanning tunneling microscope at molecular scale**
Graphene and other 2D materials September 13 - 15 2021, Online, Poland
- XIII. **D.A. Kowalczyk**, M. Rogala, K. Szałowski, W. Kozłowski, I. Lutsyk, M. Piskorski, P. Krukowski, P.
Dąbrowski, D. Belić, Z. Klusek, and P.J. Kowalczyk
ORAL: **Monolayers of α -MoO_{3-x} on graphite substrate growth and electronic structure
characterization**
Graphene and other 2D materials September 13 - 15 2021, Online, Poland
- XIV. I. Lutsyk, P. Dąbrowski, **D.A. Kowalczyk**, M. Rogala, K. Szałowski, W. Kozłowski, M. Piskorski, P.
Krukowski, and P.J. Kowalczyk
Electronic properties of the graphene and TaS₂ hybrid systems
Graphene and other 2D materials September 13 - 15 2021, Online, Poland
- XV. P.J. Kowalczyk, P. Krukowski, **D.A. Kowalczyk**, K. Pabianek, I. Lutsyk, M. Rogala, P. Dąbrowski, A.
Busiakiewicz, M. Piskorski, W. Kozłowski, B. Łuszczynska, R. Udovyt'ska, J. Jung, J. Ulański, J.M.
Baranowski, S.A. Brown, G. Bian
Elastyczne ogniwa fotowoltaiczne na bazie materiałów dwuwymiarowych i ich hybryd
XX Krajowa Konferencja Elektroniki September 05 - 09 2021, Darłowo, Poland
- XVI. P.J. Kowalczyk, I. Lutsyk, **D.A. Kowalczyk**, M. Rogala, P. Dąbrowski, P. Krukowski, M. Piskorski,
W. Kozłowski, E. Lacinska, A. Wymołek, R. Stępniewski, J. Binder, R. Udovyt'ska, J. Jung, J.
Ulański, J.M. Baranowski, S.A. Brown, G. Bian and Z. Klusek
2D materials and their hybrids: pathway toward new phenomena
49th International School & Conference on the Physics of Semiconductors September 01 - 10
2021, Online, Poland
- XVII. P.J. Kowalczyk, I. Lutsyk, **D.A. Kowalczyk**, M. Rogala, P. Dąbrowski, P. Krukowski, M. Piskorski,
W. Kozłowski, E.M. Łacińska, A. Wymołek, R. Stępniewski, J. Binder, R. Udovyt'ska, J. Jung, J.
Ulański, J.M. Baranowski, S.A. Brown, G. Bian, Z. Klusek
Heterostructures of 2D Materials: Bottom Up and Top Down approach
Global Summit and Expo on Graphene and 2D Materials August 23 - 25 2021, Online, France
- XVIII. P. Krukowski, R. Udovyt'ska, **D.A. Kowalczyk**, M. Piskorski, P. Dąbrowski, M. Rogala, P. Caban, P.
Ciepielewski, J.M. Baranowski, R. Dunał, J. Jung, J. Ulański, Z. Klusek, P.J. Kowalczyk
**Organic light-emitting diode (OLED) based on graphene electrode modified with rhenium
oxide**

- 14th International Symposium on Flexible Organic Electronics ISFOE21 July 05 - 08 2021, Thessaloniki, Greece
- XXIX. P. Krukowski, R. Udovyt'ska, **D.A. Kowalczyk**, M. Piskorski, P. Dąbrowski, M. Rogala, P. Caban, P. Ciepielewski, J.M. Baranowski, R. Dunal, J. Jung, J. Ulański, Z. Klusek, P.J. Kowalczyk
Organic light-emitting diode (OLED) based on graphene electrode modified with rhenium oxide
16th International Summer Schools on Nanosciences & Nanotechnologies, Organic Electronics and Nanomedicine July 03 - 10 2021, Thessaloniki, Greece
- XX. A. Rydosz, K. Zakrzewska, E. Kusior, P. Krukowski, **D.A. Kowalczyk**, Z. Klusek
Hierarchically structured MoO_x thin films for gas sensor and OLED applications
2019 E-MRS Fall Meeting September 16 - 19 2019, Warsaw, University of Technology, Poland
- XXI. M. Piskorski, P. Krukowski, W. Kozłowski, I. Lutsyk, **D.A. Kowalczyk**, P. Dąbrowski, M. Rogala, P.J. Kowalczyk, Z. Klusek
POSTER: Spektroskopia Ramana w atmosferze gazu obojętnej oraz w warunkach ultra wysokiej próżni
IX Krajowa Konferencja Nanotechnologii 2019 July 01 - 03 2019, Wrocław, Poland
- XXII. M. Rogala, P. Dąbrowski, I. Lutsyk, **D.A. Kowalczyk**, E.M. Łacińska, I. Pasternak, W. Strupiński, J.M. Baranowski, A. Wyszomółek and Z. Klusek
POSTER: Van der Waals hybrid structures: 1T-TaS₂/graphene and Bi₂Se₃/graphene systems
Graphene 2019 June 24 - 28 2019, Rome, Italy
- XXIII. E.Z. Frątczak, **D.A. Kowalczyk**, K. Pabianek, P. Dąbrowski, M. Rogala, J. Czerwińska, T. Kłęb, W. Kozłowski, A. Busiakiewicz, P.J. Kowalczyk, Z. Sieradzki, Z. Klusek
POSTER: Wykorzystanie technik skaningowej mikroskopii bliskich oddziaływań do badania wielowarstwowych wydruków Ink-Jet na potrzeby elektroniki elastycznej
X Seminarium Badania prowadzone metodami skaningowej mikroskopii bliskich oddziaływań STM/AFM 2018 November 28 - December 02 2018, Zakopane, Poland
- XXIV. M. Rogala, P. Dąbrowski, P.J. Kowalczyk, I. Własny, W. Kozłowski, A. Busiakiewicz, I. Lutsyk, **D.A. Kowalczyk**, E.Z. Frątczak, L. Lipińska, J.M. Baranowski, Z. Klusek
POSTER: W jaki sposób (nie) badać cienkich warstw tlenku grafenu - wpływ procesu pomiaru na materiał
X Seminarium Badania prowadzone metodami skaningowej mikroskopii bliskich oddziaływań STM/AFM 2018 November 28 - December 02 2018, Zakopane, Poland
- XXV. P.J. Kowalczyk, W. Kozłowski, A. Busiakiewicz, M. Rogala, P. Dąbrowski, S. Pawłowski, J. Czerwińska, E.Z. Frątczak, M. Piskorski, P. Krukowski, **D.A. Kowalczyk**, K. Pabianek, I. Lutsyk, Z. Klusek
POSTER: Struktura elektronowa bizmutenu
X Seminarium Badania prowadzone metodami skaningowej mikroskopii bliskich oddziaływań STM/AFM 2018 November 28 - December 02 2018, Zakopane, Poland
- XXVI. P. Dąbrowski, A. Materna, M. Rogala, P. Krukowski, A. Busiakiewicz, W. Kozłowski, P.J. Kowalczyk, I. Lutsyk, **D.A. Kowalczyk**, M. Kopciuszynski, M. Jałochowski, Z. Klusek
ORAL: Własności elektronowe hybrydowych materiałów Diraca na przykładzie układu grafen/Bi₂Se₃
IV Krajowa Konferencja „Grafen i inne materiały 2D” September 24 - 26 2018, Szczecin, Poland
- XXVII. A. Rydosz, E. Kusior, K. Zakrzewska, P. Krukowski, **D.A. Kowalczyk**, Z. Klusek
POSTER: MoO/graphene thin film system for organic electronics
Nanosmat 2018 - 13th International Conference on Surfaces, Coatings and Nanostructured Materials September 11 - 14 2018, Gdańsk, Poland
- XXVIII. Z. Klusek, I. Lutsyk, **D.A. Kowalczyk**, K. Pabianek, P. Dąbrowski, M. Rogala, A. Busiakiewicz, P. Krukowski, P.J. Kowalczyk, W. Kozłowski, J. Ulański, J. Jung, G. Wiosna-Sałyga

ORAL: **Grafenowe układy hybrydowe: fizyka, wytwarzanie, zastosowania**
XXI Kryształ Molekularne 2018 September 03 - 07 2018, Łódź-Kolumna, Poland

- XXIX. P. Krukowski, A. Rydosz, P. Dąbrowski, M. Rogala, A. Busiakiewicz, **D.A. Kowalczyk**, K. Zakrzewska, Z. Klusek
POSTER: **The investigation of growth and structure of thin layers of molybdenum oxide on Si with the aim of building the graphene-based transparent electrodes for organic light emitting diode (OLED)**
The 8th International Symposium on Surface Science October 22 - 26 2017, Tsukuba, Japan

B3. Extracurricular Courses & Activities

The list of author's relevant extracurricular courses and activities is presented below. Two of them include presentations given therein.

- 8-month research project at the Pennsylvania State University
Epitaxial Growth of 2D TMDs on GaN & AlGaIn for Hot Electron Transistors, aimed at integrating 2D materials (MoS₂ and WS₂) with wide bandgap semiconductors (specifically AlN, GaN, and AlGaIn) for electronic applications
Fulbright Junior Research Award, July 2021 – February 2022, State College, USA
 - Graphene Study 2020 (Graphene Flagship), June 17 2020, Online
 - XXIVth International Krutyń Summer School 2019, September 01 - 07 2019, Krutyń, Poland
- XXX. **D.A. Kowalczyk**, M. Rogala, P. Dąbrowski, K. Szałowski, P. Krukowski, Z. Klusek
ORAL: **Studies of the electronic structure of graphene/rhenium oxide heterostructures for anode application in OLEDs**
- XXXI. E.Z. Frątczak, **D.A. Kowalczyk**, M. Rogala, P. Dąbrowski, Z. Sieradzki, Z. Klusek
ORAL: **Design and morphological analysis of printed nanoparticle based silver ink for electronic devices**
- Graphene Study 2019 (Graphene Flagship), February 03 - 08 2019, Obergurl, Austria
- XXXII. **D.A. Kowalczyk**, P. Krukowski, M. Rogala, P. Dąbrowski, M. Kopciuszynski, P. Cielewski, P. Caban, J.M. Baranowski, Z. Klusek
POSTER: **Alternation of Work Function of Graphene/Transition Metal Oxide Heterostructures**
- V School of scanning probe microscopy and spectroscopy SPM, Zakopane, Poland (2018)
 - Graphene Study 2018 (Graphene Flagship), February 05 - 10 2018, Obergurl, Austria
 - 5th Workshop on Flexible and Printed Electronics 2017, November 17 2017, Lodz, Poland